Optimizing Application Driven Multimodality Spatio-Temporal Emission Imaging

Der Technischen Fakultät der
Universität Erlangen–Nürnberg

zur Erlangung des Grades

DOKTOR–INGENIEUR

vorgelegt von

Johannes Zeintl

Erlangen — 2011

Deutscher Titel:
Optimierung von raumzeitlich basierter multimodaler Emissions-Tomographie in definierten Anwendungsbereichen

Als Dissertation genehmigt von der
Technischen Fakultät der
Universität Erlangen-Nürnberg

Tag der Einreichung:	16.04.2010
Tag der Promotion:	22.12.2010
Dekan:	Prof. Dr.-Ing. R. German
Berichterstatter:	Prof. Dr.-Ing. J. Hornegger
	Prof. Dr. A. Yahil
	Prof. Dr. med. T. Kuwert

Abstract

Single Photon Emission Computed Tomography (SPECT) is a widely used nuclear medicine imaging technique with many applications in diagnosis and therapy. With the introduction of hybrid imaging systems, integrating a SPECT and a Computed Tomography (CT) system in one gantry, diagnostic accuracy of nuclear procedures has been improved. Current imaging protocols in clinical practice take between 15 and 45 minutes and Filtered Backprojection (FBP) is still widely used to reconstruct nuclear images. Routine clinical diagnosis is based on reconstructed image intensities which do not represent the true absolute activity concentration of the target object, due to various effects inherent to SPECT image formation.

In this thesis, we present approaches for the optimization of current clinical SPECT/CT imaging for selected applications. We develop analysis tools for the image quality assessment of commonly used static and dynamic cardiac image quality phantoms. We use these tools for the optimization of cardiac imaging protocols with the specific goal of reducing scan time and, at the same time, maintaining diagnostic accuracy. We propose a time-optimized protocol which uses iterative image reconstruction and offers a time reduction by a factor of two, compared to conventional FBP-driven protocols. The optimized protocol shows good agreement with the conventional protocol in terms of perfusion and functional parameters when tested on a normal phantom database and in prospective clinical studies.

In addition to optimizing image acquisition, we propose a calibration method for improved image interpretation which allows to derive absolute quantitative activity concentration values based on reconstructed clinical SPECT images. In this method, we specifically take the non-stationarity of iterative reconstruction into account. In addition, we estimate the imprecision of our quantitative results caused by errors from measurement instrumentation and accumulated through the course of calibration. We could show that accurate quantification in a clinical setup is possible in phantoms and also in-vivo in patients.

We use the proposed calibration method for the quantitative assessment of dynamic processes by using time-contiguous SPECT acquisitions in combination with co-registered CT images and three-dimensional iterative reconstruction. We develop a physical dynamic phantom and establish a baseline for dual-headed SPECT systems by varying time-activity input function and rotation speed of the imaging system. We could show that, using state-of-the-art SPECT/CT systems, an accurate estimation of dynamic parameters is possible for processes with peak times of 30 seconds.

Kurzfassung

Die Einzel-Photonen Emissions-Tomographie (SPECT) ist eine weit verbreitete nuklearmedizinische Bildgebungs-Methode mit einer großen Anzahl von Anwendungsbereichen im Bereich der Diagnose und Therapie. Mit der Einführung der Hybridtechnik, die ein SPECT-System mit einem Computer-Tomographen (CT) in einem Gerät vereint, wurde die diagnostische Güte von nuklearmedizinischen Verfahren verbessert. Die Aufnamhmezeiten klinischer Bildgebungsprotokolle betragen derzeitig üblicherweise 15 bis 45 Minuten und die Rekonstruktion der resultierenden Bilder wird noch hauptsächlich mithilfe der gefilterten Rückprojektion (FBP) durchgeführt. Die Diagnose in der klinischen Routine basiert auf rekonstruierten Bildwerten, die aufgrund von verschiedenen Faktoren in der SPECT Bildformierung nicht die echte Aktivitätskonzentration des Zielobjektes widergeben.

In dieser Arbeit werden Ansätze für die Optimierung von ausgewählten Anwendungen in der klinischen SPECT/CT Bildgebung vorgestellt. Es werden Hilfsmittel für die Untersuchung der Bildqualität von häufig benutzten statischen und dynamischen Herzphantomen entwickelt. Diese Hilfsmittel werden dann für die Optimierung kardiologischer Bildgebungs-Protokolle genutzt mit dem Ziel die Aufnahmezeit zu verringern und gleichzeitig die diagnostische Güte zu erhalten. Ein zeit-optimiertes Protokoll wird vorgeschlagen, welches mithilfe von iterativen Rekonstruktionsverfahren eine Zeitverringerung um den Faktor zwei im Vergleich zu konventionellen FBP-basierten Protokollen bietet. Dieses optimierte Protokoll zeigt im Hinblick auf Perfusions- und Funktionseigenschaften gute Übereinstimmung mit dem konventionellen Protokoll bei Tests mit einer Phantomdatenbank und in klinischen prospektiven Studien.

Zusätzlich zur Optimierung der Bild-Akquisition wird eine Methode zur Verbesserung der Bildinterpretation vorgeschlagen, welche erlaubt absolute quantitative Aktivitätskonzentrationen aus rekonstruierten klinischen SPECT Aufnahmen zu extrahieren. Diese Methode berücksichtigt ausdrücklich die Nicht-Stationarität der iterativen Rekonstruction. Außerdem wird die Ungenauigkeit der quantitativen Ergebnisse geschätzt, die durch Toleranzen der Messinstrumente entsteht und im Zuge der Kalibrierung akkumuliert. Es konnte gezeigt werden, dass genaue Quantifizierung in einer klinischen Umgebung sowohl in Phantomen als auch in-vivo in Patienten möglich ist.

Die entwickelte Kalibrierungsmethode wird ausserdem für die quantitative Bewertung von dynamischen Prozessen benutzt, wobei zeitlich dicht aufeinander folgende SPECT Aufnahmen in Kombination mit co-registrierten CT Aufnahmen und iterativer Rekonstruktion verwendet werden. Ein physisches, dynamisches Phantom wurde entwickelt und eine Richtline für Zweikopf-SPECT-Systeme wurde erstellt, indem Eingangs-Zeit-Aktivitäts-Funktion des Phantoms und Rotationsgeschwindigkeit des Bildgebungssystems variiert wurden. Es konnte gezeigt werden, dass eine genaue Schätzung der dynamischen Parameter für Prozesse mit Einstromzeiten von 30 Sekunden möglich ist, wenn modernste SPECT/CT-Systeme verwendet werden.

Acknowledgment

This thesis is a product of a collaboration between the University of Erlangen-Nuremberg and Siemens Medical Solutions USA, Inc., Molecular Imaging. The preparation of this thesis would not have been possible without the support and advise of a variety of individuals who were involved in this project.

First and foremost, I would like to express my sincere gratitude to my supervisor Prof. Dr.-Ing. Joachim Hornegger. He opened up the opportunity to do research abroad in collaboration with the market leader in medical imaging. He always had an open ear for my concerns and needs throughout the course of my thesis.

I am very thankful to Prof. Dr. Amos Yahil for his co-supervision of my work and for the valuable and lively discussions which helped me to develop over the years.

My special thanks go to Prof. Dr. med. Torsten Kuwert who provided the infrastructure for my research at the Clinic of Nuclear Medicine in Erlangen. I greatly value his medical expertise and enjoyed the fruitful discussions with him which helped me to get a deep insight into the medical aspects of my reserach.

I am very grateful to Dr. Alexander Hans Vija for his excellent co-supervision and for introducing me to the world of nuclear medicine. He coached me through the first year when I came in touch with this exciting field of research. With his knowledge and dedication he helped me becoming a respected member in his team.

In addition, I am indebted to the team in Hoffman Estates in particular Dr. Manjit Ray, Dr. Manojeet Bhattacharya, Dr. Xinhong Ding, and Dr. Ron Malmin for their patient and selfless assistance at all times.

Furthermore, I would like to thank my co-workers at the Clinic of Nuclear Medicine and the Pattern Recognition Lab at the University of Erlangen-Nuremberg and everyone I had the chance to work with over the years, for the fruitful time we spent together.

I would also like to thank the Siemens AG for providing financial support for my research.

Last, but not least, I want to thank my family and my friends for their great patience, support and encouragement throughout all these years.

Johannes Zeintl

Contents

Chapter 1

Introduction

Molecular Medicine seeks the understanding of health and disease at the cellular and molecular level, and to use this information to design new approaches to promote health and prevent, diagnose, and treat disease. Molecular imaging visualizes and localizes molecular processes in vivo for diagnosis and therapy. Minute amounts of a radio-labeled compound ('tracer') are injected and the distribution of this tracer at one or multiple time points is measured thereafter. Tomographic techniques are used to obtain a volumetric image of the tracer distribution which can be analyzed and interpreted. Volumetric imaging has become clinical practice. Single Photon Emission Computed Tomography (SPECT) is a tomographic nuclear medicine imaging technique and has proven high sensitivity and specificity in oncology as well as neurology and cardiology. The diagnostic ability has even been increased with the introduction of multi-modal imaging systems combining SPECT cameras with morphological imaging techniques such as Computed Tomography (CT) in one gantry. Still, in clinical routine the two modalities are spatially and temporally separated when using state-of-the-art SPECT/CT systems. Active research is conducted to acquire, process and analyze multi-modal, spatio-temporal consistent and inconsistent tomographic datasets and to assess the benefits in clinical applications.

1.1 Scope and Contribution to the Progress of Research

This work aims to optimize current routine clinical SPECT/CT imaging by focusing on the key components of the image formation chain: Imaging instrumentation, image acquisition, image reconstruction, and image evaluation and interpretation.
The goals are to increase clinical efficiency and to improve SPECT image quality and diagnostic value.
The following listing specifies current fields of research and points out our main contributions:

- Active research is conducted to accelerate SPECT imaging techniques and maintain diagnostic ability at the same time. In the case of myocardial perfusion studies, current clinical SPECT acquisitions take between 15-25 minutes, whereas a CT scan of the heart is performed in seconds. In order to increase

throughput or lower injected dose, faster SPECT scan protocols are needed. In this work we evaluate new imaging protocols which allow a reduction of cardiac imaging time by 50%. We develop tools for the evaluation of cardiac static and echocardiogram (ECG)-gated images and assess the image quality delivered by time optimized scan protocols. We show that equivalent image quality can be achieved with a protocol which uses 50% of the conventional number of projection views.

- The interpretation of SPECT images in clinical routine is based on pixel intensities which represent photons emitted from the object of interest. Due to physical effects inherent to SPECT image formation, these pixel intensities do not reflect the true activity concentration values in the object. Absolute quantitative representation of the underlying activity distribution is of great interest e.g. for treatment planning in radiotherapy or tumor staging and classification. Various research groups work on absolute quantification in SPECT and showed acceptable accuracies in static phantoms. Very few studies have been published which apply in-vivo quantification. In this thesis we present a calibration technique for quantitative SPECT/CT imaging which can be applied to current clinical SPECT/CT imaging systems. We verify the method with phantom studies and show an average in-vivo quantification accuracy of 1.1% with a 95% confidence interval between -15.4% and +17.5%.

- The common clinical method for the evaluation of dynamic processes in nuclear medicine is a planar study. Disadvantages of planar image acquisition are the superposition of multiple organs and the poor capabilities in terms of absolute quantification. SPECT techniques have been investigated for use in dynamic studies. Still, the full potential and limitations of state-of-the-art SPECT/CT systems for the imaging of dynamic processes are not yet revealed. In this thesis, we establish a baseline for the quantitative capabilities of dual-headed clinical SPECT/CT systems when time-contiguous acquisitions in combination with 3D iterative reconstruction is used.

Some sections of this thesis contain material that has been published or submitted for publication. We specify these articles in the following list:

[1] J. Zeintl, A. H. Vija, J. T. Chapman, E. G. Hawman, and J. Hornegger, "Quantifying the Effects of Acquisition Parameters in Cardiac SPECT Imaging and Comparison with Visual Observers", in *IEEE Nuclear Science Symposium Conference Record*, San Diego, CA, USA, 2006, pp. 3251-3257.

[2] J. Zeintl, X. Ding, A. H. Vija, E. G. Hawman, J. Hornegger, and T. Kuwert, "Estimation accuracy of ejection fraction in gated cardiac SPECT/CT imaging using iterative reconstruction with 3D resolution recovery in rapid acquisition Protocols", in *IEEE Nuclear Science Symposium Conference Record*, Honolulu, HI, USA, 2007, pp. 4491-4496.

[3] J. Zeintl, A. H. Vija, A. Yahil, X. Ding, J. Hornegger, and T. Kuwert, "Towards quantitative SPECT: Error Estimation of SPECT OSEM with 3D Resolution Re-

covery, Attenuation Correction and Scatter Correction", in *IEEE Nuclear Science Symposium Conference Record*, Dresden, Germany, 2008, pp. 4106-4111.

[4] J. Zeintl, A. H. Vija, A. Yahil, J. Hornegger, and T. Kuwert, "Quantitative Accuracy of Slow-Rotating Dynamic SPECT", in *IEEE Nuclear Science Symposium Conference Record*, Orlando, FL, USA, 2009, pp. 3853-3857.

[5] J. Zeintl, A. H. Vija, A. Yahil, J. Hornegger, and T. Kuwert, "Quantitative Accuracy of Clinical Tc-99m SPECT/CT Using OSEM with 3D Resolution Recovery, Attenuation, and Scatter Correction", Journal of Nuclear Medicine, vol. 51, pp. 921-928, 2010.

[6] A. H. Vija, J. Zeintl, J. T. Chapman, E. G. Hawman, and J. Hornegger, "Development of rapid SPECT acquisition protocol for myocardial perfusion imaging", in *IEEE Nuclear Science Symposium Conference Record*, San Diego, CA, USA, 2006, pp. 1811-1816.

1.2 Structure of this Work

This thesis is structured as follows: Chapter 2 describes the physical principles of SPECT imaging and details the key concepts of projection data generation and tomographic reconstruction. An overview of the imaging protocols which are currently used in clinical routine is given and the state of the art of quantitative attempts for static and dynamic SPECT are discussed. This chapter serves as foundation for the subsequent chapters by providing the relevant background information.
Chapter 3 describes the image quality assessment tools developed to evaluate new methods for optimized SPECT imaging. The developed tools process static and ECG-gated cardiac image data sets.
In Chapter 4 these tools are applied for the optimization of cardiac scan protocols. New faster scan protocols are compared with conventional methods in terms of image quality and diagnostic ability.
Chapter 5 introduces methods for fully quantitative image interpretation. State-of-the-art clinical SPECT/CT systems are characterized in terms of emission recovery by identifying systematic biases across the imaging parameter space. A calibration method is developed which allows quantitative SPECT data interpretation in phantoms and in-vivo. This method is also evaluated in dynamic SPECT imaging.
In the final chapter, we draw an overall conclusion and give an outlook for possible future developments and optimization approaches in this field of research.

Chapter 2

Background and Significance of SPECT/CT Imaging

2.1 SPECT Image Formation - Physical Principles

Single Photon Emission Computed Tomography is a non-invasive tomographic imaging technique widely used to assess the metabolism of human tissue on a molecular level. It has shown its clinical practicability in many applications across neurology, cardiology, and oncology. SPECT imaging, as opposed to conventional nuclear medicine planar imaging, provides information about the target object in three dimensions.
A gamma-emitting radioisotope is attached to a ligand which has specific chemical binding properties to certain types of human tissues. This radiopharmaceutical is injected in the patient's blood stream and accumulates in the target regions within the body. Gamma rays are emitted from these regions and collected by an external detector system, also called gamma camera. For tomographic imaging, the gamma cameras (usually two) rotate around the patient and collect a set of two-dimensional (2D) projection images, which are reconstructed to a three-dimensional (3D) image using certain post-processing techniques. The principles of the entire SPECT image formation chain including instrumentation, projection data generation, and reconstruction are explained in detail in this chapter.

2.1.1 Gamma Camera

The first gamma camera was developed by Anger in 1964 [1]. The key components of the gamma camera are the collimator, the scintillation crystal, the photomultiplier tubes (PMT), and the signal processing electronics. A schematic layout of the camera assembly is shown in Figure 2.1 left.
The collimator is a pattern of holes made of lead or other γ-ray absorbing material. It is responsible for the projection of the source distribution onto the detector crystal by restricting the passage of the photons (absorptive projection). In the case of parallel collimation, only those photons traveling perpendicular to the detector reach the crystal. The shape and geometry of the holes vary depending on the imaging

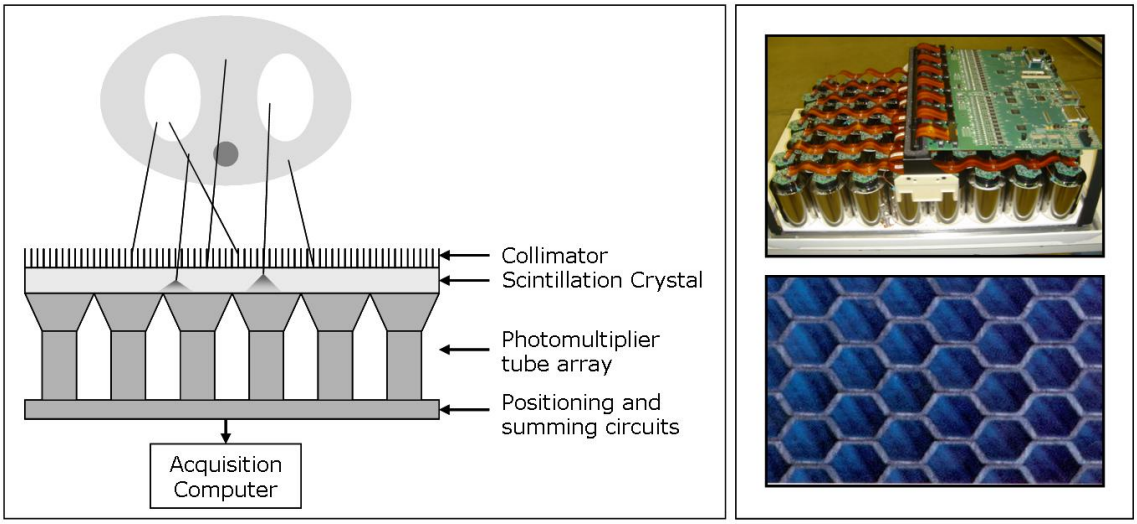

Figure 2.1: Left: The key components of a gamma camera; Right-top: A rectangular gamma camera detector with the cover removed showing the array of photomultiplier tubes attached to the NaI(Tl) crystal; Right-Bottom: A enlarged sample of a parallel hole collimator; (Courtesy of Siemens Healthcare)

objective. Figure 2.1 right-bottom shows an enlarged sample of a uniform septa parallel-hole collimator (BiCORE™, Siemens Healthcare).
The scintillation crystal is made of thallium activated sodium iodine (NaI(Tl)) in almost all commercial systems. It absorbs the incoming photons via photoelectric effect and produces a flash of light at the point of interaction. The light intensity is proportional to the energy of the interacting photon. Photomultiplier tubes detect the light flash and convert it to pulses of electric current. The signal processing electronics amplify and analyze the pulses from the PMT array and determine the energy of the absorbed photon and the location of interaction. The uncertainties of both energy and location of the absorbed photons are referred to as energy resolution and spatial resolution of the detector. The typical intrinsic resolution of a large field of view gamma camera in clinical use is the range of 4 mm (full width at half maximum, FWHM). The typical energy resolution is in the range of 10% of the photon energy. Figure 2.1 right shows a picture of a rectangular gamma camera detector with an array of 59 PMTs mounted on the scintillation crystal. The total field of view (FOV) is 53.3 $\times$ 38.7 cm (Data courtesy of Siemens Healthcare).

2.1.2 The Projection Characteristics in SPECT

The generation of projection data in SPECT is unique for this modality and will be described in more detail in this section. We start with the general principle of projection data generation typical for parallel beam Computed Tomography (CT) and add the specifics for SPECT imaging later.
The image formation in parallel beam CT is based on a fundamental relationship between the image space (object space) and the data space (projection space). This

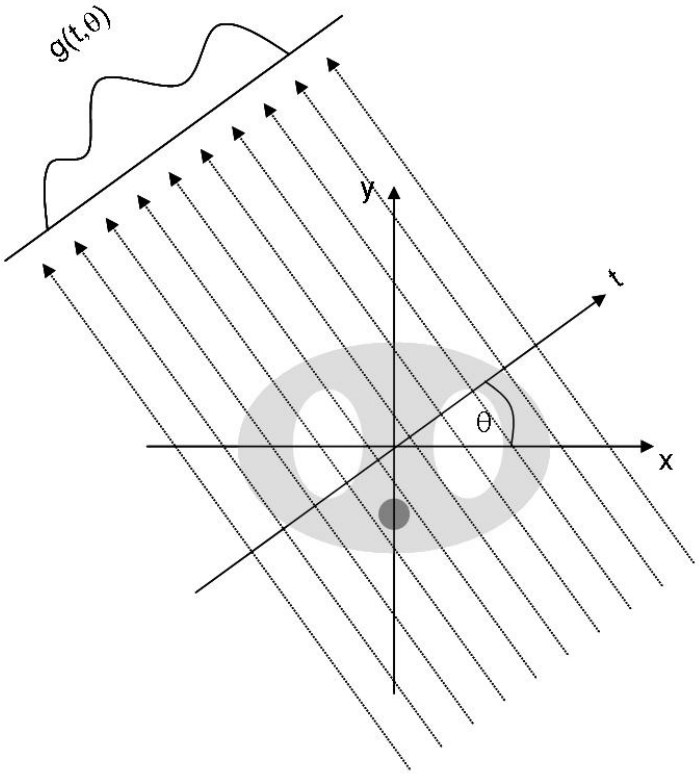

Figure 2.2: The relationship between image space $f(x, y)$ and data space $g(t, \theta)$ in the case of parallel projection

relationship is described by the radon transform [2]. For a 2D image space it can be written as follows:

$$g(t, \theta) = \iint f(x, y)\, \delta(x \cos\theta + y \sin\theta - t)\; dxdy \;, \tag{2.1}$$

where $f(x, y)$ is the representation of the object in image space, $\delta(\ldots)$ is the Dirac delta function, and $g(t, \theta)$ is the projection data with t being the detector coordinate and θ the projection angle. Each value in data space is equal to the value of a specific line integral in image space, as shown in Figure 2.2. For a simple parallel projection generation process, the inverse Radon transform describes the mapping from data space back to image space also referred to as reconstruction.

In SPECT imaging the relationship between image space and data space is not as simple as described by the Radon transform. Various effects inherent to the image formation chain contribute to a more complex projection operator in SPECT. In the following, the key image degrading factors are discussed.

Collimator Characteristics

In the case of ideal parallel collimation all photons traveling not perpendicular to the detector are absorbed while all photons traveling perpendicular to the detector pass

through without any interactions. In this ideal case the collimator efficiency, which is the number of γ-rays passing through the collimator per γ-ray emitted from the source toward the collimator, is 100% and the collimator resolution is infinitesimal. In practice, the collimator is not ideal and there is a trade-off between efficiency and resolution.
The collimator holes have finite width and length. Thus, photons not traveling perpendicular to the collimator but still traveling within a certain acceptance angle pass through the collimator, as shown in Figure 2.3(a). As a result the spatial resolution of the collimator is distance dependent. With increasing distance of a point source to the collimator the photons pass freely through an increasing number of collimator holes and are detected over a larger area of the detector. Figure 2.3(b) shows the principle of this point spread function (PSF).
The collimator resolution r_{Coll} is given by the FWHM of the radiation profile of a point source projected by the collimator onto the detector (see 2.3(b)). It can be calculated as follows [3]:

$$r_{Coll} \approx d(l_{eff} + b)/l_{eff} \ , \tag{2.2}$$

where b is the distance from the source to the collimator, d is the hole diameter and $l_{eff} = l - 2\mu_l{}^{-1}$ is the effective length of the collimator holes. μ_l is the linear attenuation coefficient. The effective length accounts for the effect of septal penetration.
r_{Coll} decreases with the decrease of the hole diameter d and the increase of the effective hole length l_{eff}.
The collimator efficiency e_{Coll} can be calculated as follows [3]:

$$e_{Coll} \approx K^2(d/l_{eff})^2[d^2/(d + t_s)^2] \ , \tag{2.3}$$

where K is a constant dependent on the hole shape (~ 0.26 for hexagonal and ~ 0.24 for round holes) and t_s is the septal thickness.
The ratio d/l_{eff} affects the collimator efficiency quadratically. An approximate relationship between collimator resolution and collimator efficiency is:

$$e_{Coll} \propto (r_{Coll}^2) \ . \tag{2.4}$$

Nonuniform Attenuation

Photons that follow a straight line from the point of origin through the collimator and deposit their full energy in the detector crystal are most useful for SPECT imaging. Attenuation is the decimation of these useful photons due to interactions with matter when passing trough objects between the point of origin and the detector. In SPECT imaging, with typical photon energies between 80 keV and 500 keV, there are two major effects: Photoelectric absorption and Compton scattering. In photoelectric absorption the incident photon is fully absorbed by an atom. In Compton scattering the photon collides with an orbital electron and is deflected by a scattering angle. The intensity of a collimated beam with an initial intensity I_0 exiting a given material of thickness x is:

$$I(x) = I_0 e^{-\mu_l x} \ , \tag{2.5}$$

where μ_l is the linear attenuation coefficient which depends on the material and the photon energy. The value of μ_l also depends on the measurement geometry. Narrow

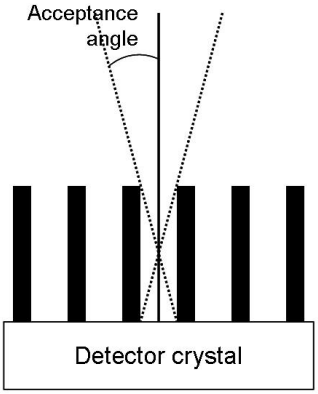

(a) Collimator acceptance angle

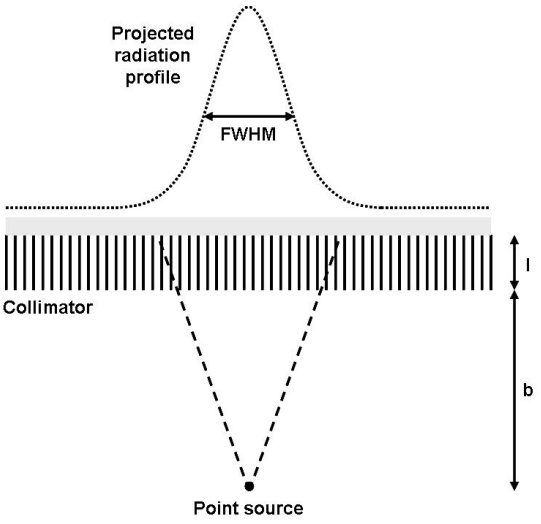

(b) Radiation profile of a point source (Point Spread Function). The full width at half maximum (FWHM) is used to characterize the collimator resolution

beam geometry postulates a highly collimated photon beam without scattering. If the measurement is made with a broad beam geometry scattered photons from direction other than the beam are detected and increase the measured intensity. The narrow and broad beam values for 140 keV photons in water are 0.15 cm^{-1} and ~0.12 cm^{-1}, respectively [4]. Linear attenuation coefficients in the human body range from almost zero, for air, to approximately 0.28 cm^{-1}, for cortical bone (140 keV), and their distribution is highly inhomogeneous across the body. This postulates proper attenuation correction techniques for SPECT imaging in clinical practice.

Scatter

A fraction of the photons that travel through the body is scattered in the tissue and looses energy. The energy loss depends on the scattering angle φ:

$$E_{SC} = 1 + \frac{E_0}{m_0 c^2}(1 - \cos\varphi) \ , \tag{2.6}$$

where E_0 is the initial photon energy, E_{SC} the energy after the interaction, m_0 the rest mass energy of the electron, and c is the speed of light. Figure 2.3 shows a typical energy spectrum of 140 keV photons (Tc-99m) in scattering medium. In this case the spectrum was measured during a regular clinical acquisition using a large field of view (FOV) gamma camera (Symbia-T6, Siemens Healthcare) with an energy resolution of 10%. Due to this finite energy resolution a fraction of scattered photons is detected within the peak of the primary photons (photopeak). A 140 keV photon scattered e.g. through an angle of 45° has a remaining energy of 129.5 keV which is within a typical acquisition energy window width of 15%. Scattered photons which are detected carry varying degrees of spatial information and can be characterized by a scatter response function (SRF) which describes the probability with which the

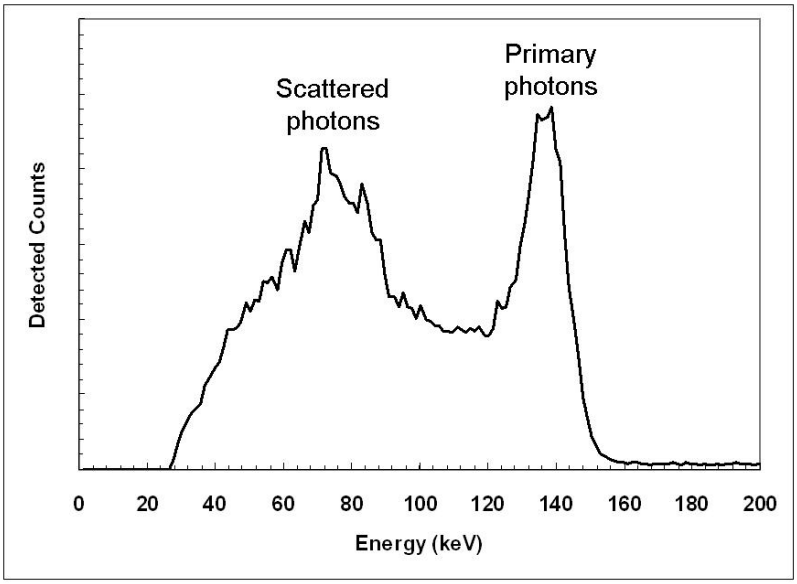

Figure 2.3: Typical energy spectrum of 140 keV photons in scattering media (clinical acquisition of a human torso using Tc-99m-diphosponate). The spectrum was generated using a large field of view gamma camera (Symbia-T6, Siemens Healthcare) with an energy resolution of 10%.

scattered photons originating from a point in the object are detected in a specific detector position. The SRF is non-stationary and depends on the source location, the photon energy, and the composition of the material [5, 6, 7].

2.1.3 The SPECT System Model

It was mentioned earlier (Section 2.1.2) that the Radon transform (Equation (2.1)) represents the relationship between the image space $f(x, y)$ and the data space $g(t, \theta)$ for an ideal parallel projection geometry. This relationship can also be written using a linear operator $\mathbf{A}$:

$$\mathbf{g} = \mathbf{A}\mathbf{f} \iff g(t,\theta) = \iint a(t,\theta,x,y)\, f(x,y)\; dxdy \;, \tag{2.7}$$

where $\mathbf{A}$ is called the system operator which models the imaging system (here in 2D). For the ideal case of the Radon transform $\mathbf{A}$ is:

$$a(t,\theta,x,y) = \delta(x\cos\theta + y\sin\theta - t) \;. \tag{2.8}$$

As discussed in Section 2.1.2, real SPECT systems have finite spatial resolution. This can be accounted for in the system model using a detector response function $d(t, \theta, x, y)$ at a particular position (x, y) in the object. In addition, the attenuation factor $c(x, y)$ experienced at position (x, y) can be included in the system operator. If both detector response and attenuation are modeled Equation (2.1) can be written as follows:

$$\mathbf{g} = \mathbf{A}_{d,c}\mathbf{f} \iff g(t,\theta) = \iint f(x,y)\, c(x,y)\, d(x\cos\theta + y\sin\theta - t)\; dxdy \;. \tag{2.9}$$

In the definitions above the parameters x, y, t, and θ were assumed to be continuous. In practice, however, tomographic imaging devices can only acquire a finite number of data points collected over a finite number of angular views and reconstruction algorithm can only estimate a finite number if image intensity parameters. Therefore, discrete representations are used. The discrete representations for data space and image space are $\mathbf{g}$ and $\mathbf{f}$ with detector elements g_i and image voxels f_j where $i = 1, 2, \ldots, P$ and $j = 1, 2, \ldots, N$. Thus, the operator $\mathbf{A}$ becomes a matrix with dimension $P \times N$. Each element a_{ij} represents the probability that a photon detected in the ith detector element originated from the jth volume element (voxel). For SPECT systems this matrix is full-rank yet ill-conditioned, so inversion is non-trivial.
Due to randomness in activity distribution, activity decay, and photon counting, SPECT projection measurements are treated as Poisson distributed independent random variables [8]:

$$\mathbf{G} \sim Poisson\left\{\mathbf{Af} + \varsigma\right\} \ , \tag{2.10}$$

where $Poisson\left\{\lambda\right\}$ is the Poisson distribution with mean λ and ς denotes additive scattered counts. At this point we assume that scattered counts are additive even though scatter can also be incorporated in the system matrix by calculating the SRF e.g. by using Monte-Carlo simulations [9].
In order to generate 3D information from the data, image reconstruction tries to estimate the real image $\mathbf{f}$ given the data $\mathbf{g}$ as a realization of the random vector $\mathbf{G}$. The concept of image reconstruction will be discussed in the following section.

2.2 Tomographic Image Reconstruction in SPECT

As shown in the previous section, the tomographic data $\mathbf{g}$ produced by a SPECT camera is a set of projections through the object $\mathbf{f}$. This data cannot be used in its raw form for medical diagnosis. It would be a challenging task for a human observer to reliably detect small abnormalities and determine their exact positions by examining the projection views only. Thus, image reconstruction methods are required to map the observed data $\mathbf{g}$ to an image estimate $\hat{\mathbf{f}}$.

2.2.1 Filtered Backprojection

The most basic approach for obtaining an image estimate from the observed data is to use the inverse of the Radon transform (Equation (2.1)):

$$\hat{f}(x,y) = \int_0^\pi g\left(x\cos\theta + y\sin\theta, \theta\right)\, d\theta \tag{2.11}$$

The backprojection distributes each projection back across the image grid along the direction of the respective projection angle and integrates the result over all angles. It can be shown that the simple backprojection yields a blurred image estimate [3]:

$$\hat{f}(x,y) = f(x,y) \;*\; \frac{1}{|r|}\;, \tag{2.12}$$

where $r = \sqrt{x^2+y^2}$ is the radial distance and $*$ represents the appropriate convolution which is 2D in this case. This so called 1/r blurring can be avoided by applying a ramp filter to the projections in frequency domain:

$$\acute{G}(\omega_t,\theta) = |\omega_t|\, G(\omega_t,\theta)\;, \tag{2.13}$$

where

$$G(\omega_t,\theta) = \mathcal{F}[g(t,\theta)] \tag{2.14}$$

is the Fourier transform of the projection data. With

$$\acute{g}(t,\theta) = \mathcal{F}^{-1}[\acute{G}(\omega_t,\theta)] \tag{2.15}$$

the formula for the *Filtered Backprojection* (FBP) can be written as:

$$f(x,y) = \int_0^\pi \acute{g}\left(x\cos\theta + y\sin\theta, \theta\right)\, d\theta \tag{2.16}$$

Note that FBP reconstruction with perfectly measured noise-free data yields the exact value of the true object distribution $f(x,y)$. The ramp filter in frequency domain emphasizes high frequencies and suppresses low frequencies. This eliminates 1/r blurring, yet amplifies high frequency noise. Since there is usually little signal in the highest frequencies of a nuclear medicine image, filters that roll off gradually at higher frequencies, such as e.g. Shepp-Logan [10], Hann [11], or Butterworth [12], are used in practice. The filter cut-off frequency is an important parameter to set. For FBP reconstruction it is usually defined in the spatial domain and given in cycles/pixel or as a multiple of the Nyquist frequency ($f_{Nyquist} = 0.5\, cycles/pixel$). We will expand on the impact of the cut-off value on image quality in Chapter 3.

2.2.2 Statistical Image Reconstruction

In SPECT clinical practice FBP is still a widely used method for image reconstruction and recommended by major nuclear medicine communities [13, 14, 15]. However, FBP in general does not account for depth-dependent blur or scattered photons and has limited capabilities in terms of attenuation correction. If optimal corrections for image degradations are needed, iterative image reconstruction is to be used [15]. It was shown e.g. by Gilland et al. [16], Tsui et al. [17, 18], and Rosenthal et al. [19] that these corrections reduce errors for absolute quantification in SPECT imaging. Both the availability of fast computers at low cost as well as advances in efficient processing allow the use of computationally expensive iterative methods in clinical routine [14]. Ordered Subset Expectation Maximization (OSEM) [20], an accelerated version of the Maximum Likelihood Expectation Maximization (MLEM) method [21], is often the iterative method of choice.
In the following, the concept of iterative reconstruction based on MLEM is discussed in more detail.

The EM Algorithm in Emission Tomography

The expectation maximization (EM) algorithm was first proposed in 1977 by Dempster et al. [22]. It was adapted to the reconstruction problem in emission computed tomography (ECT) by Lange et al. [23] and Shepp et al. [21] as Maximum Likelihood Expectation Maximization (MLEM) reconstruction.
The EM algorithm is an iterative method for solving maximum likelihood (ML) estimation problems when missing or latent information is involved. It consists of two alternating steps which are repeated until convergence: The expectation step (E-step) and the maximization step (M-step).
The key equation of the EM algorithm describes the relationship between some observable information and complete information given an estimated parameter set $\hat{\mathbf{B}}^{(n+1)}$ in iteration step $(n+1)$:

$$\ln\, p(x;\hat{\mathbf{B}}^{(n+1)}) = \ln\, p(x,y;\hat{\mathbf{B}}^{(n+1)}) - \ln\, p(y|x;\hat{\mathbf{B}}^{(n+1)})\ , \tag{2.17}$$

with x being the observed data, y the hidden data and $\ln\, p(\cdots,\hat{\mathbf{B}}^{(n+1)})$ the log-likelihood function. In words, Equation (2.17) states that the observed information is equal to the complete information minus the hidden information. By multiplying Equation (2.17) with $p(y|x;\hat{\mathbf{B}}^{(n)})$ and integrating over y we get:

$$\begin{aligned}&\int p(y|x;\hat{\mathbf{B}}^{(n)})\ \ln\, p(x;\hat{\mathbf{B}}^{(n+1)})\, dy = \\ &\int p(y|x;\hat{\mathbf{B}}^{(n)})\ \ln\, p(x,y;\hat{\mathbf{B}}^{(n+1)})\, dy - \int p(y|x;\hat{\mathbf{B}}^{(n)})\ \ln\, p(y|x;\hat{\mathbf{B}}^{(n+1)})\, dy\end{aligned} \tag{2.18}$$

The left hand side of Equation (2.18) remains the log-likelihood function of the observed data $\ln\, p(x;\hat{\mathbf{B}}^{(n+1)})$ after integrating over y. The right hand side of the equation can be written as:

$$Q\left(\hat{\mathbf{B}}^{(n)};\hat{\mathbf{B}}^{(n+1)}\right) + H\left(\hat{\mathbf{B}}^{(n)};\hat{\mathbf{B}}^{(n+1)}\right)\ , \tag{2.19}$$

where $Q(\hat{\mathbf{B}}^{(n)}; \hat{\mathbf{B}}^{(n+1)})$ is the so called *Q-function* or *Kullback-Leibler statistics* and $H(\hat{\mathbf{B}}^{(n)}; \hat{\mathbf{B}}^{(n+1)})$ is the entropy with

$$Q\left(\hat{\mathbf{B}}^{(n)}; \hat{\mathbf{B}}^{(n+1)}\right) = \int p(y|x; \hat{\mathbf{B}}^{(n)}) \ln p(x, y; \hat{\mathbf{B}}^{(n+1)})\, dy \tag{2.20}$$

$$H\left(\hat{\mathbf{B}}^{(n)}; \hat{\mathbf{B}}^{(n+1)}\right) = -\int p(y|x; \hat{\mathbf{B}}^{(n)}) \ln p(y|x; \hat{\mathbf{B}}^{(n+1)})\, dy \tag{2.21}$$

Instead of maximizing the likelihood of the observed data, the EM algorithm maximizes the Q-function which also can be written as a conditional expectation of the complete data given the observed data:

$$\begin{aligned} Q\left(\mathbf{B}; \mathbf{B}'\right) &= \int p(y|x; \mathbf{B}) \ln p(x, y; \mathbf{B}')\, dy \\ &= E\left[\ln p(x, y; \mathbf{B}') \mid x, \mathbf{B}\right] \end{aligned} \tag{2.22}$$

At this point we can define the data variables which are used in the case of emission tomography [24]:
The observed projection data (or incomplete data) are denoted by $\mathbf{g}$. The projection data are incomplete because the exact location of the origin of the photons collected in each detector element i is unknown. According to Equation (2.7) the counts in each detection bin are projected from the object $\mathbf{f}$ in a way described by the system matrix $\mathbf{A}$. Each element a_{ij} in the system matrix, which is primarily defined by the imaging geometry and imaging physics, can be seen as the probability of detecting a photon in detector pixel i originated from voxel j. The data $\mathbf{g}$ would be complete if we knew not only the count values in each detection bin but also how many of these counts originated from each voxel k in the object. The full complement of data we wish we had (complete data) are denoted by $\mathbf{s}$ with elements s_{ik} with $k \in J_i$ where J_i denotes the set of voxels contributing to detector bin i. Each element s_{ik} is the number of photons emitted in voxel k and detected in detection bin i.
With this definition of the data we can formulate the EM algorithm for SPECT. The E-step of the EM algorithm computes the expectation (Equation (2.22)) based on the current image estimate $\hat{\mathbf{f}}^{(\mathbf{n})}$:

$$Q\left(\mathbf{f}; \hat{\mathbf{f}}^{(\mathbf{n})}\right) = E\left[\ln p\left(\mathbf{s}; \mathbf{f}\right) \mid \mathbf{g}; \hat{\mathbf{f}}^{(\mathbf{n})}\right] , \tag{2.23}$$

The M-step calculates the next image estimates $\hat{\mathbf{f}}^{(\mathbf{n+1})}$ by maximizing $Q(\mathbf{f}; \hat{\mathbf{f}}^{(\mathbf{n})})$:

$$\hat{\mathbf{f}}^{(\mathbf{n+1})} = \arg\max_f Q\left(\mathbf{f}; \hat{\mathbf{f}}^{(\mathbf{n})}\right) . \tag{2.24}$$

The relationship between the complete data $\mathbf{s}$, observed data $\mathbf{g}$, and the image $\mathbf{f}$ is as follows:

$$g_i = \sum_{k \in J_i} s_{ik} \tag{2.25}$$

$$E\left[s_{ik}\right] = a_{ik} f_k . \tag{2.26}$$

In emission tomography the data are independent Poisson distributed random variables. The basic Poisson model provides the probability of measuring a particular count c given an expected measurement λ:

$$p(c;\lambda) = \frac{\lambda^c e^{-\lambda}}{c!} \tag{2.27}$$

The conditional probability of acquiring the measured projection count distribution $\mathbf{g}$ for a given activity distribution $\mathbf{f}$, also called the likelihood, is the product of the probabilities for the individual detector bins:

$$p(\mathbf{g};\mathbf{f}) = \prod_i \frac{E\left[g_i\right]^{g_i} e^{-E[g_i]}}{g_i!} \ , \tag{2.28}$$

where

$$E\left[g_i\right] = \sum_j a_{ij} f_j \ . \tag{2.29}$$

The likelihood function of the complete data is therefore:

$$p(\mathbf{s};\mathbf{f}) = \prod_i \prod_k \frac{E\left[s_{ik}\right]^{s_{ik}} e^{-E[s_{ik}]}}{s_{ik}!} \ . \tag{2.30}$$

Accordingly the log-likelihood function is:

$$\ln p(\mathbf{s};\mathbf{f}) = \sum_i \sum_k \left[s_{ik} \ln\left(E\left[s_{ik}\right]\right) - E\left[s_{ik}\right] - \ln\left(s_{ik}!\right)\right] \tag{2.31}$$

and using Equation (2.26) we can write Equation 2.31 as a function of s_{ik}, a_{ik}, and f_k:

$$\ln p(\mathbf{s};\mathbf{f}) = \sum_i \sum_k \left[s_{ik} \ln\left(a_{ik} f_k\right) - a_{ik} f_k - \ln\left(s_{ik}!\right)\right] \ . \tag{2.32}$$

E-step

With the likelihood function defined we can compute the E-step of the EM algorithm:

$$\begin{aligned} Q\left(\mathbf{f};\hat{\mathbf{f}}^{(\mathbf{n})}\right) &= E\left[\ln p\left(\mathbf{s};\mathbf{f}\right) \mid \mathbf{g};\hat{\mathbf{f}}^{(\mathbf{n})}\right] \\ &= \sum_i \sum_k \left\{ E\left(s_{ik} \mid \mathbf{g};\hat{\mathbf{f}}^{(\mathbf{n})}\right) \ln\left(a_{ik} f_k\right) - a_{ik} f_k - E\left[\ln\left(s_{ik}!\right)\right] \right\} \end{aligned} \tag{2.33}$$

The expectation value of s_{ik} given the measured data and the current image estimate is:

$$E\left[s_{ik} \mid \mathbf{g};\hat{\mathbf{f}}^{(\mathbf{n})}\right] = \frac{a_{ik}\hat{f}_k^{(n)}}{\sum_j a_{ij}\hat{f}_j^{(n)}} g_i \stackrel{def}{=} q_{ik} \ , \tag{2.34}$$

which is the fraction of the counts in pixel i expected to have originated from voxel k given that the current image estimate $\hat{\mathbf{f}}^{(\mathbf{n})}$ is the source of the counts. From substituting Equation (2.34) in Equation (2.33) it follows:

$$Q\left(\mathbf{f};\hat{\mathbf{f}}^{(\mathbf{n})}\right) = \sum_i \sum_k \left\{q_{ik} \ln\left(a_{ik} f_k\right) - a_{ik} f_k - E\left[\ln\left(s_{ik}!\right)\right]\right\} \ . \tag{2.35}$$

M-step

The M-steps finds the new image estimate $\hat{\mathbf{f}}^{(\mathbf{n+1})}$ by maximizing $Q(\mathbf{f};\hat{\mathbf{f}}^{(\mathbf{n})})$ with respect to $\mathbf{f}$.
The partial derivative of the Q-function is:

$$\frac{\partial Q(\mathbf{f};\hat{\mathbf{f}}^{(\mathbf{n})})}{\partial f_j} = \sum_i \left(\frac{q_{ij}}{\hat{f}_j^{n+1}} - a_{ij}\right) \stackrel{!}{=} 0 \tag{2.36}$$

By using Equation (2.34) and solving for $\hat{f}_j^{n+1}$ the well-known iterative expression for the MLEM algorithm is obtained:

$$\hat{f}_j^{(n+1)} = \frac{\hat{f}_j^{(n)}}{\sum\limits_i a_{ij}} \sum_i a_{ij} \frac{g_i}{\sum\limits_j a_{ij} \hat{f}_j^{(n)}} \tag{2.37}$$

In practice, Equation (2.37) is implemented using a pair of forward and back projectors. Each voxel of the current image estimate $\hat{\mathbf{f}}_{\mathbf{k}}^{(\mathbf{n})}$ is forward projected using the known system matrix $\mathbf{A}$ to obtain an estimated projection data set (denominator of the second fraction). The estimated projections are divided into the measured projections and the ratio is backprojected, denoted by the sum over i. This correction term is multiplied to the current image estimate and normalized by the backprojection of ones. A schematic overview of the iterative process in SPECT reconstruction is shown in Figure 2.4. The OSEM algorithm [20] is an accelerated version of the MLEM algorithm. In MLEM, the image is updated after all projection angles have been processed. OSEM updates the image after a subset of projections has been processed. One iteration is completed once the entire projection data set is processed and the total number of updates is the number of subsets times the number of iterations. The acceleration is proportional to the number of subsets.

2.2.3 Correction Techniques for SPECT Physical Effects

As detailed in the previous section, FBP reconstruction provides an exact analytical solution for the reconstruction problem by inverting the Radon transform. However, we mentioned earlier that the inversion of the Radon transform is only part of the problem. Photon attenuation, scatter, and distance dependent resolution corrupt the projection images. As a result, FBP reconstructed images do not represent the true source distribution, even in the absence of noise.
Even though corrections for image degrading factors can in part also be incorporated

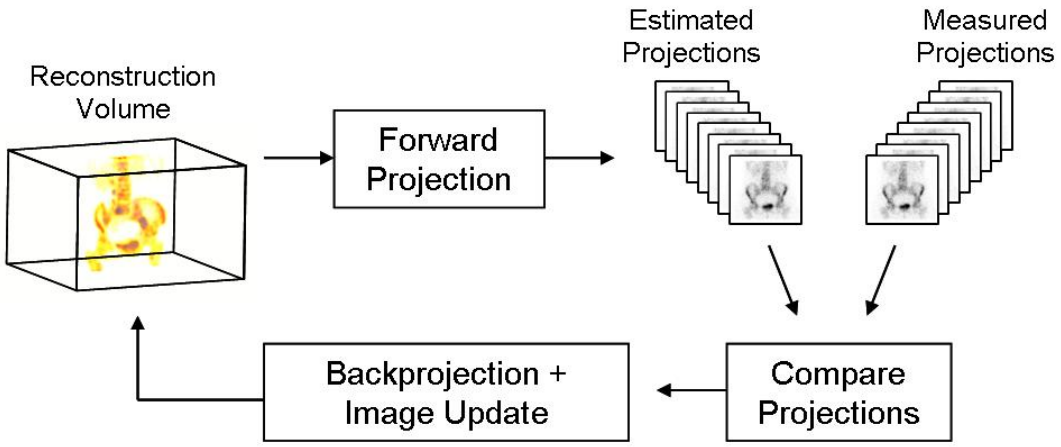

Figure 2.4: A schematic overview of the principle of iterative reconstruction in SPECT.

into FBP reconstruction (see e.g. [25, 26]), we focus on the practical implementation of these correction techniques within iterative reconstruction.

Non-uniform Attenuation Correction

A fundamental part of attenuation correction is to accurately determine the patient-specific distribution of linear attenuation coefficients, also called attenuation map or μ-map. There are three different strategies for the estimation of this map. One can either calculate the values from emission data directly, use a transmission source in combination with the gamma camera employed for emission imaging, or import maps from different modalities e.g. CT [27]. In this work we focus on the latter method, since co-registered CT data is available for all the performed experiments and patient studies.
CT inherently provides patient-specific measurements of the linear attenuation coefficients at each point in the image. However, these measurements are performed at the X-ray energy of the CT scanner, which generates a polychromatic X-ray beam with a mean energy of 50-80keV, depending on the peak tube voltage. Therefore, the linear attenuation coefficients obtained from the CT scan need to be converted to those corresponding to the energy of the emission photons. This is usually done using a piecewise linear fit to pairs of HU and known attenuation coefficients of the calibration materials (e.g. water, bone) [27, 28, 29, 30].
Once the μ-map is calculated, it can be incorporated into the reconstruction algorithm. Numerous algorithms for attenuation correction have been developed. Analytical approaches for non-uniform attenuation correction were e.g. proposed by Liang et al. [31] and Glick et al. [25] and the inversion of the Radon transform in the general case of non-uniform attenuation has been solved by Natterer [32]. A commonly used method in combination with FBP reconstruction is the Chang algorithm [33] which assumes uniform attenuation and is applied as a post-processing step. It is mainly used for FBP in clinical routine because it is fast, straightforward, and leads

to acceptable results in regions with quasi-uniform attenuation e.g. the brain [34]. The MLEM/OSEM method is the iterative method of choice in clinical practice. It proved a high degree of accuracy when compensating for attenuation using non-uniform μ-maps [35]. As indicated in Equation (2.9) the effects of photon attenuation can be incorporated into the system matrix $\mathbf{A}$ of the iterative algorithm. In practice, an attenuated projector-backprojector pair is used for the forward and backward projection operations in the iterative process of Equation (2.37) [36]. The attenuated projection operation can be written as:

$$g(t,\theta) = \sum_j f_j \exp\left[-\int_{r_{j+1}}^{\infty} \mu(r)\, dr\right] \int_{r_j}^{r_{j+1}} \exp\left[-\mu_j(r_{j+1}-r)\right]\, dr \ , \tag{2.38}$$

where r_j and r_{j+1} are the positions of the edges of voxel j through which the projection ray passes in direction of r perpendicular to the detector ($r = -x\sin\theta + y\cos\theta$). The first exponential term represents the attenuation of a photon emitted from position r_{j+1} (voxel edge towards the detector) and the second term accounts for attenuation across the voxel.
In general, the backward projection should be the transpose operation to the forward projection. However, Zeng et al. [37] showed that in some cases it is beneficial to use an unmatched projector-backprojector pair e.g. to speed up computation.
Figure 2.5 illustrates the effect of non-uniform attenuation correction using the example of a patient injected with a Tc-99m labeled somatostatin receptor-binding peptide (Tc-99m-SMS). Images were acquired on a SPECT/CT hybrid camera at the Clinic of Nuclear Medicine, University of Erlangen-Nuremberg. The CT image (A), the corresponding attenuation map (B), and MLEM/OSEM reconstructed images without (C) and with (D) attenuation correction are shown.

Detector and Collimator Response Correction

In addition to non-uniform attenuation, the distance dependent detector response can be modeled in the iterative reconstruction. The detector response function (DRF) in SPECT has four components: the intrinsic response due to finite resolution of the detection system, the geometric collimator response, and the septal penetration and septal scatter response [38]. The general form of the detector response function can be written as:

$$d(t,D) = i(t) \ * \ (g_C(t,D) + p_S(t,D) + s_S(t,D)) \ , \tag{2.39}$$

where D is the distance from the source to the detector plane, $i(t)$ the intrinsic point response function, and $g_C(t,D)$, $p_S(t,D)$, and $s_S(t,D)$ the collimator specific geometric, septal penetration, and septal scatter response functions. Note that the representation of the detector response function in Equation (2.39) is simplified in comparison to the representation in Equation (2.9) because for parallel hole collimators it is often assumed to be invariant in planes parallel to the detector plane and independent of projection angle θ. This property can be exploited when using rotation based projector-backprojector pairs [39, 40]. For each projection view the image

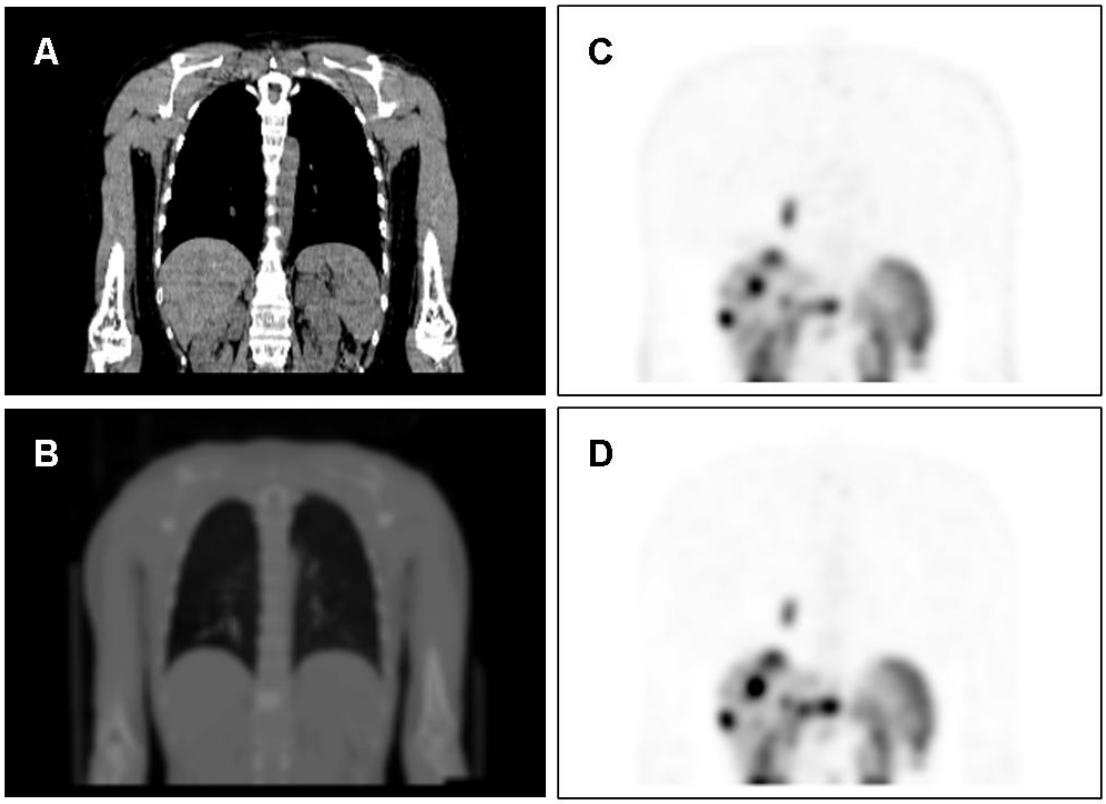

Figure 2.5: Example images of a patient injected with Tc-99-SMS: CT image (A), corresponding μ-map (B), and reconstructed images without (C) and with (D) attenuation correction. Courtesy Clinic of Nuclear Medicine, Erlangen University.

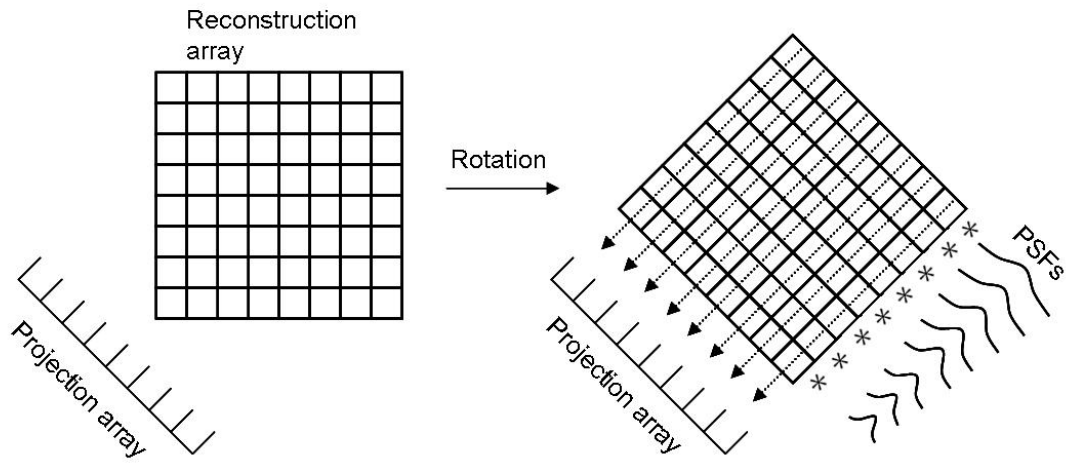

Figure 2.6: Illustration of PSF modeling in the forward projection using a rotation based projector. The image grid is rotated and each image plane parallel to the detector is convolved with the appropriate dector response kernel.

is rotated such that the sampling grid is parallel to the detection plane (see Figure 2.6). The detector response can be modeled by convolving each image plane parallel to the detector with the appropriate detector response kernel. For simplicity septal penetration and septal scatter are often neglected and the detector response function is simply the convolution of intrinsic and geometric collimator response [41]. This function is well approximated by a Gaussian and often described as the basic PSF model in literature [38, 42, 43, 44]. Using a Gaussian, one can model the incremental blurring from one image plane to the next using Gaussian diffusion [42, 45, 46]. Each plane is treated as a 2D image and convolved with a small kernel representing the change in the DRF from plane n to $n-1$, where n is the plane farthest away from the detector. The resulting 2D image is added to the plane $n-1$, which is then blurred with the next incremental kernel and so on. The 2D plane closest to the detector is convolved with the DRF corresponding to the distance to the detection plane. The backprojection is accomplished by performing the steps in the reverse order.

Scatter Correction

Due to the finite energy resolution of scintillation based gamma cameras, a fraction of the detected counts in the photopeak are scattered counts. These scattered counts degrade the spatial information contained in the photopeak window and therefore need to be eliminated. In general, gamma rays can scatter in the patient and in material outside the patient such as the table, the collimator, and the detector. An important step for developing scatter correction methods is the characterization of the scatter response function (SRF) and the estimation of the scatter fraction

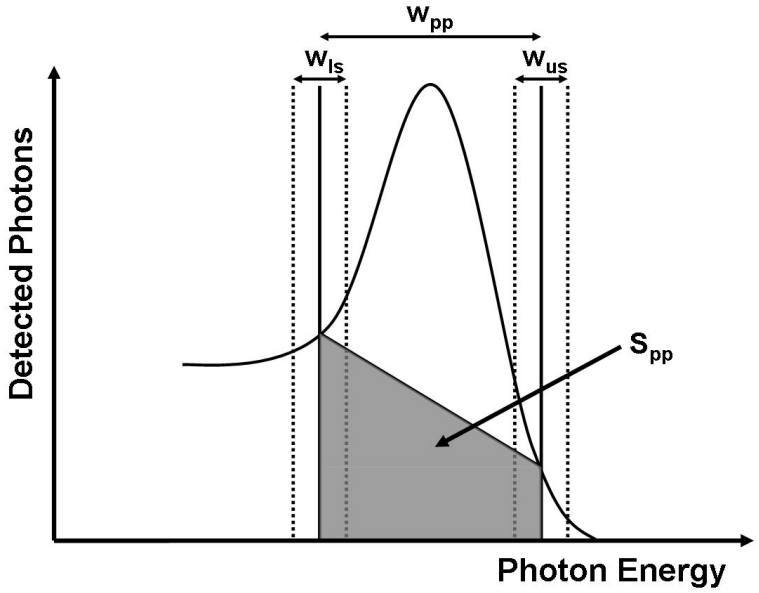

Figure 2.7: Illustration of the estimation of scattered counts in the photopeak using the triple energy window (TEW) method.

in the photopeak. A variety of scatter correction techniques have been proposed. Implicit methods include restriction of the photopeak window [47], specific system calibration [48], or the use of broad-beam attenuation coefficients [4]. Buvat et al. presented a thorough review of explicit methods [49] and a comparative assessment of a subset of these methods based on spectral analysis [50]. Methods based on the analysis of the energy spectrum, such as dual- or triple-energy window (TEW) methods [51, 52, 53], are most commonly used, due to their ease of implementation [54]. Furthermore, the TEW method [52] proved reasonable quantitative accuracy when evaluated using Monte-Carlo simulations [50, 54, 55]. In the TEW method a lower and upper scatter energy window are used in addition to the photopeak window. The number of scattered photons S_{pp} in the photopeak window are estimated as the area of a trapezoidal region in the energy spectrum having a left height of P_{ls}/w_{ls} a right height of P_{us}/w_{us}, and a base of w_{pp} (see Figure 2.7):

$$S_{pp} = \left(\frac{P_{ls}}{w_{ls}} + \frac{P_{us}}{w_{us}} \right) \frac{w_{pp}}{2} \ , \tag{2.40}$$

where $P_{(...)}$ and $w_{(...)}$ are the pixel values and window width of the respective energy window (ls: lower scatter, us: upper scatter, pp: photopeak).

Other commonly used methods are based on transmission-dependent convolution subtraction (TDCS) [56, 57, 58] which operates on the observed projection data using a convolution of a projection estimate with a transmission dependent scatter response function in an iterative process.
Approaches using analytic photon distribution (APD) [59, 60] and reconstruction-based scatter compensation (RBSC) techniques with Monte-Carlo based scatter models [61, 62, 9] were introduced with advances in computational power.

Despite the variety of different scatter estimation methods, dual- and triple-energy window based approaches are most commonly used in SPECT imaging of patients [63, 64].
Once the scatter estimate is derived it can be included in the iterative reconstruction algorithm. For reasons of efficiency a dual matrix approach can be used in which scatter is incorporated only in the forward projection step [65]. Attenuation and detector response are modeled both in the forward and back projection. To further reduce computation time, the scatter estimate is not directly incorporated in the system matrix $\mathbf{A}$ but pre-calculated and introduced in the denominator of the MLEM equation (Equation (2.37)), i.e. the forward projection step:

$$\hat{f}_j^{(n+1)} = \frac{\hat{f}_j^{(n)}}{\sum_i a_{ij}} \sum_i a_{ij} \frac{g_i}{\sum_j a_{ij} \hat{f}_j^{(n)} + \hat{s}} \ , \tag{2.41}$$

where $\hat{s}$ is the estimate of the scatter component.

2.3 SPECT/CT Clinical Routine

2.3.1 Overview

Nuclear medicine offers a large variety of different applications in diagnosis and therapy. Table 2.1 summarizes common applications where gamma cameras are employed [66]. SPECT acquisitions are performed for both, diagnosis as well as treatment planning and progress monitoring for radiotherapy. Numerous different radio-tracers are available for nuclear medicine procedures and the development of new compounds is an active field of research. Commonly used licensed radio-tracers according to European standards are listed in Table 2.1 for the respective applications (this list does not claim to be exhaustive).
The majority of diagnostic nuclear medicine procedures are cardiac, skeletal, and tumor studies. In 2007 approximately 7.5 million nuclear studies were conducted in Europe every year whereas $\sim 30\%$ were bone, $\sim 26\%$ tumor, and $\sim 11\%$ myocardial studies [67]. In the United States the number of cardiac studies increased from 1% of the total in 1973 to 57% of the total in 2005. In the same period the number of bone and tumor studies quintupled to 20% and 2%, respectively, whereas the percentage of lung, gastrointestinal and brain studies decreased significantly [68]. The total number of diagnostic nuclear procedures in the United States in 2006 was ∼19 million.

2.3.2 Hybrid Imaging

During the past decade, dual-modality imaging has evolved as a method to facilitate the correlation of functional (e.g. SPECT) and anatomical (e.g. CT) medical images. Integrated SPECT/CT systems combine the two imaging modalities in one gantry. During the imaging study, the patient remains on the table which is translated from the SPECT system to the CT scanner. This facilitates the co-registration of morphological and functional information by offering a consistent patient geometry and minimal patient movement. Figure 2.8 shows a state-of-the-art hybrid SPECT/CT system (Symbia-T, Siemens Healthcare) with a dual headed gamma camera system in the front and a CT scanner in the rear of the gantry.
The images are fused after the acquisition for diagnostic evaluation. Recently, Bockisch et al. [69] and Even-Sapir et al. [70] published review articles evaluating the improvements in diagnostic accuracy using hybrid imaging as compared to scintigraphy and CT alone. Bockisch et al. reported significant improvements in lesion classification for SPECT/CT studies of the skeletal system (Tc-99m), thyroid (I-131), and somatostatin receptors (In-111). In addition, the anatomic information provided by the CT was stated to help considerably with foci localization e.g. in preoperative sentinel lymph node detection. Even-Sapir et al. furthermore acknowledged the improved SPECT image quality using CT-maps for attenuation correction.

Diagnosis		
Organ	**Application**	**Radiopharmaceutical**
Endocrine organs	Thyroid Parathyroid Adrenal Endocrine tumors	Tc-99m-Pertechnetate, I-131-NaI Tc-99m-MIBI[1] I-123-MIBG[2] In-111-Octreotide, Tc-99m-SMS[3]
Cardiovascular	Myocardial perfusion Mycardial perfusion/viability Cardiac nerve supply	Tc-99m-MIBI, Tc-99m-Tetrofosmin Tl-201-Cloride I-123-MIBG
Brain	Brain perfusion Dopamine neurotransmission Cerebro-spinal fluid	Tc-99m-HMPAO[4], Tc-99m-ECD[5] I-123-IBZM[6], I-123-FP-CIT[7] In-111-DTPA[8]
Lung	Perfusion Ventilation	Tc-99m-MAA[9] Tc-99m-DTPA
Skeletal system	Bone neoplasm Osseous metastasis Endoprosthesis staging Osteonecrosis Arthritis Osteomyelitis	Tc-99m diphosphonates
Kidney	Perfusion/secretion Morphology Glomerular filtration	Tc-99m-MAG3[10] Tc-99m-DMSA[11] Tc-99m-DTPA
Gastrointestinal	Esophagus Gastric emptying/reflux Liver perfusion Hepatic function	Tc-99m-DTPA, -MAA Tc-99m-DTPA, -MAA Tc-99m-DTPA Tc-99m-HIDA[12]
Miscellaneous	Sentinel lymph node Infection Hematology	Tc-99-colloid Tc-99m-HMPAO leukocyte, antibodies Tc-99m-DTPA erythrocyte
Molecular Radiotherapy		
Benign/malignant thyroid disease Neuroendocrine tumors Radiosynoviorthesis Palliative care		I-131-NaI I-131-MIBG, Ga-68-, Y90-DOTATOC[13] Y-90, Re-186 Sm-153-EDTMP[14]

Table 2.1: Common nuclear medicine applications for the use with gamma cameras in Europe

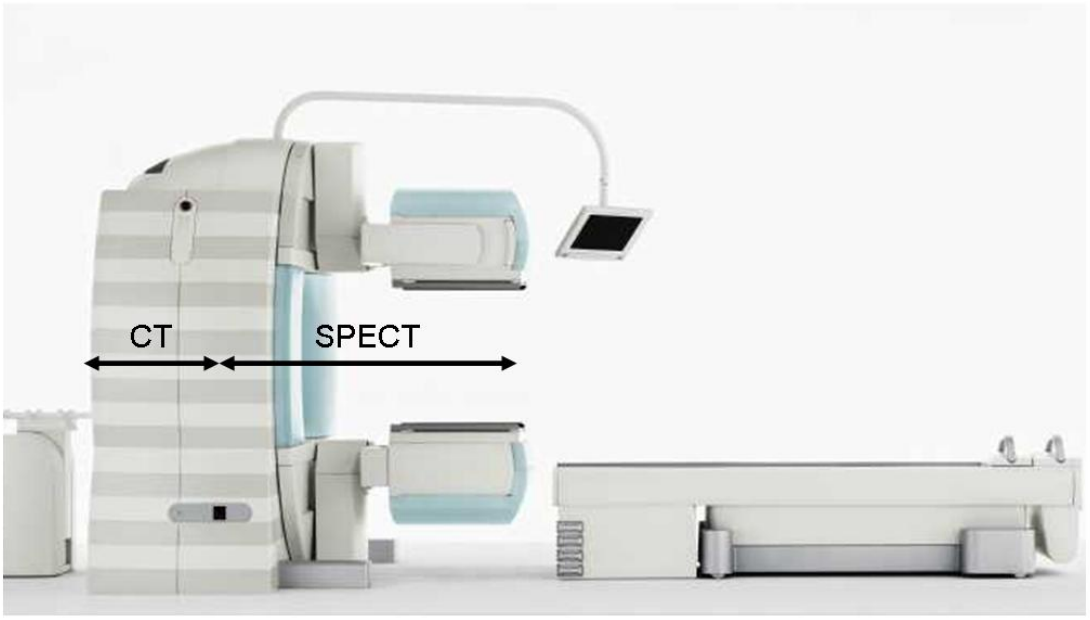

Figure 2.8: State-of-the-art integrated SPECT/CT system with a dual headed SPECT camera (Symbia-T, Siemens Healthcare).

Figure 2.9 shows example patient images for several different SPECT/CT applications: Row **A** shows a Tc-99m somatostatin receptor study of a patient with foci in liver and lung. In row **B** a I-131 thyroid study of a patient with a metastasis in a cervical lymph node is shown. Row **C** shows a Tc-99m diphosponate bone study of a patient with a rib fracture, and row **D** a sentinel lymph node localization study using Tc-99 colloids. Each row contains, from left to right, the reconstructed SPECT image using iterative reconstruction with corrections for attenuation, scatter, and detector response, the CT image, and the fused image. The data was acquired on a Symbia-T6 SPECT/CT system (Siemens Healthcare) at the Clinic of Nuclear Medicine, University Erlangen-Nuremberg.

As discussed in Section 2.2.3, the CT data are used to account for non-uniform attenuation during the reconstruction. The correct conversion from HU units to linear attenuation coefficients on a pixel by pixel basis postulates accurate image registra-

[1]Methoxyisobutylisonitrile
[2]Metaiodobenzylguanidine
[3]Somatostatin receptor binding peptide
[4]Hexamethyl-propyleneamine oxime
[5]Ethyl cysteinate dimer
[6]Benzamide
[7]Ioflupane
[8]Diethylene triamine pentaacetic acid
[9]Macroaggregated albumin
[10]Mercaptylacetyltriglycine
[11]Dimercaptosuccinic acid
[12]N(2,6-Dimethylphenylcarbamoylmethyl) iminodiacetic acid
[13]Tetraazacyclododecane-tetraacetic acid Phe-Tyr-octreotide
[14]Ethylenediaminetetramethylene phosphonic acid

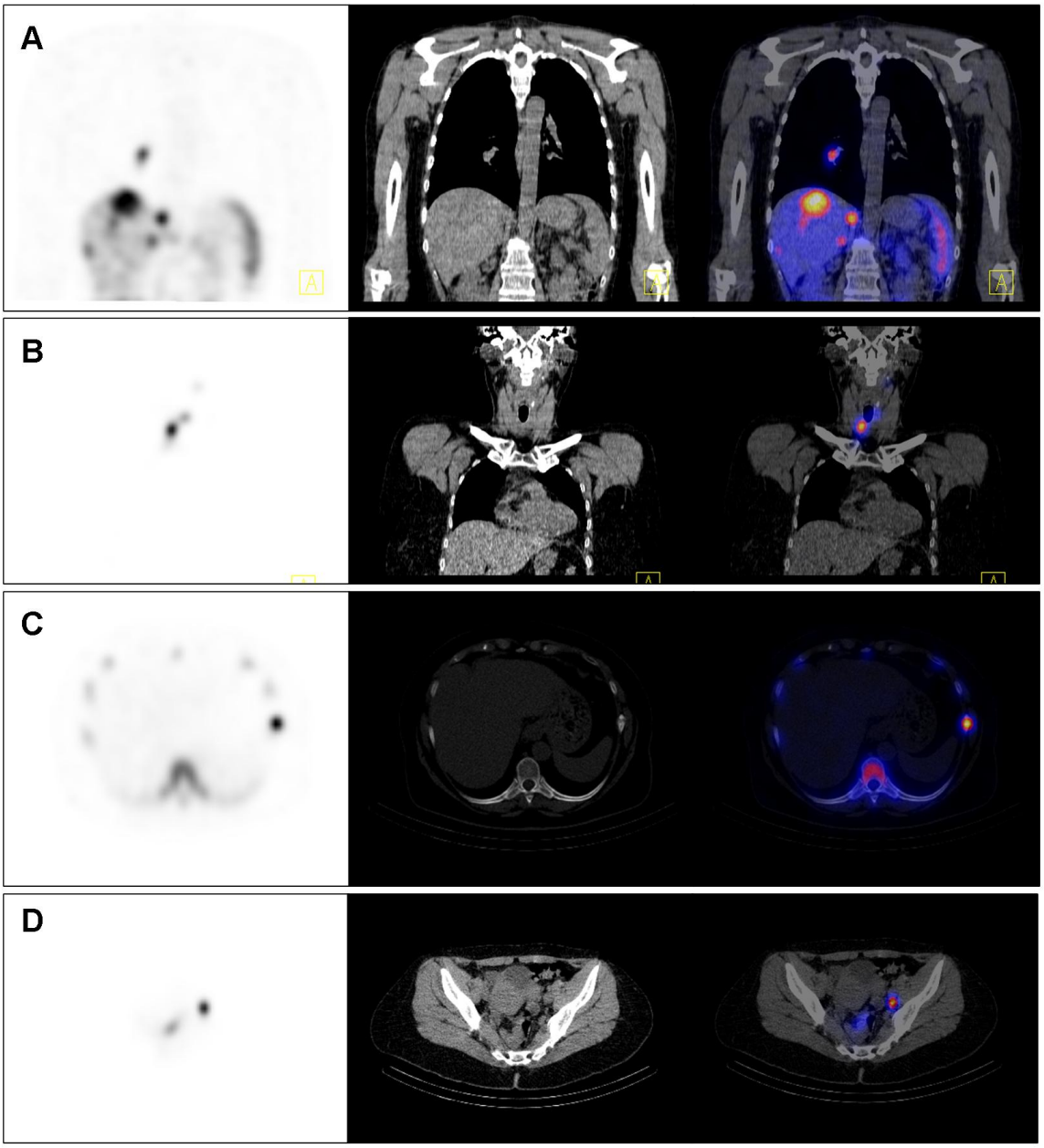

Figure 2.9: Example images from hybrid imaging studies. A: Tc-99m-SMS study with active foci in liver and lung; B: I-131 thyroid study with metastasis in cervical lymph node; C: Tc-99m diphosponate bone study with rib fracture; D: Tc-99m-colloid sentinel lymph node localization. Each row contains the reconstructed SPECT image (left), the CT image (center), and the fused image (right).

tion between the SPECT and CT coordinate system. Accurate registration of in-vivo patient images still remains a challenge due to organ motion in the torso. Yet, it was shown by Noemayr et al. [71] that the registration accuracy of a hybrid system (Symbia-T2, Siemens Healthcare) is within 0.9-1.6 mm in the lower spine region.
Accurate registration is essential for both the correct anatomic localization of foci as well as for the implementation of quantitative procedures. For the latter, attenuation correction and the correct definition of object boundaries is critical. Quantitative SPECT techniques will be discussed in more detail in Section 2.4 and Chapter 5.

2.3.3 SPECT Imaging Protocols and Quality Assurance

The major nuclear medicine communities regularly publish procedural guidelines for various nuclear medicine imaging applications. These guidelines include standard procedures for patient preparation and management, preferred acquisition and reconstruction parameters, quality control procedures, and guidance for image analysis and artifact detection and correction. Table 2.2 gives an overview of SPECT imaging parameters as recommended by the European Association of Nuclear Medicine (EANM) and the Society of Nuclear Medicine (SNM) for some selected applications. In general, the amount of administered radionuclide dose depends on the application and may vary according to the requirements imposed by regulatory authorities (see e.g. [72]). The activity values given in Table 2.2 are baseline values.
Imaging parameters for data acquisition are delimited by the capabilities of the imaging system which vary between manufacturers. Current SPECT imaging systems offer a large variety of different acquisition and reconstruction parameter settings. The manufacturer usually recommends appropriate parameter settings for optimal image quality. The acquisition parameters given in Table 2.2 take the capabilities of current technology into account. Asterisks indicate recommendations provided by the manufacturer in those cases where the respective information was incomplete in the employed guideline.
The overall SPECT imaging time is usually a compromise between counting statistics and the risk of patient movement. For sufficient counting statistics, long imaging times are sometimes needed. Still, the total scan time should not exceed 30-45 minutes [14]. Instrumentation and acquisition parameters need to be adapted accordingly. In the case of myocardial perfusion studies the total scan time is usually between 15-25 minutes [13]. In order to obtain sufficient counting statistics per projection pixel unit (count density), parameters such as matrix size, number of projections, and time per view need to be adapted. For ECG-gated studies either 8 or 16 frames per cardiac cycle are used.
Image reconstruction parameters may also vary depending on tracer characteristics, amount of activity, system and collimator characteristics, and analysis software. FBP reconstruction is still widely used because of historic reasons and the advantage of being fast and computationally non-expensive. Due to increasing performance of computers and advances in processing efficiency, iterative methods are becoming common practice in the clinical environment [14]. Table 2.2 gives reconstruction parameters for OSEM as recommended by the manufacturer (Siemens Healthcare). These pa-

	Cardiac Perfusion [15, 13]	**Bone Imaging [73, 14]**	**Tumor Imaging [74, 14]**	**Brain Perfusion [75]**
Radiopharmaceutical	Tc-99m-MIBI	Tc-99m-Phosphonate	In-111-Octreotide	Tc-99m-ECD
Administered activity (baseline)	1st: 250-350 MBq 2nd: 750-1050 MBq	740-1110 MBq	222 MBq	555-1110 MBq
Acquisition				
Collimator	LEHR[1], LEAP[2]	LEUHR[3], LEHR	ME[4]	LEUHR,LEHR
Energy Window Width	15%	15%*	15%*	15%*
Detector Configuration	90°	180°	180°	180°
Rotation Range	90°	180°	180°	180°
Angular Coverage	180°	360°	360°	360°
Matrix Size	64×64, (128×128)	128×128	128×128	$\geq 128 \times 128$
Pixel Size	6.6mm, (3.3mm*)	4.8mm*	4.8mm*	3.3-4.8mm
No. of projections	64	60-120	120	$\geq$120
Angular Sampling	2.8°	3-6°	3°	$\leq$3°
Time per view	20-30s	10-40s	20-30s	30s
Total Acquisition Time	15-25min	<30-45min	20-30min	30min
Total Counts	($> 6 \times 10^6$)	($> 6 \times 10^6$)	($> 6 \times 10^6$)	$> 5 \times 10^6$
Reconstruction				
FBP				
Filter Type	Butterworth, Hamming			
Cutoff	0.3-0.7[5]			
MLEM/OSEM				
Number of Iterations	8*			
Number of Subsets	4*			
Post-smoothing	8.4mm*			

Table 2.2: SPECT imaging parameter settings for different applications recommended by the European Association of Nuclear Medicine (EANM) and the Society of Nuclear Medicine (SNM). Asterisk indicates manufacturer's recommendations.

[1]Low energy high resolution
[2]Low energy all purpose
[3]Low energy ultra high resolution
[4]Medium energy
[5]depends on counting statistics and empirically established values

rameters are a general baseline and may vary significantly depending on the imaging task and the count statistics of the underlying projection data set. The effects of OSEM reconstruction parameters on the image quality will be discussed in detail in Chapter 5.

Optimal SPECT image quality is achieved by tuning of acquisition and reconstruction parameters with respect to the conducted application. In addition, gamma camera quality control and assurance is a major factor which contributes to the final image and is therefore stressed as a separate topic in many procedural guidelines. Quality control of nuclear medicine instrumentation involves the performance of the gamma camera in planar and single- and multi-detector SPECT mode. Table 2.3 gives an overview of the key quality control tests according to recommendations of the EANM [76] and the National Electrical Manufacturers Association (NEMA)

Test	Purpose	Frequency
General Gamma Camera Tests		
Energy window setting (peaking)	To check and center the energy window	daily
Background count rate	Detection of radioactive contamination and accounting for electronic noise	daily
Intrinsic/extrinsic uniformity and sensitivity	Monitoring of trends in uniformity and sensitivity	weekly
Spatial resolution and linearity	Distortion detection of spatial resolution and linearity	Six-monthly
SPECT		
Center of Rotation (COR) calibration	To check and calibrate alignment of mechanical and electronic CORs	monthly
Multi-head registration (MHR) calibration	Alignment of multiple heads for multi-head systems	monthly
Tomographic spatial resolution and contrast	Check uniformity and contrast resolution	Six-monthly

Table 2.3: Quality control tests for clinical gamma camera systems recommended by the European Association of Nuclear Medicine and National Electrical Manufacturers Association.

[77, 78]. Missing or improper system calibrations can lead to severe artifacts in the resulting images. Examples will be shown in Chapter 3.

2.4 Absolute Quantification in SPECT

Quantification in SPECT aims to depict radio-tracer distributions in absolute terms based on the acquired images. The ultimate goal is to provide reconstructed images in which each voxel represents the absolute activity concentration in the corresponding region in the patient. Absolute quantification has wide applications in many areas in nuclear medicine including patient-specific dosimetry for radiotherapy treatment planning and monitoring [79, 80, 81] and improvements in clinical diagnosis e.g. tumor classification or the detection of balanced triple vessel disease in cardiac imaging [82, 83]. As discussed earlier, various image degrading factors affect SPECT image quality. Tsui et al. [18] summarized the factors which affect the quantitative accuracy of SPECT images by adopting three main categories. These factors are outlined in Table 2.4. Active research is conducted to develop and improve techniques for the correction of these effects and to evaluate the accuracy of quantitative image reconstruction techniques. With the introduction of iterative reconstruction including the modeling of physical effects, the quantitative accuracy of SPECT images has

Category		Factor
Patient	Anatomic	Body size, anatomic structure
	Temporal	Biokinetics, motion
Physical		Attenuation, scatter
Technical	Instrumentation	Detector response, sensitivity, dead time, energy resolution, uniformity, linearity, system alignment
	Acquisition	Number of projections, time per view, radius of rotation, orbital shape
	Reconstruction	Reconstruction algorithm, compensation methods, image processing techniques

Table 2.4: Factors which affect absolute quantification in SPECT according to Tsui et al. [18]

increased [16, 18, 19]. Still, absolute quantification has not yet entered the clinical arena. In the following, current efforts for improving quantitative accuracy are briefly reviewed and failure of this prior art is discussed.

2.4.1 State of the Art

The improvement of correction techniques for SPECT quantification of different nuclear medicine isotopes is subject of active research [84, 85, 86, 87]. Various investigators have proposed quantitative image reconstruction techniques and evaluated their accuracy based on numerical and physical phantom studies.
Shcherbinin et al. [88, 89], for instance report between 3 - 5% absolute errors for total activity estimation in a torso phantom for the isotopes Tc-99m, I-123, I-131, and In-111 using CT based attenuation correction, detector response, scatter and septal penetration correction. Other studies e.g. by Du et al. for I-123 [87] and Vandervoort et al. [84] for Tc-99m show 2% accuracy in regions of a brain phantom and 4% in a cardiac chamber using their versions of correction for attenuation, scatter, detector response, and partial volume. The correction techniques for scatter and septal penetration employed in these studies are based on computational expensive methods such as Monte-Carlo simulations or analytical photon distribution and seem to perform well in phantoms also for high- and multi-energy isotopes.
He et al. [90, 80] test their quantitative reconstruction method which includes corrections for attenuation, scatter, detector response, septal penetration, and partial volume on physical and numerical phantoms using In-111. They use a population of numerical phantoms with realistic variations in anatomy and uptake and evaluated the absolute quantitative accuracy for key organs affected in radiotherapy. They re-

port an average accuracy within 5.5% in numerical and 6.5% in physical phantoms.
Koral et al. [91, 92, 93] evaluate activity quantification of I-131 in spheres which are placed in a cylindrical and an anthropomorphic torso phantom. They use high energy (HE) and ultra high energy (UHE) collimators and OSEM with attenuation correction, TEW based scatter estimation, and collimator specific point response functions. They report total activity estimation errors between 4.3% - 23.8% depending on sphere size and collimator type.
Da Silva et al. [82, 83] present a quantitative method using CT-based attenuation and partial volume correction but no scatter correction in cardiac Tc-99m SPECT studies. They report a quantitative accuracy within 4-7% in phantoms and 10% in-vivo in the porcine myocardium.
In vivo quantification in humans is e.g. presented by Willowson et al. [86]. They study Tc99m-MAA lung perfusion in 12 patients and calculate the total lung uptake in large, minimally varying volumes reporting an average accuracy of -1% (range: -7% to +4%).

2.4.2 Prior Art Failure

In the studies mentioned above little or no comment is made on the non-stationary behavior of OSEM in terms of quantification and the dependency of quantification errors on imaging parameters and instrumentation.
SPECT reconstructed spatial resolution is highly nonuniform when using maximum likelihood reconstruction without corrections for depth-dependent blur [94]. Still, with those corrections built in, resolution can only be fully recovered when iterating until convergence [95, 96]. This would lead to overly noisy and difficult to interpret images when applied to clinical data. Therefore, a lower number of iterations in combination with regularization in the form of post-smoothing is usually used in clinical practice [15]. The effects of different reconstruction parameters and instrumentation on emission recovery need to be taken into account to establish quantification baselines.
Moreover, previous work focuses on the accuracy of quantitative methods but not on the precision of the measurements. Precision is defined as the degree to which different measurements give the same result. Accuracy is the degree to which the estimation of a quantity is close to the true value. In clinical as well as research environments, imprecision due to measurement instrumentation (e.g. dose calibrator, pipette, etc.), measuring procedures (e.g. drawing of VOIs), and statistics (e.g. Poisson distributed counts) is unavoidable and should be taken into account for quantification in SPECT.
In Chapter 5 we will present a calibration method for quantitative SPECT which can be applied to clinical SPECT/CT systems. We investigate the effects of different imaging parameters by also taking into account the imprecisions caused by measurement instrumentation and procedures.

2.5 Dynamic Imaging in Nuclear Medicine

Dynamic studies are used to determine the kinetics of the radiopharmaceutical in the human body. Typical dynamic studies in nuclear medicine are for example: Renal function scintigraphy (Tc-99-MAG3, [97, 98]), gastric emptying (Tc-99-DTPA, [99]), or blood flow imaging during a three-phase bone scintigraphy (Tc-99m diphosphonate, [73]). The common method for dynamic data acquisition is a planar study. A sequence of planar images is acquired and the counts in a certain 2D region of interest (ROI) are obtained as a function of time. The relation between counts and time describes a time-activity curve (TAC). Figure 2.10 shows example images from a MAG3 renal dynamic scintigraphy during different phases. In the first 40-60 seconds, the radio-tracer resides predominantly in the blood pool (perfusion phase). In the time frame from 1-4 minutes the tracer accumulates in the kidneys (secretion) and beyond 4 minutes it is washed out into the bladder (excretion). The goal of dynamic imaging in the case of a renal study is to evaluate the kidney function and compare left and right kidney performance. ROIs are drawn around the target organs and relative quantification is performed based on measured ROI counts over time. Figure 2.10 shows example ROIs and the resulting time activity curves for the dynamic image sequence above it.
A disadvantage of planar data acquisitions is the superposition of counts from multiple organs which may result in erroneous count values within the region of interests. In addition, planar imaging does not provide quantitative results, since accurate corrections for physical effects are difficult to achieve. Thus, SPECT techniques have been investigated for use in dynamic studies.

2.5.1 Dynamic SPECT - State of the Art

In the past two decades, a variety of different approaches for dynamic SPECT imaging has been proposed. In general, there are two different ways to obtain dynamic parameters when using a rotating SPECT system. The most straightforward approach has often been referred to as image based or conventional frame by frame method in literature [100, 101, 102]. The method uses a sequence of fast camera rotations each one generating a full projection data set which is reconstructed using conventional 3D reconstruction methods. A single reconstructed image represents the spatial activity distribution at one point in time. The activity distribution is therefore assumed to be constant during the collection of one full projection data set. The sequence of reconstructed images is then used to derive time activity curves or to fit kinetic parameters. This approach usually requires multi-headed SPECT systems, in order to acquire sufficient counts in a small amount of time for a reasonable temporal resolution. Dual and triple head imaging systems were used in the past e.g by Nakajima et al. [101], Celler et al. [100], Luyt and Wells [103], or Narayanan et al. [102].
Another set of methods are direct approaches which use the whole set of projection data simultaneously and fit kinetic parameters or find a series of dynamic images. Often, a single camera rotation is used to generate the projection data set. Either dynamic parameters are extracted directly from the projections or time activity curves are generated from reconstructed spatiotemporal images. Various tools have

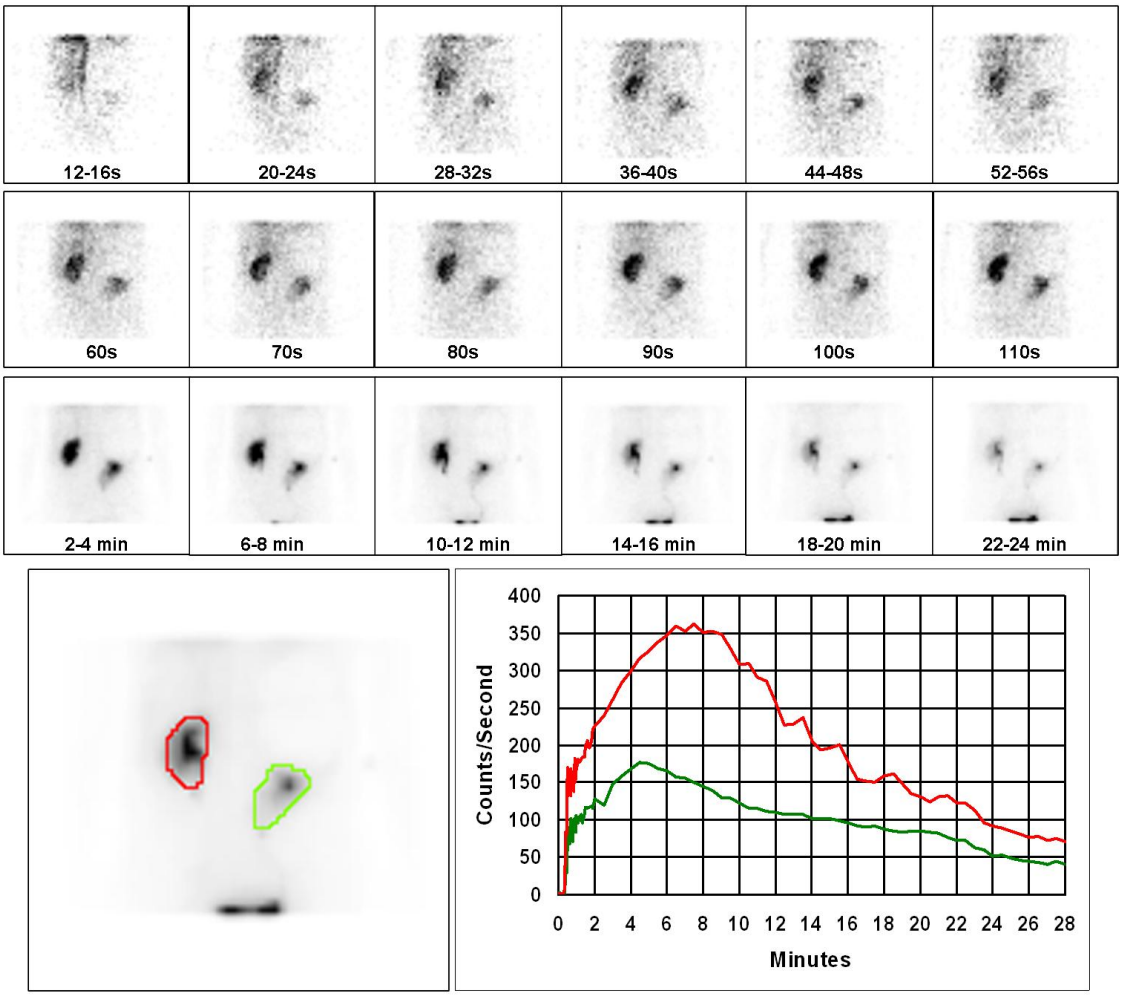

Figure 2.10: Example images, ROI analysis, and resulting time activity curves of a MAG3 renal dynamic scintigraphy.

been used to find solutions for these estimation problems including MLEM methods [104, 105, 106] and non-linear (NLS) [107, 108, 109] and linear least square minimization (LLS) [108, 110, 111]. Usually, some assumptions about the temporal behavior of the activity are made e.g. by using a single or dual-exponential model [108], a set of basis functions [112], factor models [113, 114], or simple inequality assumptions [110, 111].
Farncombe et al. and Celler et al. [110, 108, 111], for example, presented a dynamic SPECT method referred to as 'dSPECT' which uses a single camera rotation of a slowly rotating gantry. They used a constrained linear least-squares (CLS) problem of the form:

$$f(x) = \left\{ \sum_{i,t} \sigma_{it}^{-2} \left(\sum_{j} a_{ijt} x_{jt} - g_{it} \right)^2 \right\} \tag{2.42}$$

subject to

$$x_{j1} \geq x_{j2} \geq \cdots \geq x_{jn} \geq 0 \tag{2.43}$$

or

$$0 \leq x_{j1} \leq x_{j2} \leq \cdots \leq x_{jn} \tag{2.44}$$

or

$$0 \leq x_{j1} \leq \cdots \leq x_{jp} \geq \cdots \geq x_{jn} \geq 0 \ , \tag{2.45}$$

where x_{jt} is the activity in the jth voxel at time t, σ_{it}^{-2} is a weighting factor determined from the variance in projection element g_{it}, and a_{ijt} is the system matrix element. With this technique a series of images is reconstructed, each image representing the activity distribution at the time when each projection is acquired. The method yielded 10% accuracy of the physiological half live in simulations and 20% in dynamic cardiac phantom experiments.
Farncombe et al. also proposed a dynamic version of the expectation maximization algorithm [106, 105]) based on the static MLEM algorithm (Equation (2.37)) by introducing an additional dimension (time) and using the same temporal inequality constraints as for the CLS method (Equation (2.43) - (2.45)). The dynamic MLEM method produced comparable accuracy but with improvements in reconstruction times compared to CLS by a factor of 2-3.
The dSPECT method was applied in-vivo in renal studies [111] and in imaging of hepatic hemangiomas [103]. In the hepatic studies, the dSPECT method demonstrated comparable accuracy to the conventional dynamic SPECT approach for the estimation of TACs.
Reutter et al. [112, 115, 116, 117], presented a direct least-square estimation method using temporal B-splines which obtains time activity curves and kinetic parameters directly from projections. The method was tested in simulations with a dynamic Mathematical Cardiac Torso (MCAT) phantom. Kinetic parameters for cardiac uptake and washout could be determined with an accuracy of 0.3% in the myocardium and 5% and 16% in septal and lateral defects.
The method was extended later on, to derive a spatiotemporal image sequence and applied to cardiac patient studies [118, 119].
In general, spatiotemporal reconstruction techniques have a high computational burden [118]. They have not yet proven their superiority in terms of TAC estimation

accuracy compared to image based methods which use fast acquisitions and conventional reconstruction. Image based methods have been clinically used e.g. for the estimation of dynamic blood pool and liver uptake [120, 121, 122] or for the quantification of myocardial blood flow [123]. The advantage of these methods is the availability in clinical environments and the relatively fast reconstruction times. Disadvantages are low counting statistics and high noise in the images due to the short acquisition times required. Recently, Iida et al. [123] presented a study where they quantified the myocardial blood flow with Tl-201 in-vivo in canine using a fast rotating dual-headed commercial gamma camera and OSEM reconstruction with corrections for attenuation and scatter. They calculated kinetic parameters and compared the results with blood samples and the true values of sacrificed myocardial tissue. They reported good correlation (R=0.93) between the measured and true kinetic parameters.
In Chapter 5 we will establish a baseline for this image based methods by employing a dual-headed SPECT system and assessing the quantitative accuracy of TAC estimation using simulations and physical phantom experiments.

2.6 Summary

In this chapter we introduced the principles of SPECT image formation. We covered SPECT imaging instrumentation, projection characteristics, and tomographic image reconstruction. We explained SPECT inherent physical effects and showed approaches for their correction within iterative image reconstruction.
Furthermore, we gave an overview of state of the art hybrid SPECT/CT clinical applications and imaging protocols. In this context we provided detailed information about typical clinical acquisition and reconstruction protocols for selected applications such as e.g. cardiac perfusion imaging.
Finally, we summarized the state of the art of quantitative and dynamic SPECT imaging and discussed their maturity for clinical routine usage.
Based on the fundamentals provided in this chapter we optimize imaging protocols in Chapter 3 and 4 by focusing on the cardiac application and develop a method for clinical quantitative imaging in Chapter 5.

Chapter 3

Development of Image Analysis Tools

To ensure constant and optimal diagnostic performance in emission tomography, quality assurance within the entire image formation chain is essential. This includes thorough instrumentation quality control according to National Electrical Manufacturers Association (NEMA) specifications [77, 78] or other recommendations [76, 124] (Table 2.3) as well as optimization and standardization of imaging protocols as e.g. proposed by the American Society of Nuclear Cardiology (ASNC) [125] or European Association of Nuclear Medicine (EANM) [15]. Phantom studies are often used to track down system problems, to optimize imaging parameters and instrumentation, or to establish image quality baselines. This is either done with numerical models and simulations [126, 127, 128, 129, 130] or with physical measurements of phantoms [131, 132, 133, 134]. By performing actual measurements as opposed to simulations of an imaging system, uncertainties in system modeling are avoided. Therefore, we use actual measurements to evaluate clinical imaging systems.
In the following, we present a suite of tools for the manipulation, reconstruction, and evaluation of static 3D and gated 3D (3D+t) SPECT data. We focus on the semi-quantitative evaluation of image features in cardiac static and dynamic phantom data. The presented tools are then used in Chapter 4 to optimize clinical cardiac imaging protocols.

3.1 SPECT Data Manipulation and Reconstruction

Measurements with SPECT imaging systems using physical phantoms are time consuming especially if the entirety or a subset of the imaging parameter space is to be explored. Thus, only a coarse sampling of the parameter space is usually possible. To allow for maximal flexibility in terms of acquisition and reconstruction parameter variation, we use a self-developed tool which allows retrospective manipulation of projection data sets and batch mode reconstruction with varying parameter settings. Figure 3.1 shows a flow chart of this tool, which can be embedded as a graphical user interface in the routine clinical workflow via broker interface to the commercial software package. The tool allows DICOM compatible handling of raw and reconstructed SPECT data including image reading and writing.
Projection data manipulation includes angular resampling, count reduction, scan range extraction, and matrix size reformatting. For count reduction, Poisson charac-

teristics are maintained using binomial subsampling [135].
The binomial distribution gives the discrete probability distribution of obtaining exactly c successes out of N Bernoulli trials where the result of each Bernoulli trial is true with probability p. The Poisson distribution (Equation (2.27)) with the parameter $\lambda = Np$ can be derived as a limiting case of the binomial distribution as $N \to \infty$ and $p \to 0$.
In binomial subsampling, a new count c is obtained from a pixel value N, using a subsampling fraction p. Applied to a Poisson deviate (a count in a pixel), the outcome is a new Poisson deviate whose mean is reduced to a fraction p. This way, a new subsampled Poisson distribution is generated. Note that in practice multiple subsampled realizations of the same initial Poisson deviate are not strictly statistically independent, since in SPECT N is a finite number and $p > 0$.
Manipulated or raw projection data are reconstructed using OSEM with 3D collimator and detector response compensation (OSEM-3D) with optional attenuation and scatter correction. Batch mode is possible for reconstruction parameter variation. The reconstructed and manipulated data are written to DICOM files for export or further processing within the imaging system's commercial software package.
This processing tool will be used extensively to generate the image data which is used for validation of evaluation tools and optimization of clinical protocols in Chapter 3 and 4. It can be applied to both phantom and patient data. For instance, this allows the clinician to test non-standard protocols on retrospective data prior to applying such a modified protocol prospectively to patients.

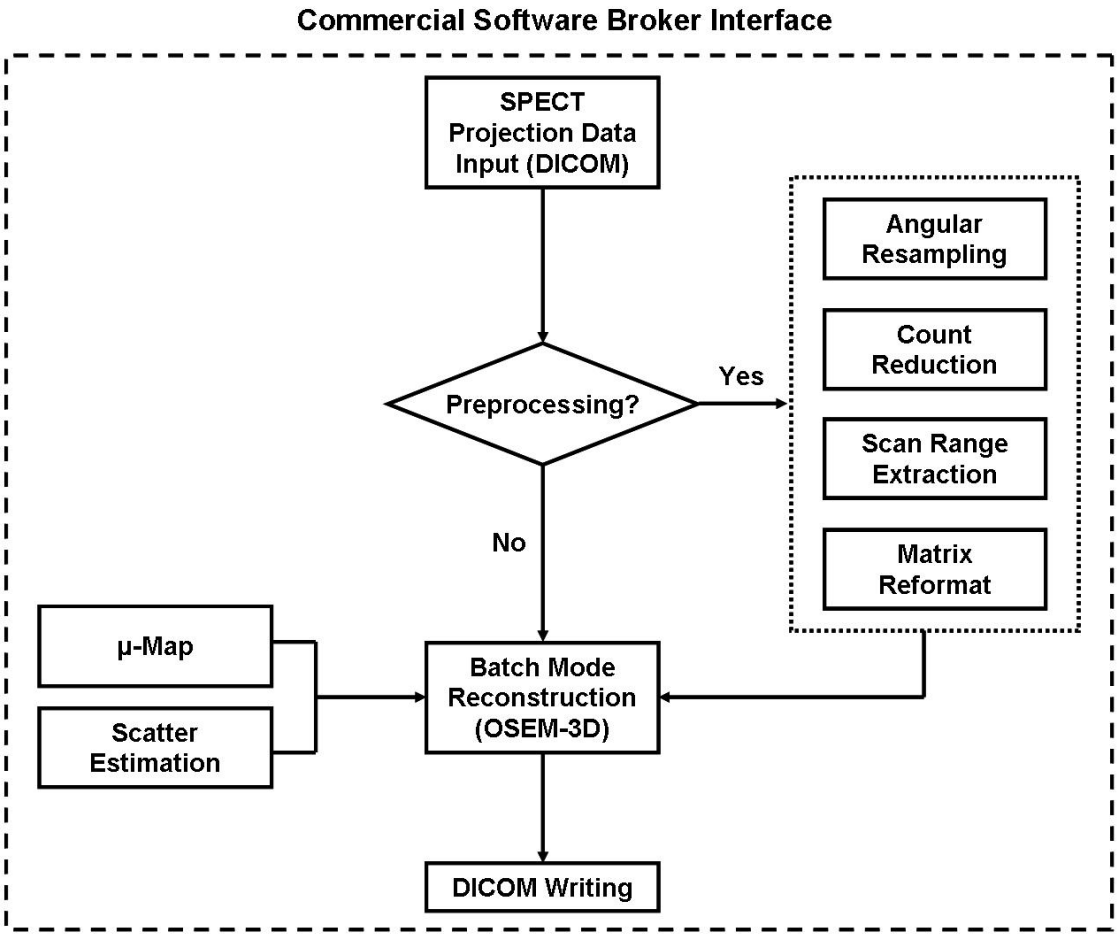

Figure 3.1: Flow chart for projection data manipulation and reconstruction tool.

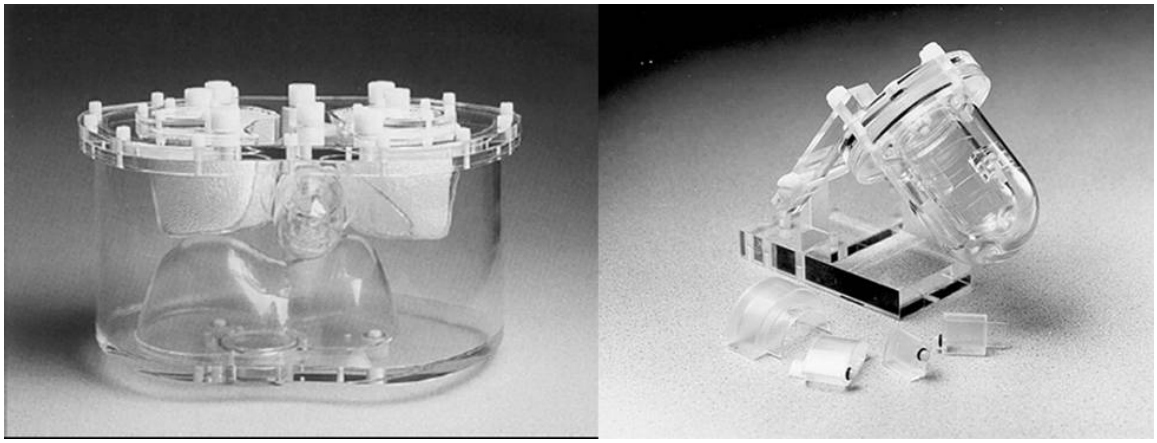

Figure 3.2: Anthropomorphic Torso Phantom (left) with Cardiac Insert^{TM} (right) manufactured by Data Spectrum Corporation.

3.2 3D Cardiac Image Analysis

A commercially available phantom which simulates the key imaging physics of a human torso is the Anthropomorphic Torso Phantom^{TM} manufactured by Data Spectrum (Hillsborough, NC). In this section we develop a method for semi-automatic quantitative image assessment of the cardiac insert inside this anthropomorphic phantom acquired by a SPECT or SPECT/CT system.
Methods for semi-quantification of clinical gated and ungated myocardial perfusion SPECT images have been developed before e.g. by Garcia et al. [136, 137, 138, 139] and Germano et al. [140, 141, 142] including techniques for sampling of the myocardium and extraction of perfusion information, wall characteristics, and motion. These methods are designated for the use in clinical routine. They emphasize the processing of perfusion information and facilitate clinical diagnosis by delivering automatic and consistent results on easy to interpret displays.
We adopt some of the techniques and modify them for use with the cardiac phantom. Additional image features such as reconstructed image uniformity, wall thickness, and regional perfusion ratios are extracted from the phantom images. We show that these features can be used to demonstrate the effects of parameter variation in the SPECT image formation chain including quality control failures and different acquisition and reconstruction settings. In general, this phantom assessment tool can be used for the purposes of SPECT system specification and testing, trouble shooting, assessment of novel technology, and optimization of acquisition and/or reconstruction protocols for the cardiac application.

3.2.1 Target Phantom

The phantom used is the Anthropomorphic Torso Phantom (Data Spectrum, Hillsborough, NC), an acrylic glass cylinder with cardiac, liver, lung, and spine components (see Figure 3.2 left). It simulates the key imaging physics by also providing a simple analytically tractable geometry of the cardiac insert. The cardiac insert (Figure 3.2

right) consists of two chambers, simulating the left ventricular blood pool and the myocardial wall with a true wall thickness of 10 mm. In order to mimic abnormalities in terms of perfusion values, various lesions both fillable and solid, with different radial and angular extents, can be mounted in the myocardial wall. This phantom is well known and widely used in nuclear medicine for cardiac specific system tests. This includes both investigating the performance of novel technologies as well as assuring cardiac specific image quality in clinical settings.

3.2.2 Generation of Myocardial Wall Response Function

The developed cardiac analysis tool processes reconstructed, reoriented, or transversal cardiac SPECT data and calculates characteristic metrics like perfusion, wall full width at half maximum (FWHM), blood pool and lesion contrast, and attenuation effects. The image volume is registered to the known geometric model of the cardiac insert to obtain reproducible and reliable results. The volume is automatically aligned by determining a rigid body transformation which minimizes the chi-squared deviation of the calculated emission center from the geometric centerline of the physical cardiac chamber. This method shows high reproducibility with standard deviations lower than 0.05% for translation and lower than 2.8% for rotation, when using the same physical phantom with variations in imaging and reconstruction protocols.
After the alignment of the volume, the myocardial wall emission function is determined by generation of emission profiles. This is done by a three-dimensional hybrid sampling of the volume as proposed by [136, 141, 142] to extract the three-dimensional myocardial count distribution.
A series of emission profiles is interpolated from the physical axis of the chamber through the myocardial wall to a distance which is twice the radius of the physical chamber. The emission profiles are extended radially, in a cylindrical geometry through the base of the volume and in a spherical geometry in the hemispherical apex of the chamber, in order to ensure a radial sampling perpendicular to the myocardial wall [136, 141, 142].
The complete set of emission profiles E may be represented as

$$E(r,\theta,\xi) \qquad \xi = \begin{cases} z & \forall\, z \leq z_0 \\ \varphi & \forall\, z > z_0 \end{cases} , \tag{3.1}$$

where r is the radius extending perpendicularly from the chamber axis, θ is the polar angle about the axis, and ξ combines two parameters used in the two different coordinate systems: z denotes the distance along the long axis in cylindrical coordinates, and φ is the spherical angle in the spherical coordinate system describing the apex. The definition of ξ is given by z_0 which is a known parameter derived from the phantom geometry. Figure 3.3 illustrates the sampling principle and the use of the two different coordinate systems on a 2D long axis slice.

The entire generating process of $E(r,\theta,\xi)$ is shown in Figure 3.4. The volume is sampled as shown for HLA, VLA, and SA, and the generated profiles are 'stacked' in θ, z, and φ, which leads to a sinogram like profile display (Figure 3.4 right).
Here, r runs horizontally across the image, θ cycles repeatedly through 2π as one moves vertically along the image, and z and φ increase step-wise from the base to

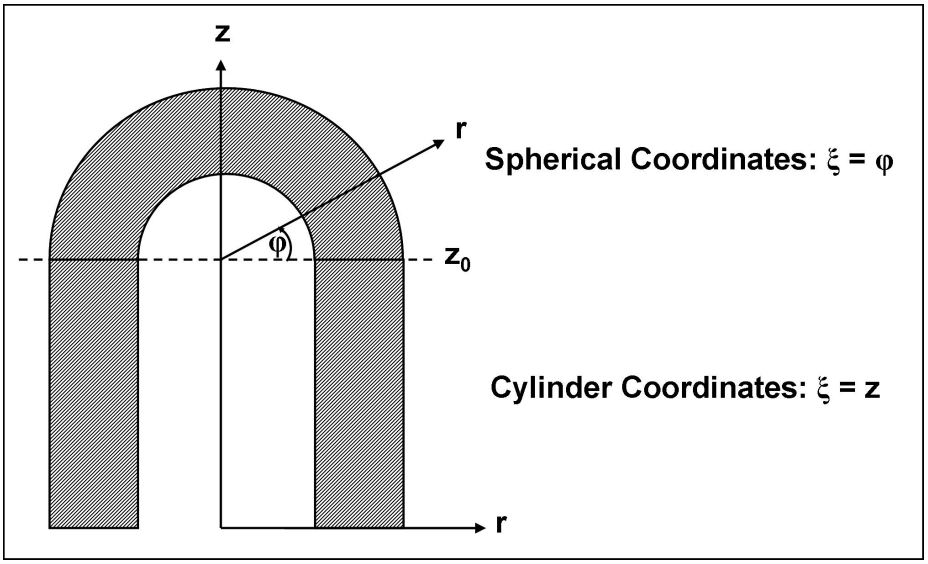

Figure 3.3: Definition of sampling variables and coordinate systems matched to the geometry of the phantom.

the apex as one moves vertically from the bottom to the top of the image. For a perfectly uniform and aligned myocardium, the image would appear as a simple uniform vertical strip.

Once $E(r, \theta, \xi)$ is determined, a set of operations is performed which characterize properties of the emission profile at each θ and ξ. Specific quantitative values are defined as properties of each profile.

Figure 3.5 left shows a single radial profile through the myocardial wall for an arbitrary θ and ξ. For the quantitative analysis, the center position R_0 of the wall is estimated as the maximum of the profile curve similar to the determination process of a circumferential profile used to generate perfusion polar maps [136, 137, 138, 139]. R_1 and R_2 are defined as:

$$E(R_{1,2}, \theta, \xi) = \frac{1}{2} E(R_0, \theta, \xi) \quad \forall\, R_1 < R_2 \tag{3.2}$$

such that $R_2 - R_1$ results in the FWHM of the profile curve which is defined as the wall thickness $T(\theta, \xi)$.

The integral perfusion $P(\theta, \xi)$ for each profile is defined as the area under the profile curve bounded by R_1 and R_2:

$$P(\theta, \xi) = \sum_{r=R_1}^{R_2} E(r_i, \theta, \xi) \ , \tag{3.3}$$

where r_i is the pixel position along the profile between R_1 and R_2. This definition of the perfusion uses a 'whole myocardium sampling' as proposed by Germano et al. [143].

The wall distortion is a measure for the deviation of the wall position from the mean of the positions in the mid regions z_{Mid}.

$$D(\theta, \xi) = \left| R_0(\theta, \xi) - \overline{R}_0(\theta, z_{Mid}) \right| \ . \tag{3.4}$$

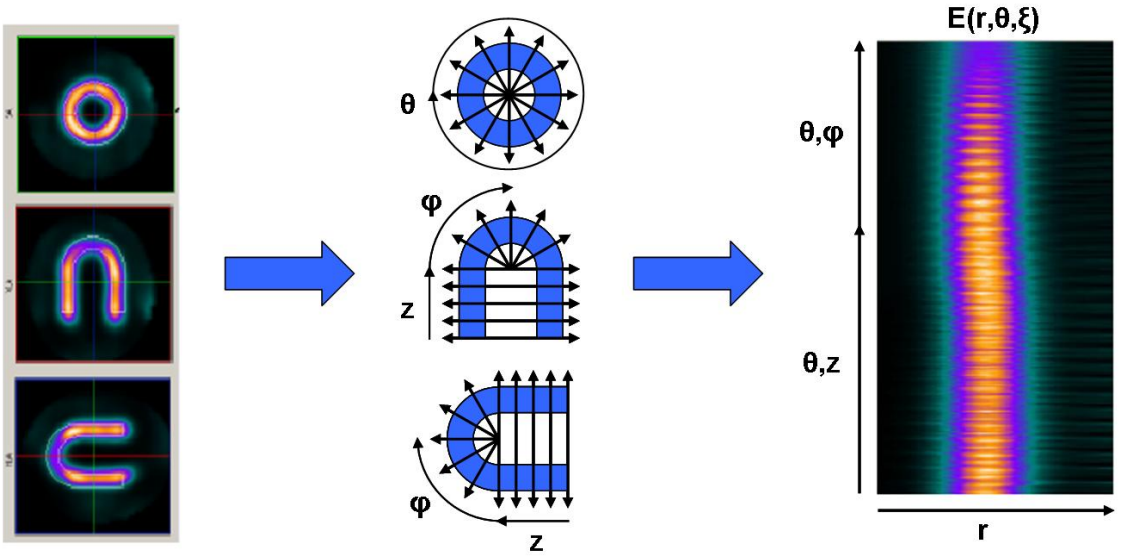

Figure 3.4: Generation of the myocardial wall response function. The reconstructed volume is registered to the geometry of the cardiac insert (left). Radial profiles are generated (center) and stacked (right).

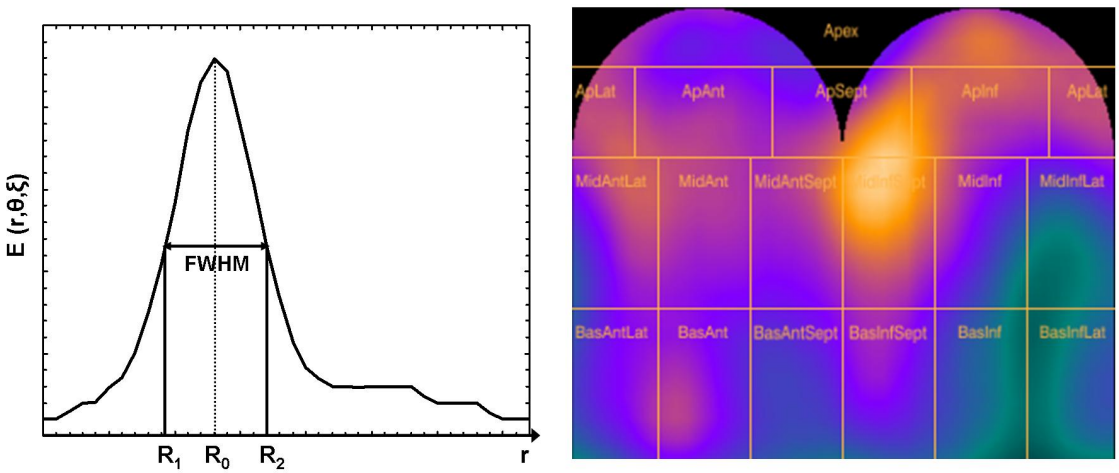

Figure 3.5: Left: Response function $E(r, \theta, \xi)$ of a single radial profile. Right: 2D 'bullet map' showing the quantitative values for the integral perfusion (Equation (3.3)). Optionally the map is superimposed either with the region border lines of the conventional 17 segment model or the o'clock lines (not shown here). In addition, the statistics for each region can be displayed.

The nonsymmetry of the wall based on the area under the profile curve gives an impression of unbalanced wall distortions:

$$S(\theta,\xi) = \frac{\sum_{r=R_1}^{R_0} E(r_i,\theta,\xi) - \sum_{r=R_0}^{R_2} E(r_i,\theta,\xi)}{\sum_{r=R_1}^{R_0} E(r_i,\theta,\xi) + \sum_{r=R_0}^{R_2} E(r_i,\theta,\xi)} \ . \tag{3.5}$$

In order to estimate the 'spill over' from the wall into the blood pool, the difference between the profile and a fitted Gaussian is calculated. The blood pool intensity is defined as the fraction of the area under the profile in the range from the geometric center of the blood pool chamber to the center of the myocardial wall, which is different from a Gaussian with $\sigma = FWHM/\sqrt{8\ln 2}$:

$$I_{BP}(\theta,\xi) = \frac{\sum_{r=C_{BP}}^{R_0} E(r_i,\theta,\xi) - \frac{1}{\sigma\sqrt{2\pi}} e^{(r_i-R_0)^2/2\sigma^2}}{\sum_{r=R_1}^{R_2} E(r_i,\theta,\xi)} \ , \tag{3.6}$$

where C_{BP} is the geometric center of the blood pool.
The analysis of the entire set of profiles yields simple functions of (θ,ξ) which can be displayed visually in 2D maps. For each defined quantitative value set ($T(\theta,\xi)$, $P(\theta,\xi)$, $D(\theta,\xi)$, $S(\theta,\xi)$, $I_{BP}(\theta,\xi)$) such a 'bullet map' is generated. The bullet map visualization was chosen instead of the more conventional bullseye to minimize distortions and to preserve the cylindrical geometry in the base and mid regions. Figure 3.5 right shows the property map for the quantitative values of the integral perfusion (Equation (3.3)). Region border lines according to the conventional 17 segment model [144] are superimposed. The property maps are segmented vertically into basal, mid, and apical sections (ξ) and horizontally (θ) in 6 sections for base and mid, respectively and 5 sections for the apex.
Tractable parametric analysis of myocardial image quality as a function of acquisition or reconstruction parameters requires further distillation of the property maps into a small number of global image quality metrics with a transparent relationship to visual assessment of image quality. For this purpose a set of global metrics was defined which is given in Table 3.1. Here $\overline{P}$ denotes the mean perfusion of the mid and base regions ($\xi = z$). $\theta_{(...)}$ denotes a range in the short axis e.g. $\theta_{5o'clock}$ defines the short axis region between 4 and 6 o'clock, where usually a depression of image counts occurs in uncorrected images due to attenuation. The defined global metrics do not make any claim of completeness. Yet, we believe that these are the most relevant metrics to describe image features which also are visually comprehensible. Additional metrics can easily be derived from the Wall Response Function $E(r,\theta,\xi)$.

3.2.3 Tool Evaluation

Phantom Setup Heart, liver, and background of the phantom (Figure 3.2) are loaded with Tc-99m. The activity concentration ratio is adjusted according to Table

Nonuniformity	$\sigma(P(\theta,z))/\overline{P}$
Nonsymmetry	$\overline{S}(\theta,\xi)$
Wall Thickness	$\overline{T}(\theta,\xi)$
Blood pool Intensity	$\overline{I}_{BP}(\theta,\xi)$
Apical Thinning	$\frac{\overline{P}-min(P(\theta,\varphi))}{2\overline{P}}$
5 o'clock Artifact	$\frac{\overline{P}(\theta_{5o'clock},z)-\overline{P}}{\overline{P}}$
Inferior vs. Anterior Wall Perfusion	$\frac{\overline{P}(\theta_{Inf},z)-\overline{P}(\theta_{Ant},z)}{\overline{P}}$
Septal vs. Lateral Wall Perfusion	$\frac{\overline{P}(\theta_{Sept},z)-\overline{P}(\theta_{Lat},z)}{\overline{P}}$

Table 3.1: Definition of global metrics ($\overline{P}$ denotes the mean perfusion of the mid and base regions $\overline{P}(\theta,z)$).

	Injected Activity (MBq)	Activity Concentration (kBq/ml)	Concentration Ratio
Myocardium	74.0	673.4	14.0
Liver	444.0	384.8	8.0
Background	444.0	48.1	1.0

Table 3.2: Phantom preparation

3.2 simulating realistic uptake ratios of Tc-99m-MIBI in the human body [145]. Note that the lung inserts are filled with both Styrofoam as well as water to correctly simulate lung attenuation.

Data Acquisition The imaging system used for test data acquisition is a dual-headed SPECT-CT hybrid camera (Symbia-T6, Siemens Healthcare). Three different low-energy collimator types are used for comparison: Low Energy All Purpose (LEAP), Low Energy High Resolution (LEHR), and Low Energy Ultra High Resolution (LEUHR). The sensitivity ratio of these collimators is: LEAP:LEHR:LEUHR = 8.9:5.5:2.7 cpm/kBq and the geometric resolution at 10 cm distance is 8.3 mm, 6.4 mm, and 4.6 mm, respectively (according to manufacturer's specification).
The cardiac insert is acquired both in air, in order to investigate basic principles without image degradation caused by attenuation, as well as within the torso casing. Table 3.3 provides an overview of the acquisition parameters used for both phantom setups. The noncircular scan orbit range for the torso using the 90° detector configuration extends from 45° left posterior oblique to 45° right anterior oblique according to clinical imaging procedures [15]. High-count projections are acquired with

	Insert in Air	Insert in Torso	
Head Separation Angle	180°	90°	180°
Scan Range	360°	180°	360°
Angular Step	3°	3°	3°
Orbit	circular	non-circular	non-circular
Radius	25 mm	variable	variable
Pixel Size	4.8 mm	4.8 mm	4.8 mm
Matrix Size	128×128	128×128	128×128
Total Counts	6 million	90 million	270 million
Count Density in Myocardium	24-27 cts/pixel	44-52 cts/pixel	33-39 cts/pixel

Table 3.3: Key acquisition parameters for the cardiac phantom tests (Note: Count density is given for LEHR collimation.)

	Non-uniformity	Wall Non-symmetry	Wall Thickness	BP Contrast	5 o'clock Intensity	Inf. vs. Ant. Intensity	Sept. vs. Lat. Intensity
Mean	8.21	0.04	20.15	13.25	-11.40	-5.35	11.13
SD	0.23	0.12	0.31	0.12	1.38	0.28	1.76

Table 3.4: Reproducibility check for quantitative analysis. All values except the wall thickness (mm) are given in percent.

a 128×128 matrix size (see Table 3.3). These data sets serve as high level starting point with enough flexibility for the generation of various count levels via binomial subsampling.

The projection data of the cardiac insert in air is reconstructed with both FBP (Butterworth filter of order 5) and OSEM-3D. Multiple count levels for the torso data are created by binomial subsampling of the high count data sets [135].
To give an impression of the reproducibility of the result values delivered by the analysis tool, the phantom is repeatedly prepared four times according to Table 3.2 without defect and acquired using standard acquisition parameters according to a clinical scan [15] with 90° detector configuration, non-circular orbit, 3° angular sampling, 8 million total counts, and 128×128 matrix size. Projection data is reconstructed with OSEM-3D with scatter and CT based attenuation correction using 32 updates. The mean and standard deviation (SD) of the result values for the four acquisitions as reported by the quantitative analysis are shown in Table 3.4.

To show the transparency of the quantitative metrics defined in Table 3.1 towards visual impression, a comparison of short axis images of the torso phantom acquired in 180° detector configuration (see Table 3.3) is shown in Figure 3.6. OSEM reconstruction parameters are varied for a high (270 million total counts, top row) and low (6 million total counts, bottom row) count level, respectively. The number of OSEM updates used is 12, 30, 120, and 450 from left to right. Scatter and attenuation correc-

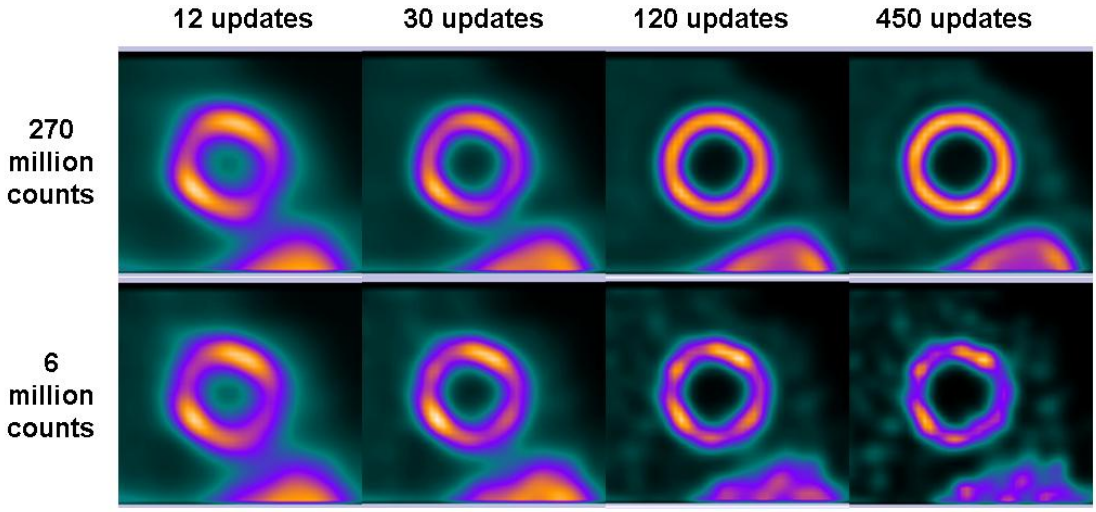

Figure 3.6: Example reconstructed short axis images of the torso phantom acquired with LEHR collimation, 180 detector configuration, 128×128 matrix size, and 3° angular sampling. The first row shows a reconstructed high count data set with 270 million total counts. The second row shows a low count data set with 6 million total counts. Scatter and attenuation correction are applied using 12, 30, 120, and 450 OSEM updates from left to right.

tion are applied. Table 3.5 gives the results as reported by the quantitative analysis. Both, metrics derived from perfusion values (uniformity and intensity ratios) as well as metrics describing the shape behave as expected for the different reconstruction parameters and count levels. In addition, these values indicate operation ranges of our experiments when consulting the 'best' and the 'worst' images.

In the following, application examples are shown for the assessment of specific steps in the image formation chain, namely: impacts of the target object itself (phantom), system calibration effects (e.g. detector misalignment), imaging parameters (e.g. collimation schemes and reconstruction parameters), and image corrections.

To demonstrate the sensitivity of the analysis tool, two differently manufactured cardiac inserts from Data Spectrum (Hillsborough, NC, USA) are compared. Figure 3.7 shows CT images of the two inserts filled with CT contrast agent and the corresponding SPECT images. In the molded insert (Figure 3.7 left) bulges of a seam can be seen in the CT image which are approximately 2 mm thick and therefore smaller than the system resolution of 7.4 mm (FWHM with LEHR collimation at 10 cm distance). According to the findings of the analysis tool a definite decrease of counts in the apex can be observed. This is illustrated by both the bullet maps (Figure 3.7 lower images) as well as the global metric for Apical Thinning. In the molded insert this value is 6.3% whereas the milled phantom (Figure 3.7 right) shows an almost perfect apex with a value of -0.3%.

Figure 3.8 shows the effects of detector misalignment in y-direction as it may occur when multi-head calibrations are absent or not performed correctly. Figure 3.8 left gives a visual impression how detector y-shift affects the image quality. Therefore the projection data are shifted artificially prior to reconstruction. Figure 3.8 shows

	270 million				6 million			
Updates	12	30	120	450	12	30	120	450
Nonuniformity (%)	11.4	7.9	4.3	4.3	11.9	9.7	9.5	14.0
Wall Nonsymmetry (%)	-0.7	-0.2	0.01	0.2	-1.5	-0.8	-0.4	-0.3
Wall Thickness (mm)	24.7	17.5	13.6	12.4	24.6	17.4	13.6	12.4
BP Intensity (%)	24.9	15.8	4.8	4.1	25.2	15.8	5.0	5.6
5 o'clock Intensity (%)	-13.0	-13.0	-5.2	-2.3	-11.2	-10.5	-4.8	-2.5
Inf. vs. Ant. Intensity (%)	-15.3	-12.7	-7.4	-5.7	-15.2	-13.9	-8.7	-3.9
Sep vs. Lat Intensity (%)	15.4	10.5	3.7	1.0	12.2	6.0	-1.5	-3.8

Table 3.5: Quantitative results for the reconstructed volumes in Figure 3.6

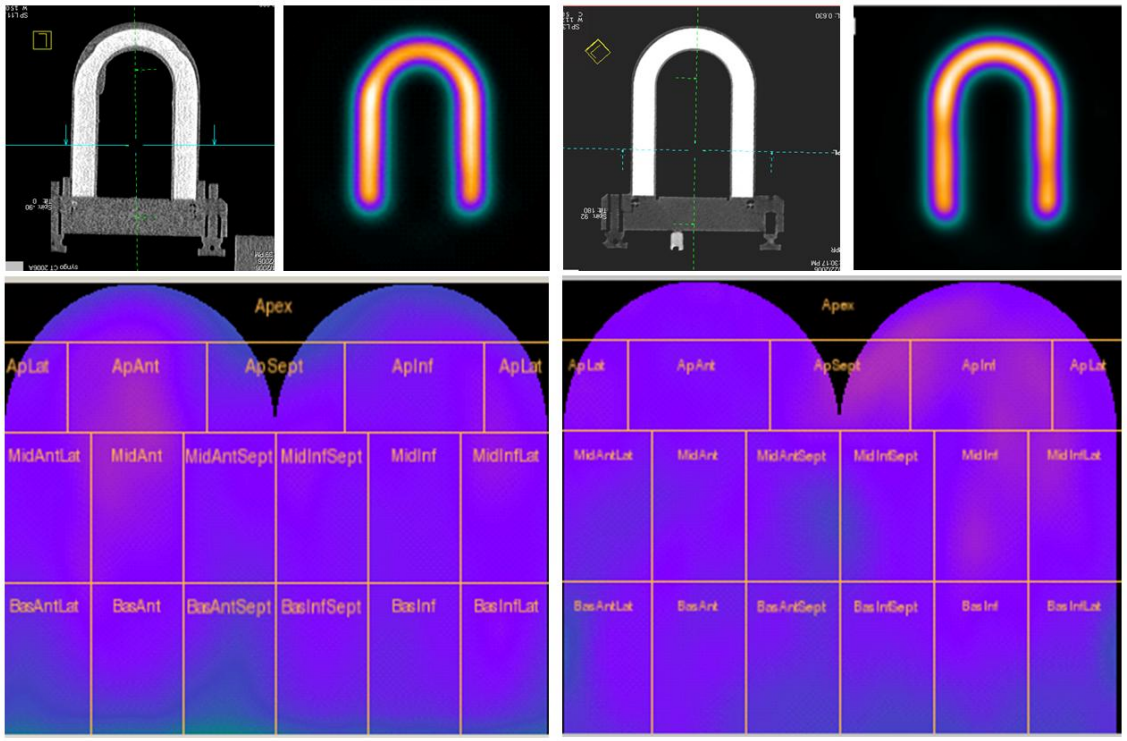

Figure 3.7: Analysis of two differently manufactured phantoms in terms of apical thinning. Left: CT image, SPECT reconstructed image, and bullet map of the molded phantom. The bullet map shows definite decrease of counts in the apex and the global metric for Apical Thinning is 6.3%. Right: Milled phantom. CT image and bullet map show an almost perfect apex. The global metric for Apical Thinning is -0.3%.

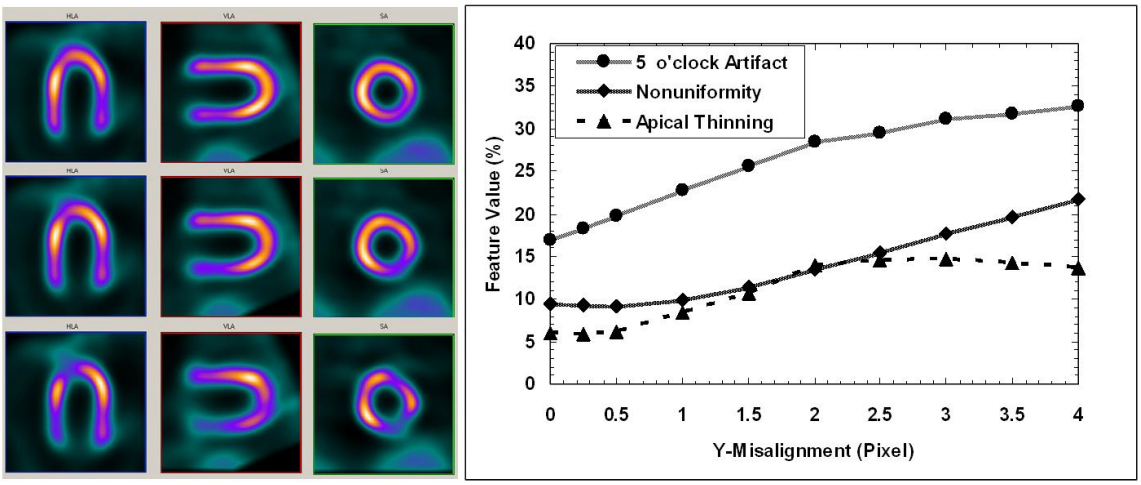

Figure 3.8: Left: Sample reconstructed slices of the male torso phantom. The projection data were modified to simulate a detector misalignment in y-direction. First row: without artificial y-shift; Second row: 1 pixel y-shift; Third row: 3 pixel y-shift; Right: Volume image features depending on the head misalignment in y-direction. The pixel size of the projection data was 3.3 mm.

selected image quality metrics for different y-shifts as reported by the analysis tool.

Results obtained by analyzing the image data of the cardiac insert in air illustrate how the defined global metric of Wall Thickness reveals principle impacts of variations in selected imaging and reconstruction parameters. Figure 3.9 gives an overview of how different collimators, as well as reconstruction methods and parameters, affect the myocardial wall FWHM. With FBP no significant improvement can be achieved beyond a filter cut-off value of 0.4. The same is true beyond 100 updates of OSEM-3D. Note that, with using about 20 OSEM updates, the FWHM is already below the value of convergence in FBP. Here the cut-off frequency for FBP is given as a multiple of the Nyquist frequency in spatial domain ($f_{Nyquist} = 0.5\,cycles/pixel$).

Figure 3.10 shows sample slices and the perfusion maps provided by the analysis tool applied to the torso phantom images. The data set in the first row shows the FBP reconstructed image. The second row shows the OSEM reconstructed and uncorrected image. The typical decrease of intensity in the inferior wall due to attenuation and scatter from the hot liver can be seen [143, 146]. This is confirmed by the perfusion maps. The third row in Figure 3.10 is the attenuation and scatter corrected image using a low dose CT generated attenuation map. The redistribution of the perfusion values is noticeable especially in the inferior regions. The global metrics which are influenced by attenuation effects for the images shown in Figure 3.10 are summarized in Table 3.6.

In summary, we can conclude that the presented quantitative phantom analysis tool demonstrates its practicability and shows proper sensitivity to reveal relevant image quality aspects caused by processes taking place within the entire image formation chain. It proves to be reliable and delivers reproducible results. This allows the use in a wide range of purposes such as system specification, assessment of novel

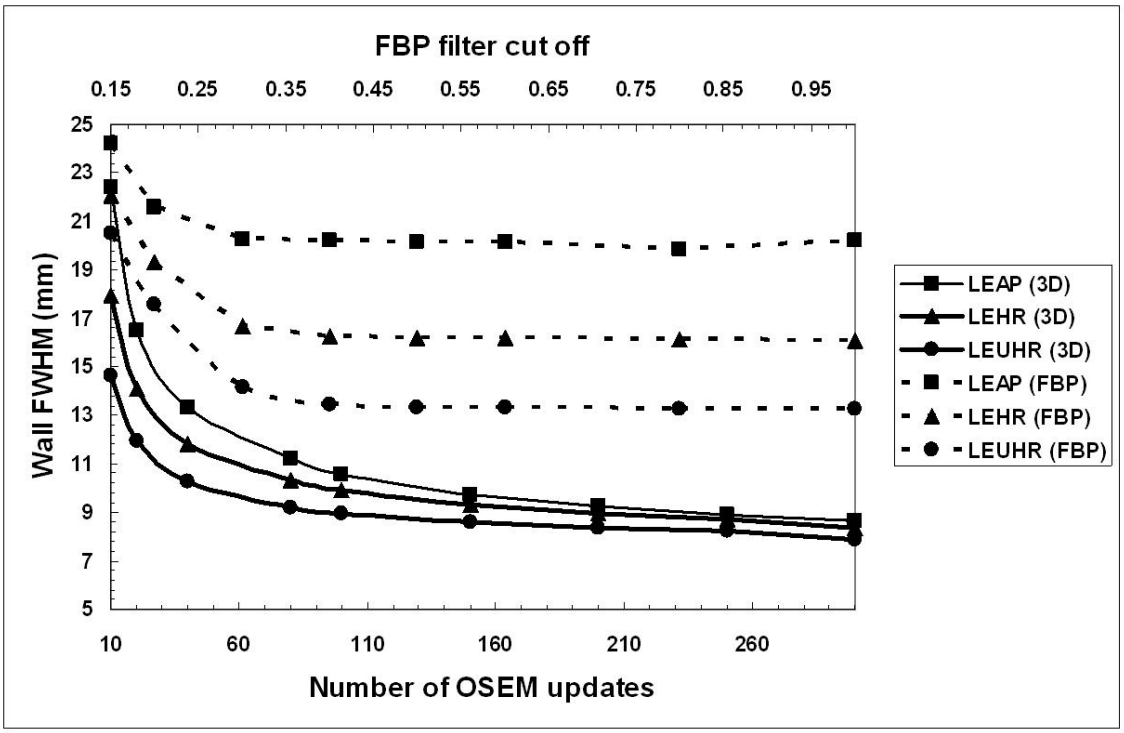

Figure 3.9: Quantitative results for the wall thickness of the Cardiac Insert in air acquired with three different collimation methods and reconstructed with OSEM-3D and FBP. Note that the filter type used for FBP was Butterworth with order 5. The FWHM of the Gaussian post-smooth in OSEM-3D was set to 2 times the pixel size, respectively.

	5 o'clock Intensity (%)	Inf. vs. Ant. Intensity (%)	Sept. vs. Lat. Intensity (%)
FBP	-18.9	-8.5	13.0
OSEM-3D uncorrected	-18.8	-18.6	16.0
OSEM-3D corrected	-6.2	-4.9	6.0

Table 3.6: Analysis results of the images shown in Figure 3.10

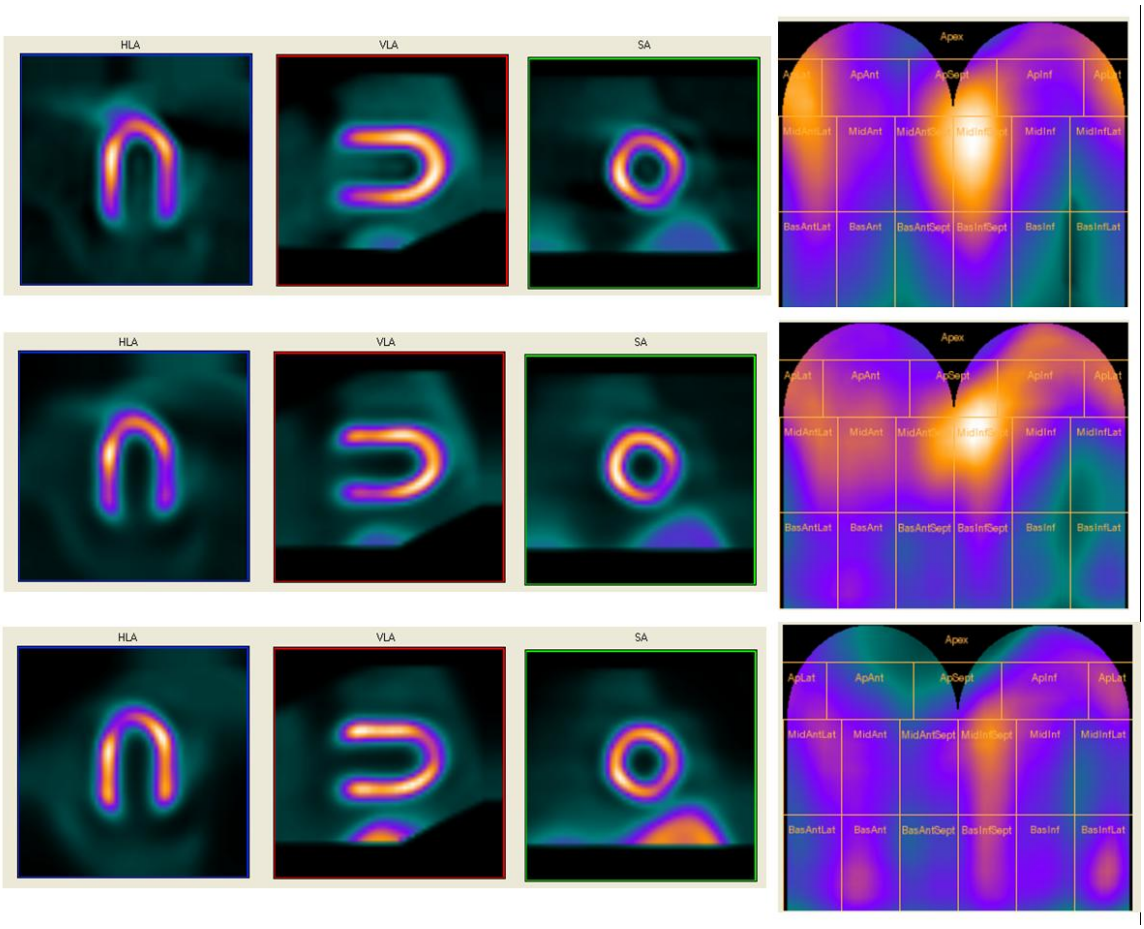

Figure 3.10: Sample slices and perfusion map of a male torso phantom reconstructed with FBP (top) OSEM-3D without (mid) and with scatter and attenuation correction (bottom)

technology, optimization of acquisition and/or reconstruction protocols, and quality control checks. We will use the tool in Chapter 4 to optimize cardiac imaging protocols.

3.3 3D+t Cardiac Image Analysis

SPECT acquisitions in clinical cardiac studies are usually gated to the electrocardiogram signal of the heart. The cardiac cycle is divided temporally in several time bins, usually 8 or 16 [13], and the resulting image sequence provides information about the movement of the heart muscle and the ejection fraction (EF).
In clinical routine, the reconstructed gated data is usually analyzed using comprehensive quantitative tools such as e.g. Corridor4DM (MedImage, Ann Arbor, Michigan), one of the major currently used quantitative cardiac analysis packages. This quantitative tools facilitate the diagnostic tasks in routine clinical work. However, they are not suitable for performing intense system tests or for creating baselines. For these purposes phantoms are used which have known tractable features.
In the following, we present an image analysis tool which evaluates functional parameters of cardiac gated studies. This tool is specifically designed for a dynamic cardiac phantom with a known geometry.

3.3.1 Target Phantom

The phantom employed is the Dynamic Cardiac Phantom manufactured by Data Spectrum, an anthropomorphic torso phantom with liver, lung, and spine inserts (Figure 3.11 left). The left ventricular blood pool and myocardium are mimicked by two latex membranes connected to a piston pump which simulates the filling and emptying of the blood pool. An ECG trigger signal is provided to perform gated acquisitions. The package includes a user interface to control the pump (Figure 3.11 right). End-diastolic volume (EDV), end-systolic volume (ESV), ejection fraction, and heart rate can be specified. In addition, the phantom software allows to 'freeze' the motion at 8 discrete positions of the cardiac cycle (see Figure 3.11 right, positions F2-F9). Figure 3.12 shows example CT images of the cardiac chamber in these positions. For demonstration purposes the myocardium was filled with CT contrast agent in these images.

3.3.2 Image Analysis

The myocardial segmentation and the blood pool volume estimation are performed slice by slice on the short axis (SA) images of the reconstructed volumes. The main steps for the image based blood pool volume estimation are illustrated in Figure 3.13. The initial segmentation of the myocardium is done by applying a threshold of 40%-50% of the maximum pixel value to the image slice. After thresholding, unwanted regions due to noise in the image are eliminated by applying a combination of region labeling, using prior knowledge of the myocardial shape, and morphological operations (compare e.g. [147]).

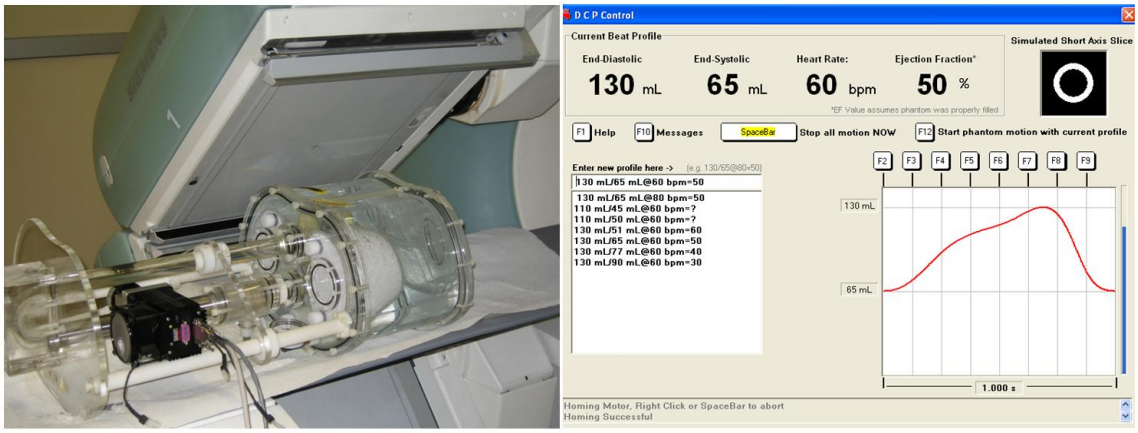

Figure 3.11: Dynamic Cardiac Phantom (left) manufactured by Data Spectrum and provided software to control cardiac parameters (right). The software allows for adjusting ESV, EDV, EF, and heart rate. In addition the phantom can be stopped at 8 discrete positions of the cardiac cycle (F2-F9).

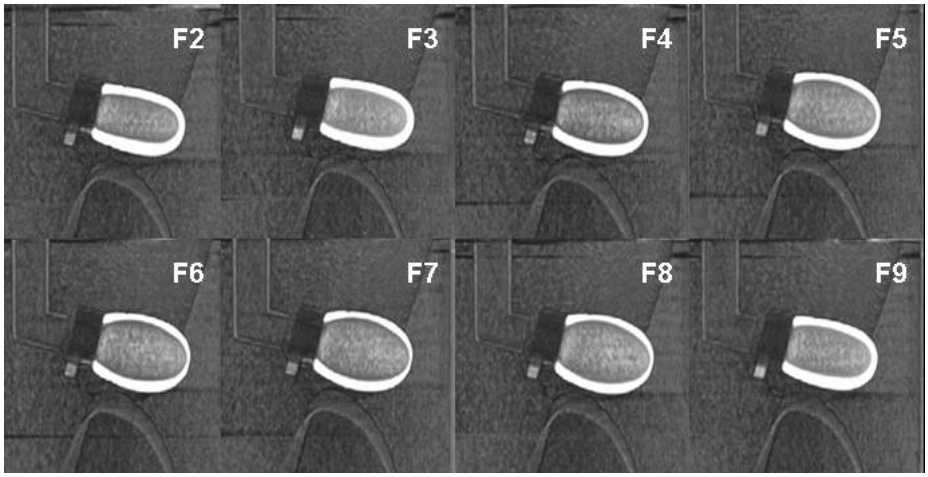

Figure 3.12: CT images of the dynamic phantom stopped at positions F2-F9 (see Figure 3.11 right). Volume parameters are set according to Figure 3.11 right. For visualization purposes, CT contrast agent is injected into the myocardial chamber.

In addition to the segmentation, a phantom specific model is introduced to facilitate the volume estimation. Since the phantom simulates the myocardium with two cylindrical membranes, a simple circular model is fitted to the segmented myocardium in the short axis slices. We use the parametric form for a circle:

$$x = r\cos\theta + x_0 \tag{3.7}$$
$$y = r\sin\theta + y_0\ , \tag{3.8}$$

with the radius r, the center coordinates x_0, y_0 , and $0 \leq \theta < 2\pi$.
For a given set of n points (x_i, y_i) with $i = 1, 2, \ldots, n$ representing the 2D positions of the segmented myocardial region in a short axis slice, the blood pool center coordinates x_0, y_0 are estimated as:

$$x_0 = \frac{1}{n}\sum_{i=1}^{n} x_i \tag{3.9}$$
$$y_0 = \frac{1}{n}\sum_{i=1}^{n} y_i\ . \tag{3.10}$$

We estimate the radius of the circle by minimizing the objective function $L(r)$ with respect to r:

$$L(r) = \sum_{i=1}^{n} \left(x_i - r\cos\theta_i - x_0\right)^2 + \left(y_i - r\sin\theta_i - y_0\right)^2\ . \tag{3.11}$$

Setting the first derivative to zero:

$$\begin{aligned}
\frac{\partial L}{\partial r} &= 2\sum_{i=1}^{n}\left(x_i - r\cos\theta_i - x_0\right)\left(-\cos\theta_i\right) + 2\sum_{i=1}^{n}\left(y_i - r\sin\theta_i - y_0\right)\left(-\sin\theta_i\right) \\
&= 2\sum_{i=1}^{n}\left(x_i - x_0\right)\cos\theta_i - r\sum_{i=1}^{n}\cos^2\theta_i + \sum_{i=1}^{n}\left(y_i - y_0\right)\sin\theta_i - r\sum_{i=1}^{n}\sin^2\theta_i \\
&\stackrel{!}{=} 0
\end{aligned} \tag{3.12}$$

and solving for r we derive the estimate of the radius:

$$r\left(\sum_{i=1}^{n}\cos^2\theta_i + \sum_{i=1}^{n}\sin^2\theta_i\right) = \sum_{i=1}^{n}\left(x_i - x_0\right)\cos\theta_i + \left(y_i - y_0\right)\sin\theta_i \tag{3.13}$$
$$r = \frac{\sum_{i=1}^{n}\left(x_i - x_0\right)\cos\theta_i + \left(y_i - y_0\right)\sin\theta_i}{n} \tag{3.14}$$

The radius of the blood pool used for the volume calculation is then derived by subtracting half of the known myocardial wall thickness.
Using a model based approach in addition to the thresholding shows its benefits especially in the case of high variations in pixel intensity caused e.g. by attenuation effects or 'blobby' images due to low signal to noise ratios.

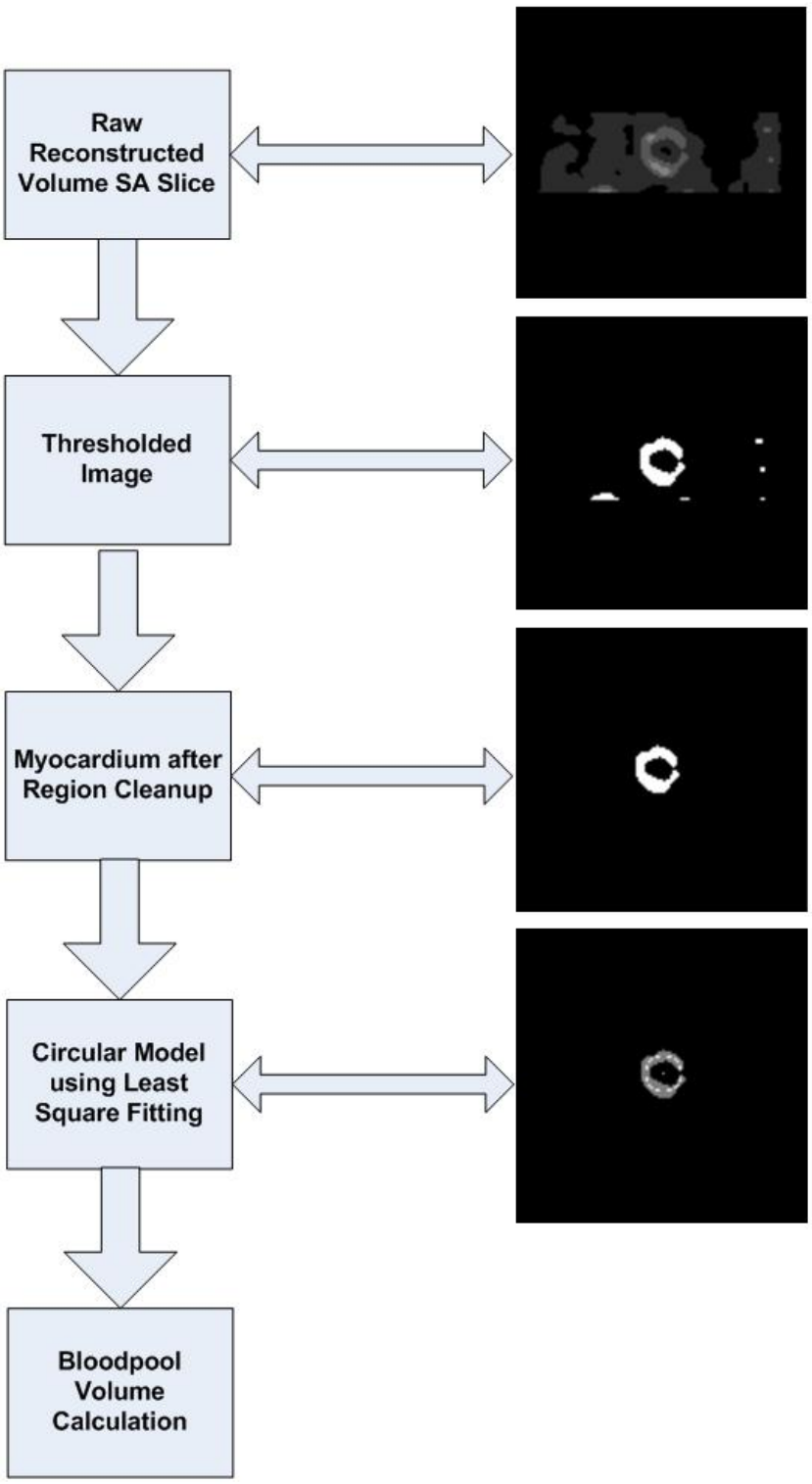

Figure 3.13: Main steps for image based blood pool volume estimation - a combination of thresholding and circular model calculation using prior knowledge of the phantom geometry.

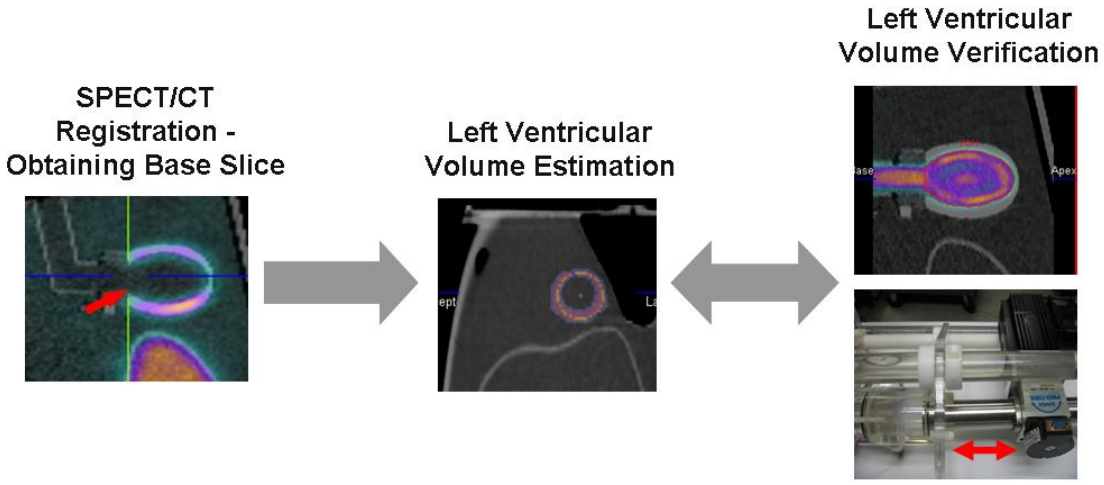

Figure 3.14: Overview of procedures for tool calibration and volume estimation and verification using the phantom's gold standard.

Since blood pool volume estimation is very sensitive towards the setting of the base slice, a base slice calibration is performed. Figure 3.14 gives a general overview of the procedures for tool calibration and volume estimation and verification using the phantom's gold standard. For the localization of the base slice, the SPECT data is superimposed with the hardware registered CT volume provided by the hybrid scanner. The determined base slice position is kept constant throughout the image analysis. The assumption of a constant base slice location can be justified, as there is no physical translation of the phantom's myocardium during the scan (unlike in patient studies).
Once EDV and ESV are derived, the EF is calculated as follows:

$$EF = \frac{EDV - ESV}{EDV} \ . \tag{3.15}$$

The truth model of the blood pool volumes and the ejection fraction is derived by two independent measurements. Image based volumetric analysis is performed on data from a cardiac blood pool study by acquiring ungated SPECT data of the phantom in the 8 discrete positions. In addition, physical measurements of the mechanical piston displacement of the pump are performed and the processed volume for each of the discrete pump positions is calculated (compare Figure 3.14).

3.3.3 Tool Validation

For the validation of the developed tool, myocardium, liver and background of the phantom are loaded with Tc-99m. The activity concentration ratio of heart:liver:background is set to 14:8:1.
Ungated high count SPECT/CT acquisitions of the 8 discrete pump positions (see Figure 3.11 right, positions F2-F9) are acquired and subsampled to clinical gated count levels. 5 Poisson realizations are generated from each high count data set. The

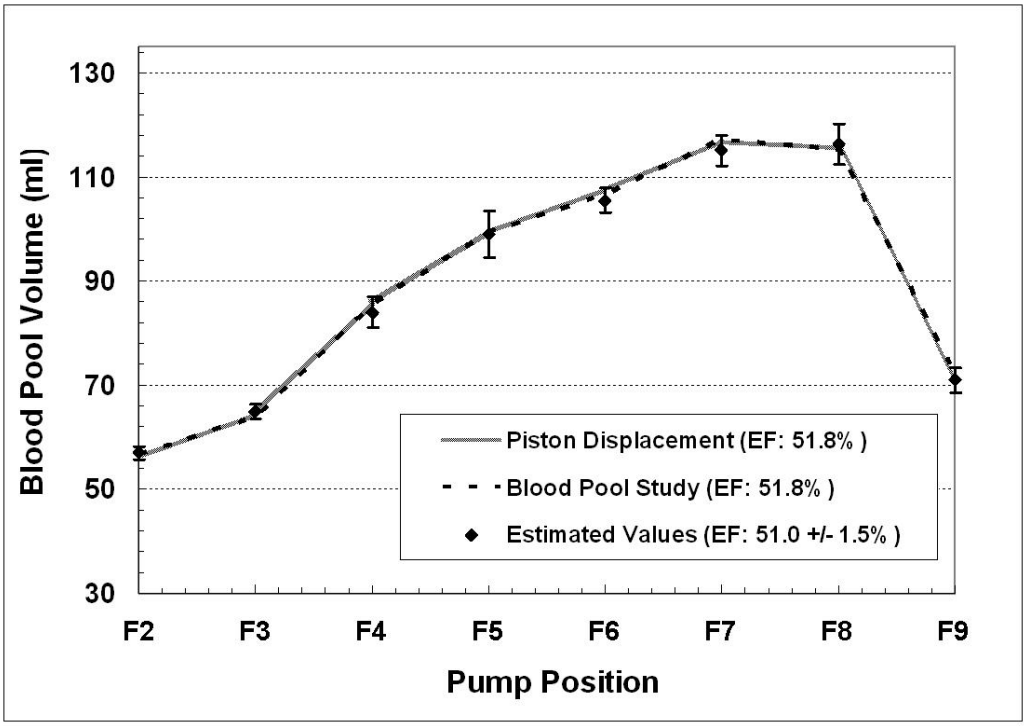

Figure 3.15: Estimated blood pool volumes for the 8 discrete pump postions and comparison with the truth model (piston displacement and blood pool study).

data are reconstructed using OSEM-3D without corrections for scatter and attenuation (according to clinical procedures). Figure 3.15 shows results for the absolute blood pool volumes as a function of pump position. Blood pool study and measurements of the piston displacement deliver identical results for the truth model. The calculated true EF is 51.8%. The analysis tool accurately estimates absolute volumes from reconstructed SPECT images and reports an EF of 51.0±1.5%.
Having performed this validity check, we conclude that the developed tool can be used to accurately assess functional parameters in the cardiac phantom. We will employ the tool for the optimization of cardiac imaging protocols in the following chapter.

Chapter 4

Optimizing Clinical Non-Quantitative Imaging Protocols

In this chapter we optimize clinical routine imaging protocols with focus on the cardiac application. We use the tools introduced in Chapter 3 to evaluate image features important for nuclear cardiac diagnosis such as activity uniformity and resolution recovery. The goal is to reduce the scan time of conventional cardiac protocols, which take between 15-25 minutes, by at least a factor of 2 while maintaining diagnostic ability.
We derive an optimized scan protocol by replacing conventional FBP reconstruction with iterative reconstruction which is then applied to time-optimized projection datasets. Phantom studies in combination with human observer studies are used to evaluate different acquisition scenarios. The best suited protocol is then validated with a reference phantom database and exemplary patient data.

4.1 Development of a Time-optimized Cardiac Imaging Protocol

Cardiac perfusion studies in clinical practice usually take between 15-25 minutes per acquisition depending on injected dose and desired counting statistics (see Table 2.2). Two scans are usually performed, one after exercise (stress) and one at rest. Following a one-day protocol, the stress and rest scan are performed the same day, whereas the first scan uses one third of the dose of the second scan [15].
FBP is still widely used to reconstruct nuclear cardiac images and is well supported in current imaging guidelines. These guidelines, however, give insufficient consideration to advances in iterative reconstruction methods that include collimator modeling, attenuation, and scatter correction. Thus, advanced reconstruction is often suboptimally used in a clinical setting. Literature provides some advise on how to set the various acquisition and reconstruction parameters for some applications [148, 149, 150, 151]. Still, in clinical practice variations in imaging protocols occur according to the specifics of the image formation including patient and tracer uptake. In general, advances in reconstruction techniques and instrumentation improve im-

Angular Sampling	Number of Projections	Time/ Projection	Detector Dead-time/ View	Count Density in Myocardium (cts/pixel)		Total Scan Time	
				128×128	**64×64**	Min.	%
3°	60	30s	3.1s	30	120	16:33	100%
3°	60	15s	3.1s	15	60	9:03	55%
6°	30	30s	4.9s	30	120	8:44	53%
9°	20	45s	6.7s	45	180	8:37	52%

Table 4.1: Different acquisition scenarios for time reduction in cardiac SPECT. Typical count densities are given for the first scan of a 1-day imaging protocol.

age quality. These improvements could be used to improve confidence and diagnostic ability, or to increase throughput or lower injected dose while maintaining diagnostic ability. Higher patient throughput can be achieved by reducing imaging scan time.
In this section, we aim to develop an acquisition protocol for SPECT cardiac imaging which reduces scan time without adversely affecting the clinical read. This is done by characterizing the effects of various acquisition and reconstruction protocols on cardiac image quality. Iterative reconstruction, instead of FBP, is used for the time-optimized imaging protocols.
We use phantom tests in combination with human observer studies to derive optimal acquisition and reconstruction parameters for the time-optimized protocol. This protocol is then validated using a database of independently filled phantoms, acquired on multiple SPECT/CT systems, and exemplarily tested on patient data.
Table 4.1 gives a set of different acquisition scenarios for ∼50% time reduced protocols. Scan time reduction can either be achieved by variations in angular sampling or by reducing detector dwell time per view. Note that reduction in dwell time yields increased noise. Typical clinical count densities in the myocardium for a single projection view are also shown in Table 4.1. These values are based on summed data acquired during the first scan of a 1-day protocol (low dose scan). For gated data, the count density values are to be divided by the number of time bins (typical 8 or 16).
In the following section we evaluate the different protocols given in Table 4.1 in terms of image quality and lesion detection ability. We use numerical assessment and human observer studies of images acquired with the cardiac phantom.

4.1.1 Phantom Preparation and Acquisition

The static cardiac phantom (Figure 3.2) introduced in Chapter 3 was used for the testing of different acquisition protocols. Measured data acquired with a clinical system were used instead of Monte Carlo simulation, which can only approximate a real clinical system. The phantom was filled as described in Table 3.2 in Chapter 3. For abnormal studies, a fillable lesion with an angular extent of 45° in the short axis and a length of 20 mm (displacement volume: 4.7 ml) was mounted in the mid-inferior

Head Separation Angle	90°
Scan Range	180°
Angular Step	1°
Orbit	non-circular
Pixel Size	1.65 mm
Matrix Size	256×256
Total Counts	90 million
Count Density in Myocardium	44-52 cts/pixel

Table 4.2: Acquisition parameters for the high-count reference data.

region of the cardiac insert and filled the entire radial extension of the wall. The activity concentration in the defect was 12.5% below the surrounding myocardium.
High-count data sets with dense angular and spatial sampling are acquired using a state-of-the-art clinical SPECT/CT system (Symbia-T6, Siemens Healthcare). Acquisition parameters are summarized in Table 4.2. The phantom was acquired from 45° left posterior oblique to 45° right anterior oblique with 90° head configuration according to clinical standard [13]. The data manipulation tool described in Section 3.1 was applied and the high-count reference data was processed in terms of counts and angular sampling to generate the different acquisition scenarios from Table 4.1. The exact count levels as well as OSEM-3D reconstruction parameters are given in Table 4.3. The matrix size was set to 64×64. The data was subsampled to count levels of gated time bins. These levels guaranteed an operation range with good statistical power for human observer studies.
The data was reconstructed with OSEM-3D and with FBP (Butterworth filter of order 5, cut-off: 0.4) for reference. Note that both the number of OSEM updates (iterations×subsets) and the number of views per subset maintained the same throughout the three different angular steps.

4.1.2 Phantom Image Analysis

A Receiver Operating Characteristics (ROC) [152] study has been performed on the scenarios presented in Table 4.3. A graphical user interface was used which gives the user a series of short axis images with a 50% chance of a defect being present. The images were ranked in a 5-step scale from definitely normal to definitely abnormal. The defect in the inferior wall appeared constantly at 6 o'clock in a short axis reconstructed slice, close to the position of the well-known infero-lateral (5 o'clock) artifact usually induced by the lack of attenuation correction.
For each row in Table 4.3 multiple realizations were generated from the high-count reference data: N/2 normal and N/2 abnormal sets (N=100). Prior to each ranking session the observer was able to run through a training with feedback. The data was

Total Counts	Counts/ view	Count Density (cts/mm^2)	Angular Step	Iterations	Subsets	OSEM Updates
900k	15k	0.45-0.70	3°	5	12	60
	30k	0.90-1.40	6°	10	6	60
	45k	1.50-1.80	9°	15	4	60
450k	7.5k	0.23-0.35	3°	6	6	36
	15k	0.45-0.70	6°	12	3	36
	22.5k	0.75-0.90	9°	18	2	36
450k	7.5k	0.23-0.35	3°	6	12	72
	15k	0.45-0.70	6°	12	6	72
	22.5k	0.75-0.90	9°	18	4	72
450k	7.5k	0.23-0.35	3°	12	12	144
	15k	0.45-0.70	6°	24	6	144
	22.5k	0.75-0.90	9°	36	4	144

Table 4.3: Generated acquisition scenarios and corresponding reconstruction parameters. Note: A post-smooth with a 3D Gaussian with a FWHM of 2 pixels is applied in all cases.

presented to 6 readers. After ranking, the ROC curves and the corresponding values for the area under the curve (AUC) and the standard error were calculated using the non-parametric model of Hanley et al. [152]. The AUC represents the degree of diagnostic ability for a certain task. An AUC of 1.0 would translate to a specificity and sensitivity of 100%, respectively. The Bootstrap method [153] (100 repeats/reader) was used to get estimates for the standard errors of the AUC values.

Table 4.4 summarizes the results of the ROC study, including the values of the AUC and their standard errors (SE).

In addition to the visual assessment, the N/2 reconstructed images of the normal phantom were analyzed in terms of myocardial nonuniformity and resolution using the analysis package described in Section 3.2. Table 4.5 shows the values for the nonuniformity and its standard error in percent as well as the FWHM of the wall thickness in millimeter and its standard error.

Figure 4.1 attempts to combine the information in Table 4.5 and Table 4.4 and to correlate detectability from an observer study as measured by AUC with a numerical characterization of an image feature, such as the myocardial nonuniformity. Values are shown for the acquisition protocols using 3°, 6°, and 9° angular sampling at total counts of 450k and 900k at increasing iteration updates (36, 72, and 144) using OSEM-3D. The 2D error bars correspond to standard errors of the AUC and nonuniformity, respectively.

In Figure 4.2 we plot the standard error of the AUC for all readers on the ordinate against the nonuniformity showing a minimum of the standard error around 11%. The reader variability as measured by the standard error of the AUC may be interpreted as an indicator for the confidence to make a detection decision. According to this, for the count level of 450kcts, 72 OSEM updates show highest AUC and reader confidence for all three tested angular steps.

In Figure 4.3 we show a graph which not only relates AUC and nonuniformity but also recovered resolution by measuring the FWHM of the wall thickness at 450k.

Total Counts	OSEM Updates	Angular Step	AUC	SE
900	36	3°	0.93	0.03
		6°	0.95	0.02
		9°	0.93	0.03
450	36	3°	0.88	0.04
		6°	0.89	0.03
		9°	0.90	0.03
450	72	3°	0.91	0.03
		6°	0.91	0.03
		9°	0.91	0.03
450	144	3°	0.75	0.05
		6°	0.85	0.04
		9°	0.83	0.04

Table 4.4: Results from ROC observer studies for the different acquisition scenarios.

Total Counts	OSEM Updates	Angular Step	Non-uniformity	SE	Wall Thickness	SE
900	36	3°	9.4%	0.1%	21.7	0.04
		6°	9.5%	0.1%	21.7	0.04
		9°	9.2%	0.1%	21.8	0.04
450	36	3°	9.7%	0.1%	23.9	0.05
		6°	10.3%	0.1%	23.9	0.07
		9°	10.0%	0.1%	23.9	0.06
450	72	3°	10.7%	0.2%	21.1	0.05
		6°	11.0%	0.1%	21.3	0.05
		9°	10.7%	0.2%	21.2	0.05
450	144	3°	12.3%	0.2%	19.9	0.06
		6°	12.2%	0.1%	19.8	0.04
		9°	12.3%	0.2%	19.8	0.05

Table 4.5: Numerical characterization of nonuniformity and wall thickness.

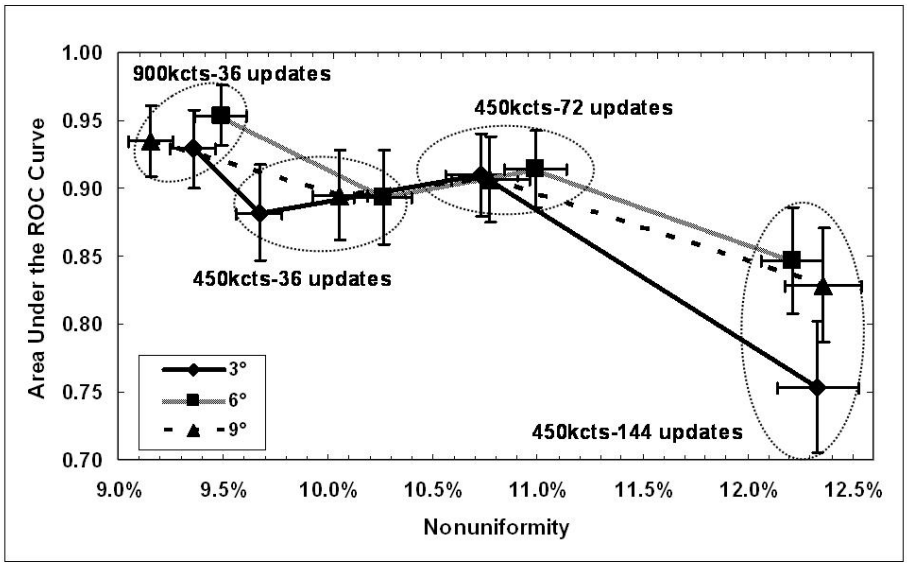

Figure 4.1: Correlating detectability with a measure for myocardial non-uniformity for 3°, 6°, 9° angular sampling, 36, 72 and 144 OSEM updates and 2 total count levels at 450kc, and 900kc. The 2D error bars show standard error of AUC and nonuniformity respectively.

Results for 3° angular sampling are shown. The left ordinate shows nonuniformity and AUC on the same scale, the right ordinate the FWHM of the reconstructed wall thickness (mm) and the abscissa shows the number of OSEM updates. The more updates the better the resolution recovery, yet nonuniformity worsens. The AUC remains stable and worsens once nonuniformity worsens above some threshold which is around 72 updates. A collective result derived from graphs (4.1, 4.2, and 4.3) is an increase in detection ability and reader confidence with increasing resolution recovery and a decrease above a nonuniformity level of approximately 11%. It seems plausible that the interplay between resolution and nonuniformity are the key drivers for this particular detection task in this application. The results indicate that nonuniformity impacts detection performance more significantly than resolution. These findings also correspond to feedback from physicians who usually like to see a smooth myocardium yet with the best possible resolution.
Figure 4.4 depicts the standard error as it trends with the decrease in infero-lateral intensity for 3°, 6°, and 9° angular sampling at total counts of 450k and 900k. The intensity decreases from -17% to -20% with decreased total counts, while the standard error increases from 2.5% to 3.5%. The slope is essentially the same for 3° and 9° angular sampling, but for 6° the range of intensity change is compressed and thus the slope is steeper.

Returning to the actual goal of reducing scan time using the different acquisition scenarios from Table 4.1, we can conclude that variations in angular sampling from 3° to 9° have only little impact on the overall detection ability of the defect given that nonuniformity is below 11%. For higher nonuniformity values we observe that 6° sampling performs best in terms of detection ability (Figure 4.1) and reader confidence (Figure 4.2). In addition, for 6° sampling infero-lateral intensity appears to

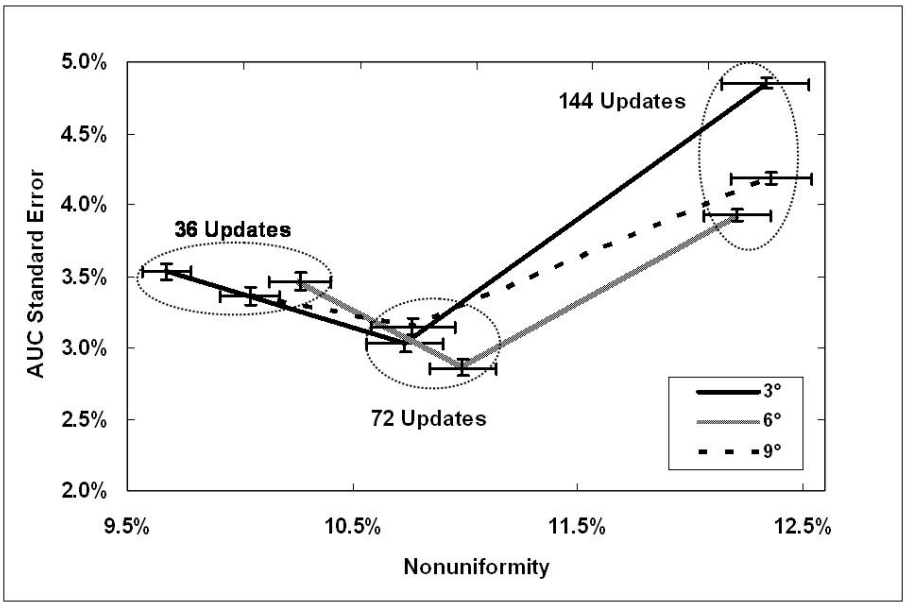

Figure 4.2: The standard error of the AUC using bootstrap is correlated with nonuniformity.

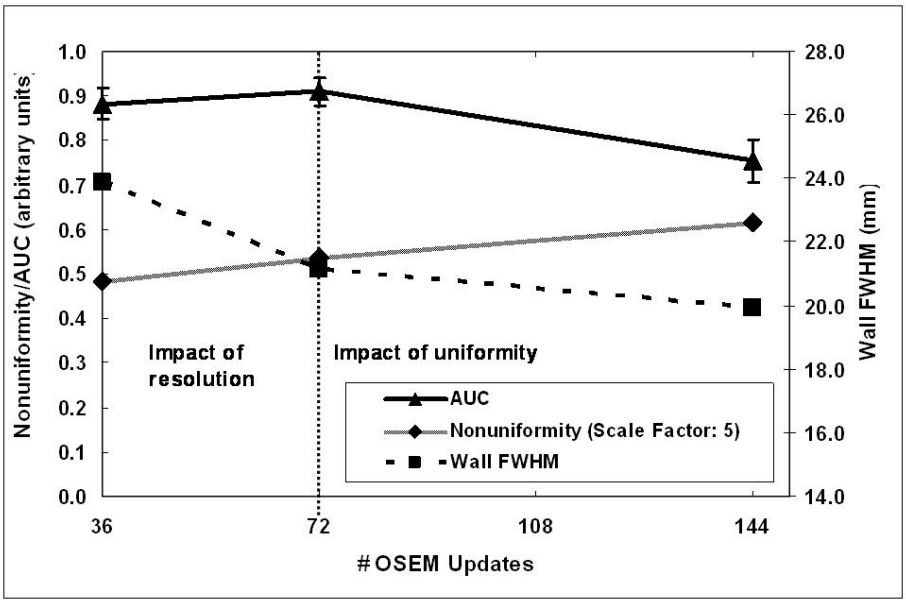

Figure 4.3: The left ordinate shows nonuniformity and AUC on the same scale and the right ordinate the FWHM of the reconstructed wall thickness (mm) and the abscissa shows the number of OSEM updates. The more updates the better the resolution recovery, yet nonuniformity increases. However the AUC remains stable and decreases once nonuniformity exceeds a certain threshold which in this case is around 72 updates.

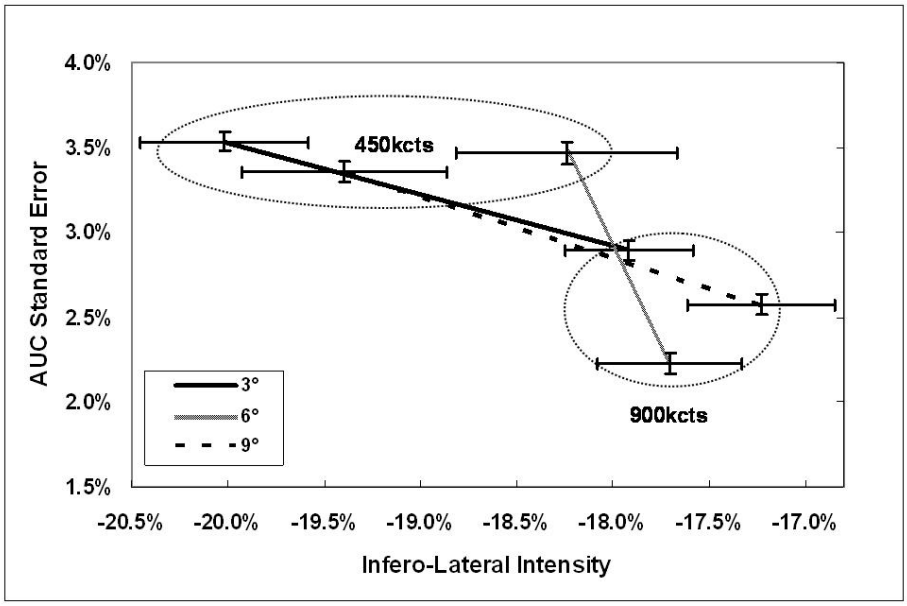

Figure 4.4: The standard error of the AUC using bootstrap is correlated with a numerical characterization of the infero-lateral intensity decreases for 3°, 6°, 9° angular sampling and the 2 total count levels of 450kc, and 900 kc.

be less affected by the count level.
We relate these outcomes to the fact that 6° sampling still gives a sufficiently dense angular representation of the object while at the same time offering adequate signal to noise ratio in each projection view (compare Table 4.1). This leads to a good performance of the applied OSEM based reconstruction for this specific detection task. As a result we choose a half-time imaging protocol which uses 6° angular sampling and OSEM-3D reconstruction (Table 4.1 third row) as compared to the conventional full-time protocol with 3° sampling and FBP reconstruction. In the following we validate this half-time protocol using a reference phantom database and exemplary patient studies.

4.2 Validation of the Time-optimized Imaging Protocol

We have developed a cardiac imaging protocol which allows a time reduction of ∼50%. During the image assessment we focused on image features extracted from the static 3D activity distribution in the target object which corresponds in-vivo to the 3D perfusion characteristics of the myocardium. The nuclear physician uses the 3D information of the ativity distribution to assess myocardial perfusion or viability. In addition, ECG-gated images are used to evaluate the functional characteristics of the heart muscle. In the following, we validate our time-optimized imaging protocol

	Non-uniformity	Wall Thickness	Apical Thinning	5 o'clock Intensity	Inf. vs. Ant. Intensity	Sept. vs. Lat. Intensity
FBP	8.3±0.4	20.8±0.5	2.2±1.9	-17.5±1.5	-12.0±2.4	8.0±2.1
OSEM-3D uncorrected	8.1±0.5	20.4±0.6	1.2±2.1	-18.9±2.0	-21.2±2.9	10.4±2.8
OSEM-3D corrected	7.4±0.6	20.5±0.6	13.0±1.6	-6.8±2.2	-2.3±2.9	10.8±3.2

Table 4.6: Numeric results for characterization of reference phantom data sets.

in terms of perfusion as well as functional consistency with conventional FBP based protocols.

4.2.1 Perfusion Characteristics

For the validation of the half-time imaging protocol we use phantom data from a reference database which was assembled over time. We use 14 data sets from cardiac phantoms filled independently and acquired on three different clinical SPECT/CT systems (Symbia T2/T6, Siemens Helathcare) within a time period of one year. This allows us to account for variabilities in phantom filling as well as for varying performance of different imaging systems, which includes different calibration and quality control states of the imaging systems. The phantoms were acquired according to a standard clinical protocol (see Table 2.2) collecting ∼6 million total counts in 64 projection frames (3°, full-time).
The full-time (3°) phantom data were reconstructed with FBP using a Butterworth filter with a cut-off value of 0.44. The half-time data were reconstructed with OSEM-3D with and without scatter and attenuation correction using 18 iterations and 2 subsets and a post-smooth of 2 pixels (3D Gaussian). Note that the number of subsets were divided by a factor of two compared to the recommended values for 3° sampling (Table 2.2), in order to keep the same number of projection views per subset compared to conventional protocols.
Reconstructed images were processed with the phantom analysis tool (Section 3.2). Mean values and standard deviations of the extracted numerical values are given in Table 4.6.

Short axis (SA), horizontal long axis (HLA), and vertical long axis (VLA) image slices and polar maps of a representative data set are shown in Figure 4.5. The first row shows the full-time FBP protocol and the second and third row show the half-time imaging protocol with OSEM-3D reconstruction without (2nd row) and with (3rd row) scatter and attenuation correction. Visually the images correlate well with the numerical findings in Table 4.6. Uniformity and wall thickness of all three datasets are comparable, with slight improvements for corrected images (3rd row). In Table 4.6, the 5 o'clock intensity and inferior-to-anterior wall intensity are slightly more pronounced in the uncorrected OSEM-3D case (2nd row) compared to the FBP

case. We relate this behavior to the better activity recovery of OSEM-3D in the anterior wall (see Figure 4.5). This increases the magnitude of the inferior-to-anterior intensity ratio. OSEM-3D with attenuation and scatter correction (3rd row) gives more balanced results. The activity depression in the apical region for the corrected OSEM-3D case is a known effect and related to a combination of different factors such as the imaging geometry, position of the cardiac insert, and distribution of background activity [154]. Attenuation correction emphasizes the effect by boosting intensities in the basal regions.

Figure 4.6 gives a visual impression of both full-time and half-time protocol ap-

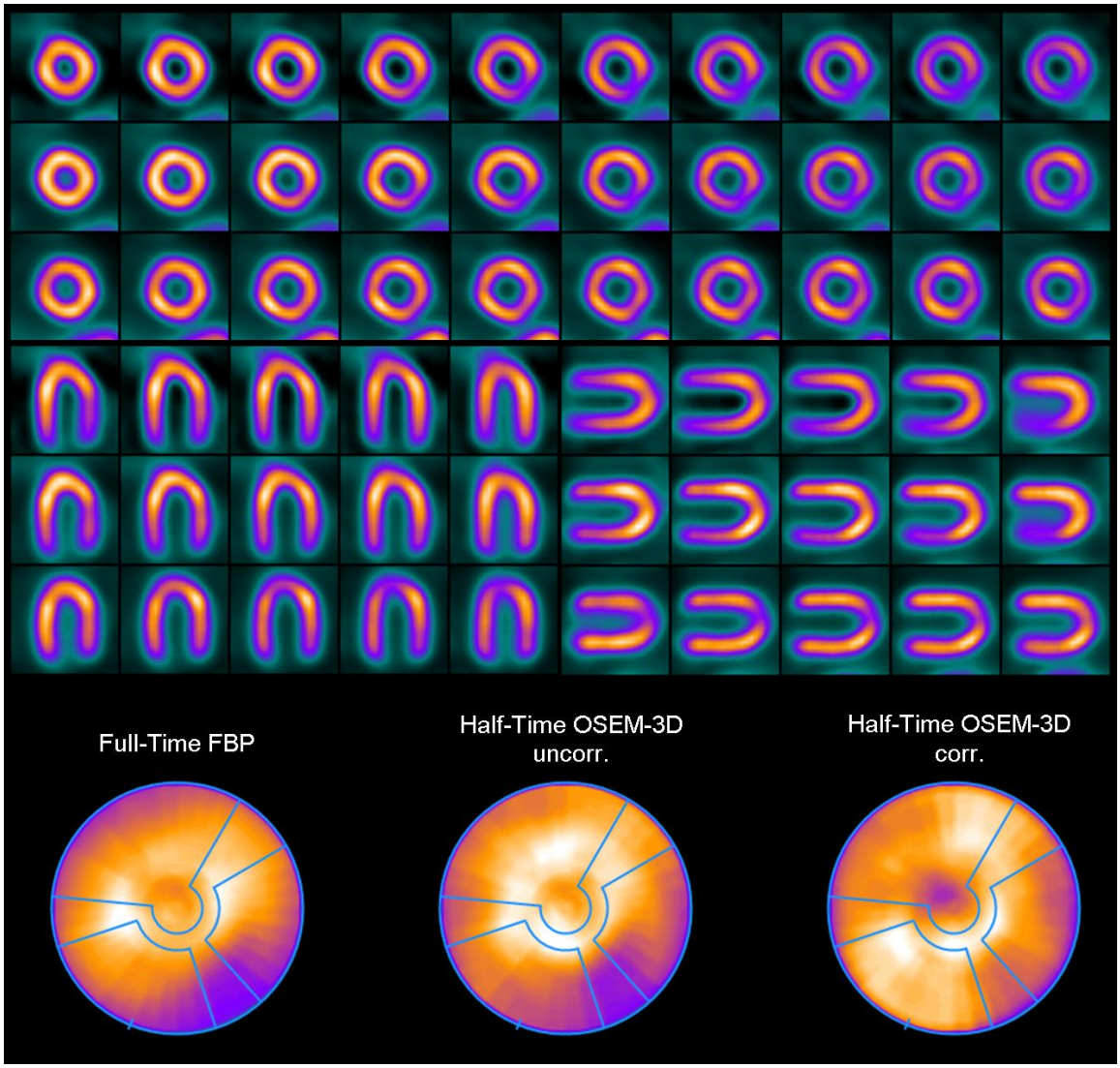

Figure 4.5: Example images from normal phantom database comparing full-time FBP with half-time OSEM-3D protocol. Top row: Full-time FBP reconstruction. Mid row: Half-time OSEM-3D uncorrected reconstruction (detector response correction only). Bottom row: OSEM-3D corrected reconstruction (detector response, scatter, and attenuation correction).

plied in an in-vivo patient study. The images were acquired at the Clinic of Nuclear

Medicine at the University of Erlangen-Nuremberg by following a standard 1-day stress/rest protocol with acquisition parameters according to Table 2.2. Injected dose was 319 MBq for stress and 698 MBq for rest. The projection data were retrospectively processed to simulate the half-time acquisition protocol. Reconstruction parameters were identical to those applied in the previous phantom studies.

The proposed half-time imaging protocol was furthermore evaluated in a prospective

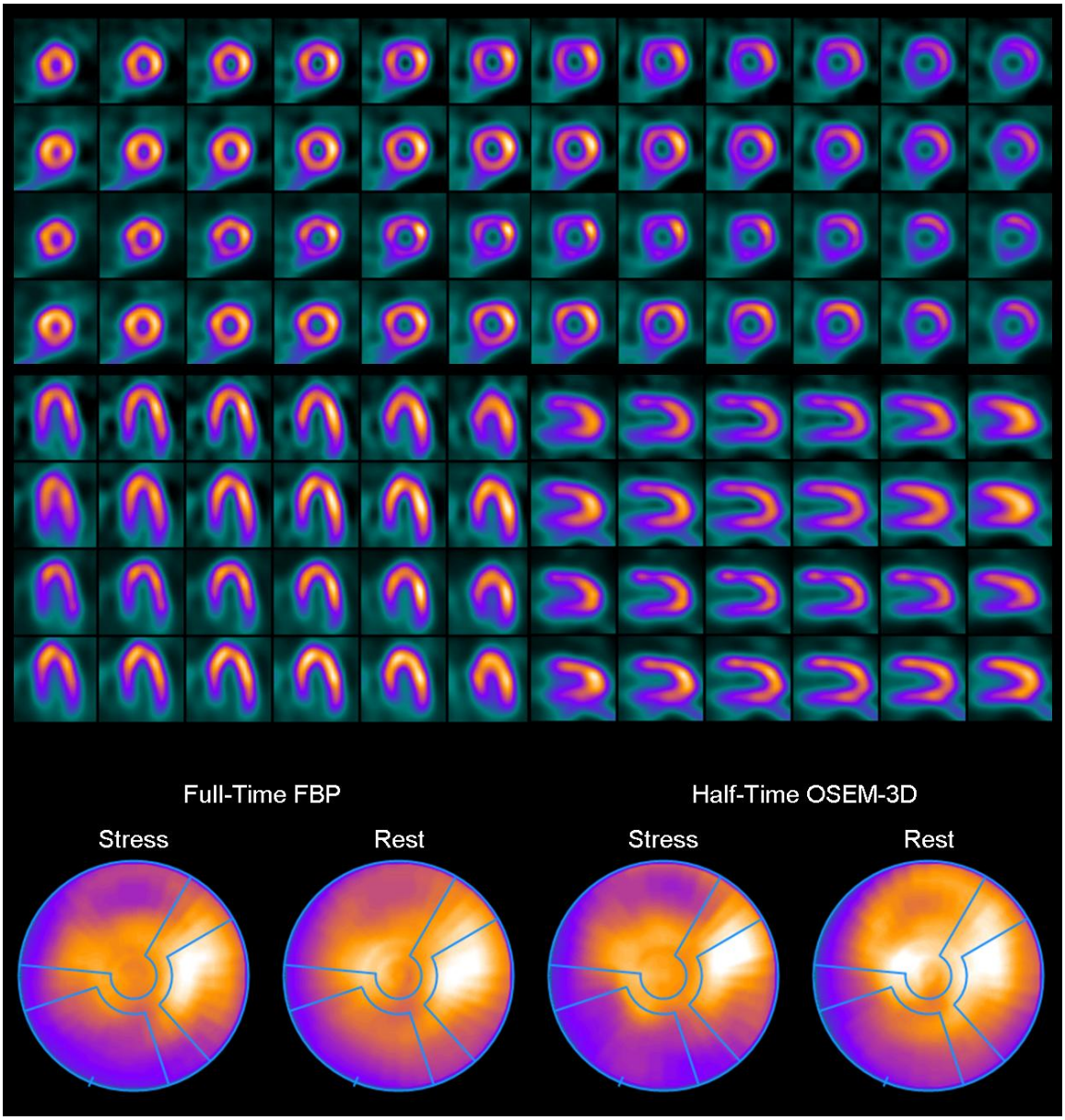

Figure 4.6: Example patient images and polar maps comparing full-time FBP versus half-time OSEM-3D protocol (56 year old normal male patient). 1st and 2nd row: Stress and rest images with full-time FBP protocol. 3rd and 4th row: Stress and rest images with half-time OSEM-3D protocol.

patient trial at the Iowa Heart Institute (Des Moines, Iowa, USA). 27 patients (18 male, 9 female) were acquired in back-to-back acquisitions with a dual headed large FOV (e.cam, Siemens Healthcare) and a dedicated cardiac imaging system (c.cam,

Siemens Healthcare) using the 3° and 6° acquisition protocol, respectively. The investigators on-site reported a good correlation between full- and half-time protocol. Figure 4.7 reflects the principle findings. It shows the correlations for the summed stress score (SSS) and summed rest score (SRS) which represent the readers' perfusion scores summed over the 17 segments of the myocardium for stress and rest, respectively. The mean differences between full- and half-time SSS and SRS were reported to be 2.44±2.50 and 0.15±3.06.

Overall, from results of numerical and visual evaluation of phantoms and a prospec-

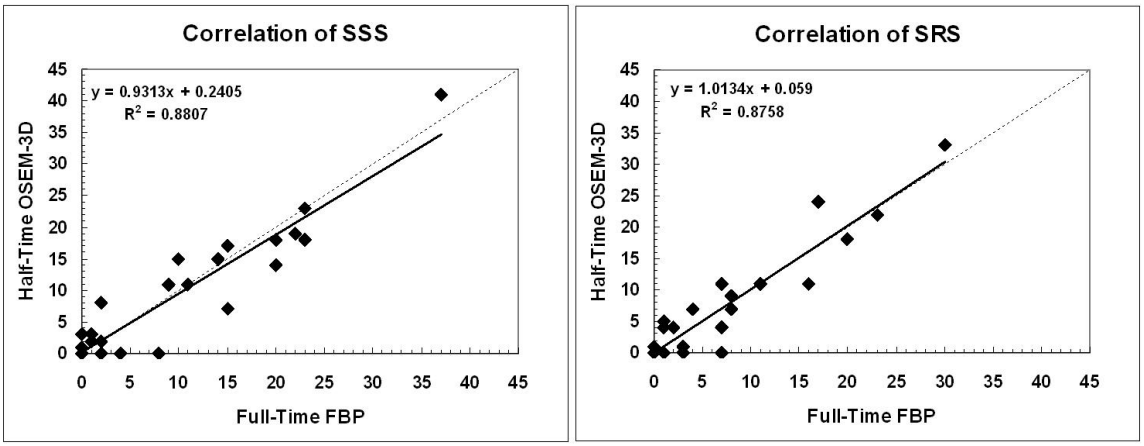

Figure 4.7: Results from a prospective patient study conducted at the Iowa Heart Institute (Des Moines, Iowa, USA). Correlation of summed stress score (SSS) and summed rest score (SRS) of full-time FBP and half-time OSEM-3D for a set of 27 patients.

tive clinical trial, we can summarize that the perfusion characteristics are comparable between the proposed time-optimized and the conventional protocol. In the following, we will evaluate the functional characteristics using ECG-gated image data.

4.2.2 Functional Characteristics

We validate the proposed imaging protocol for the use with gated acquisitions by employing the dynamic phantom and the designated analysis tool both which were introduced in Chapter 3.

For image acquisitions with a dual headed SPECT/CT system (Symbia-T2/T6) the dynamic phantom was loaded with Tc-99m using an activity concentration ratio of heart:liver:background of 14:8:1. High count ECG-gated data sets with dense angular and spatial sampling were acquired. Gated timeslots, matrix size, and ejection fraction were varied according to Table 4.7. From the measured high-count data, full- and half-time projection data were created. The myocardial count density in the projection data was approximately 4.5cts/cm^2. In order to increase statistics, five realizations for each data set shown in Table 4.7 for both clinical as well as half-time count levels were created (160 generated data sets total). The data were reconstructed using FBP (Butterworth filter with cut-off 0.4) and OSEM-3D using 6 iterations, 2 subsets, and 2 pixel post-smooth. Images were analyzed in terms of ejection fraction

Matrix Size	# of Timeslots	Ejection Fraction (%)
128	8	30, 40, 50, 60
	16	30, 40, 50, 60
64	8	30, 40, 50, 60
	16	30, 40, 50, 60

Table 4.7: Dynamic phantom gated acquisition parameters

using the analysis tool dedicated for the dynamic phantom. Figure 4.8 gives a summary of the results for the two different matrix sizes and number of time slots. The left column shows the correlation between full- and half-time protocol. The right column shows the Bland-Altman plots [155] which give a visual impression of the agreement of the two methods. The dotted lines in the Bland-Altman plots indicate ± 1.96 times the standard deviation of the differences of the two methods (values on the ordinate). The horizontal solid line indicates the mean of the differences.

In Figure 4.9 we show the deviations of the measured EF from the true values in the phantom for each combination of matrix size and number of time slots. Each bar shows the average of the 4 different EF settings (see Table 4.7) and the 5 realizations for each EF setting.

Summarizing Figures 4.8 and 4.9, we observe that the EF values for full- and half-time correlate well ($R^2 > 0.97$), except for 16 gates and a 128×128 matrix, which also show a $-27 \pm 9\%$ deviation from the true EF. We relate this to the low signal to noise ratio in the projection data which is in this case 8 times lower than e.g. for 8 time bins and a matrix size of 64×64. Best agreement with the true EF results from data with 16 gates and a matrix size of 64×64. In this case the cardiac cycle is temporally well resolved while the projections offer sufficient count density.

This particular gating protocol was tested in-vivo in a retrospective pilot study using 12 patients. The data were provided by the Iowa Heart Institute (Des Moines, Iowa, USA). The half-time projection data were generated retrospectively and the reconstruction parameters were identical to the phantom studies. The EF was measured using Corridor4DM (MedImage, Ann Arbor, Michigan). Figure 4.10 shows the correlation of full- and half-time protocol and the Bland-Altman plot.

For the sake of completeness, we also quote the EF outcomes from the prospective patient study at the Iowa Heart Institute mentioned in the previous section. Figure 4.11 gives the correlation and Bland-Altman plot for 8 gates and a matrix size of 64×64.

Overall, we can summarize that the estimation accuracy of ejection fraction in gated cardiac SPECT imaging with the proposed half-time protocol is comparable to the standard FBP-driven protocol. Best results in phantoms were obtained using 16 gates and a matrix size of 64×64.

4.3 Summary

We proposed an imaging protocol which reduces the myocardial perfusion acquisition time by $\sim 50\%$ when using iterative reconstruction with 3D detector response correc-

tion (OSEM-3D) instead of conventional FBP-based methods. We employed human observer studies and numerical analysis of an anthropomorphic torso phantom and tested various half-time acquisition scenarios. Based on the results we chose an acquisition protocol which maintains the dwell time per view, but reduces the number of projections by a factor of two. The resulting protocol offers a time reduction of 53%, considering the slightly increased detector dead time per view. The half-time protocol was tested both in terms of perfusion and functional characteristics using phantoms and patient data. The results show good correlation and agreement with the conventional FBP-driven protocol. Clinical reconstruction times of commercial iterative reconstruction packages are fast and thus OSEM-3D can be routinely used for the entire processing of nongated and gated datasets.

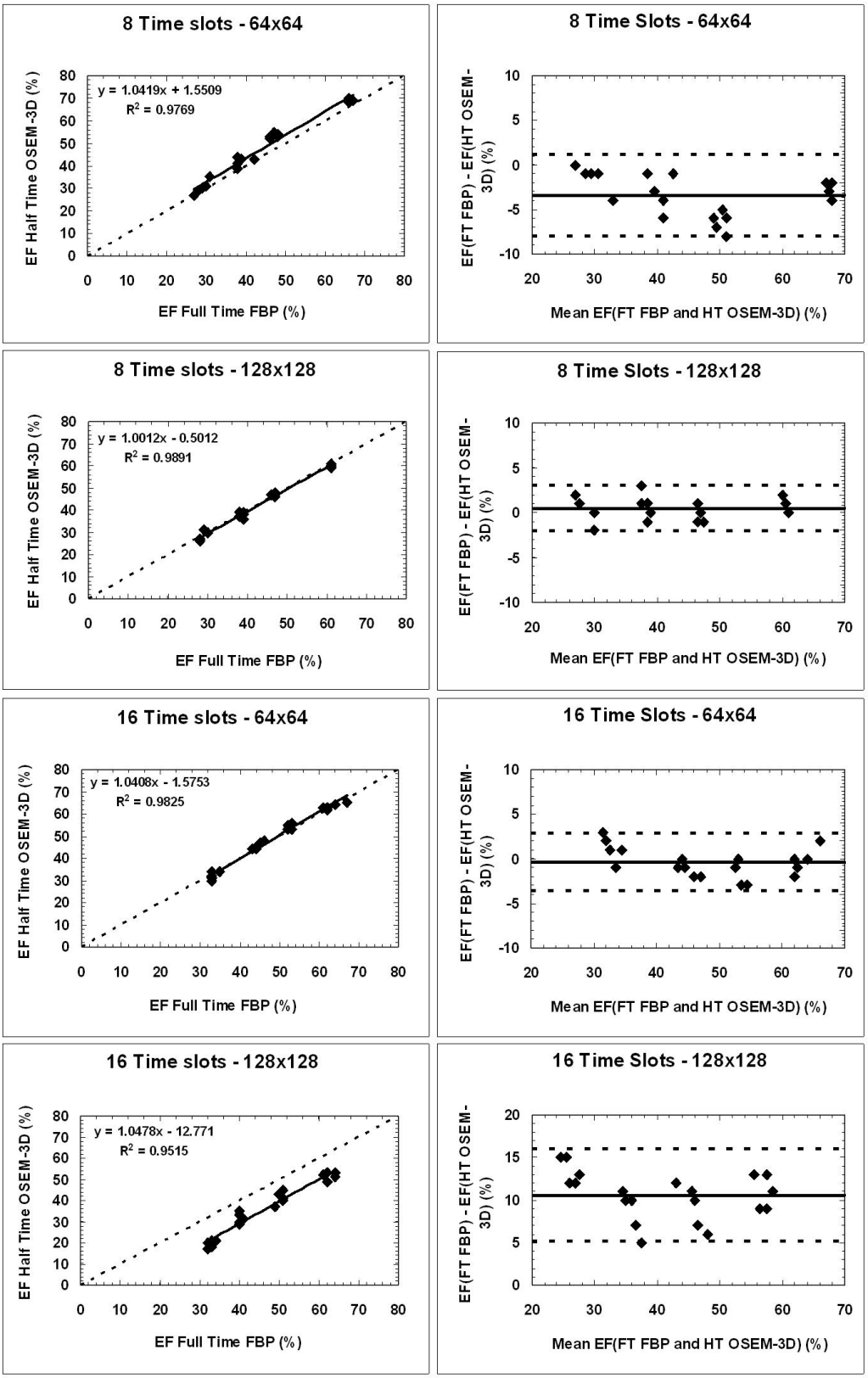

Figure 4.8: Results form phantom studies. Correlation analysis (left column) and Bland-Altman plots (right column) of full-time FBP versus half-time OSEM-3D gated datasets.

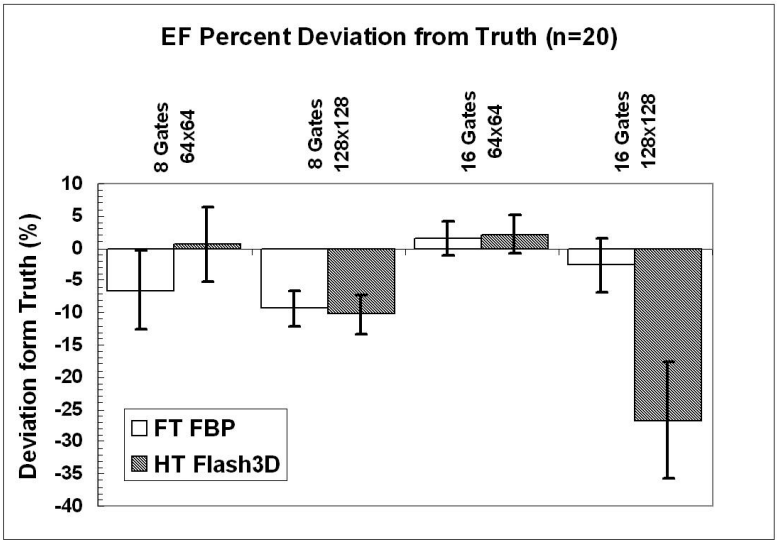

Figure 4.9: Deviation of measured EF values in the phantom images from the true values.

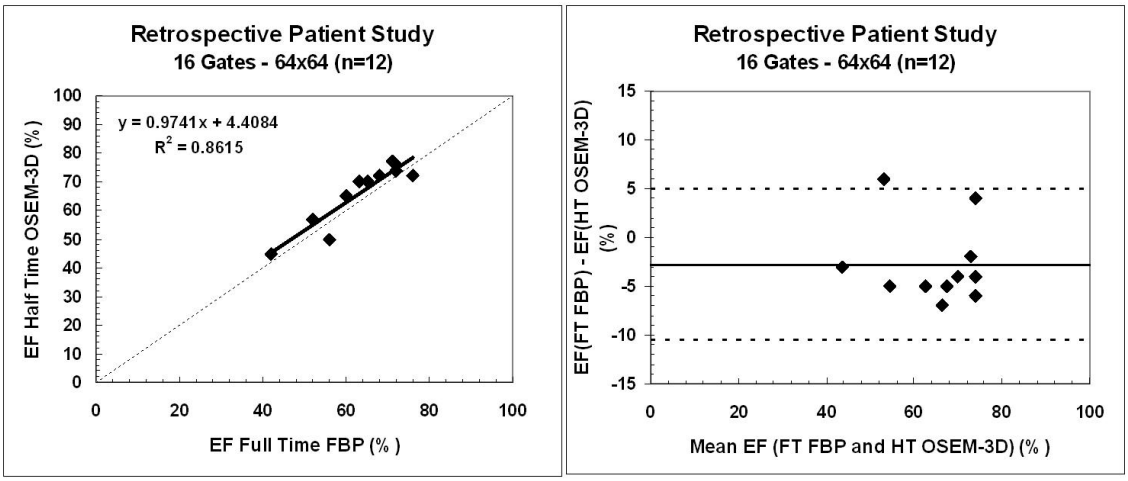

Figure 4.10: Correlation analysis (left) and Bland-Altman plot of a pilot set of 12 patients (gated stress data acquired at the Iowa Heart Center, De Moines, Iowa).

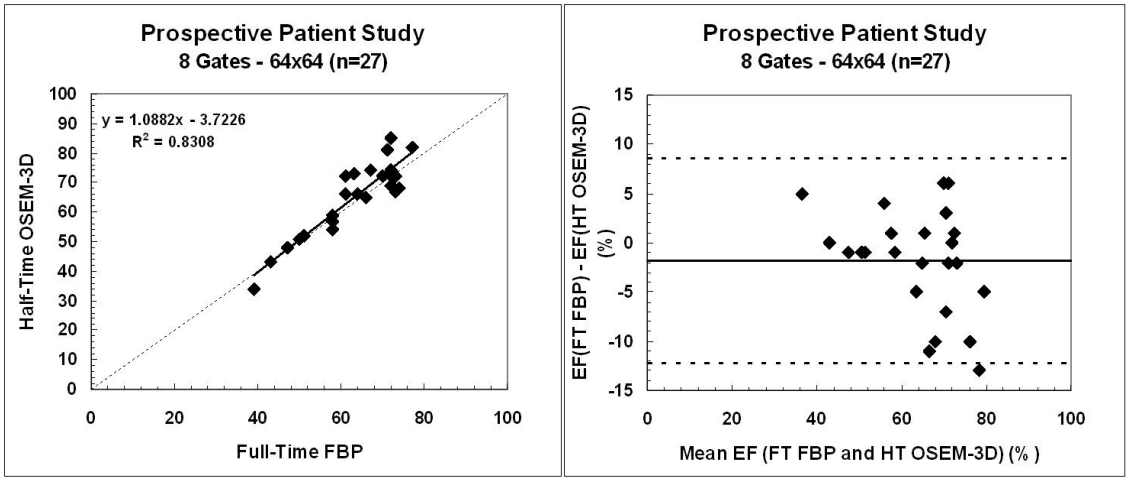

Figure 4.11: EF correlation analysis (left) and Bland-Altman plot (right) for image data from the prospective patient study conducted at the Iowa Heart Institute (Des Moines, Iowa, USA).

Chapter 5

Optimizing Quantitative SPECT Imaging Protocols

In the previous chapter we have optimized clinical cardiac imaging with focus on scan time reduction. For this, we modified the image acquisition protocol of a clinical SPECT system while aiming for consistent diagnostic ability. The image interpretation of the images remained conventional. It was based on pixel intensities which are delivered by the imaging system and aim to represent the activity distribution in the target object.

We briefly discussed in Chapter 2 that the image representation delivered by a state-of-the-art imaging system does not express the real activity distribution in absolute terms (e.g. kBq/ml). Numerous factors affect absolute quantification in SPECT (see Table 2.4). The clinical introduction of iterative reconstruction including corrections for physical phenomena has not only improved image quality but also quantitative accuracy. Still, absolute quantitative information is usually not used for routine diagnosis and image interpretation in clinical practice is still based on intensity (count) values and not on values such as e.g. absolute activity concentration.

Active research is conducted to provide the clinical user with absolute quantitative values based on reconstructed SPECT images. We have summarized some of the previous work in Section 2.4. These studies confirm that image corrections such as detector response, attenuation, and scatter correction are mandatory for accurate quantification. OSEM reconstruction inherently behaves non-stationary with respect to object size and position and number of iterations. In the present chapter we seek to develop and evaluate an approach to quantitative SPECT by taking into account this non-stationary behavior of OSEM reconstruction when used in the clinical operation range. We assess the dependencies of activity estimation errors on structure size, pixel size, count density, and reconstruction parameters. Using the obtained results we develop a calibration method for the determination of activity concentrations in kBq/ml which can be applied to a clinical SPECT/CT system. We explicitly employ standard commercial iterative reconstruction software with depth dependent 3-dimensional resolution recovery, with CT based attenuation correction and energy window based (TEW) scatter correction. We use available technology to assure clinical practicability including acceptable reconstruction times and a familiar operation environment. The method is validated with phantoms and applied to in-vivo patient

data.
Furthermore, we apply the method to dynamic SPECT data using a self-developed dynamic phantom. The goal is to establish a baseline for image based dynamic SPECT using a slow-rotating dual-headed gamma camera system.

5.1 Clinical System Calibration Technique

To obtain quantitative values from reconstructed SPECT images, a thorough characterization and calibration of the underlying imaging system is necessary. We propose three distinct steps to derive absolute activity concentrations in kBq/ml starting from conventional counts in the reconstructed image:

Step 1: Characterization
Characterization of the SPECT/CT imaging system in terms of emission recovery.

Step 2: Calibration
Cross calibration of the SPECT/CT imaging system with a well counter.

Step 3: Validation
Application of correction factors derived from steps 1 and 2 to reconstructed image data.

In the following, we further particularize these three steps. We begin with a comprehensive characterization of a clinical SPECT/CT system by taking into account variations in instrumentation and acquisition and reconstruction parameters. Thereafter, the procedure for the cross-calibration is presented which includes considerations about the precision of the measurement instrumentation and procedures. The results are then used for the determination of activity concentrations in phantoms and in-vivo in patients.

5.1.1 Step 1: Characterization of the Imaging System

For the characterization of a state-of-the-art imaging system we use quasi-analytical simulations of a clinical SPECT system with a voxel size of 0.6 mm in image and data space. The projection operator is modeled in 3D according to the detector and collimator specifications of the Symbia T-series gamma cameras (Siemens Healthcare) using different low energy collimators with sensitivities between 45 cps/MBq and 459 cps/MBq and geometric resolution FWHM between 4.4 mm and 13.1 mm at 10 cm distance. The detector intrinsic resolution FWHM is set to 3.8 mm. Figure 5.1 illustrates the system resolution of four Siemens low energy collimators, Low Energy High Sensitivity (LEHS), Low Energy All Purpose (LEAP), Low Energy High Resolution (LEHR), and Low Energy Ultra High Resolution (LEUHR), as a function of distance to the detector surface. Table 5.1 gives additional characteristics of the collimators such as acceptance angle, sensitivity, and bore length.
The point spread function (PSF) in the simulations for each voxel in image space is

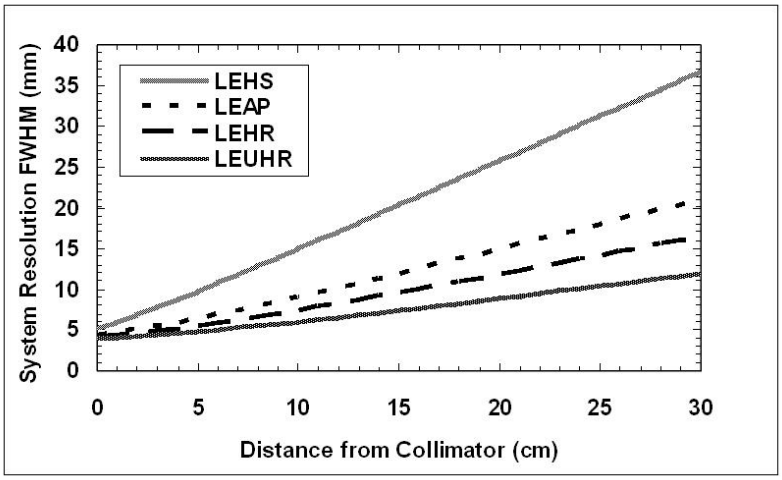

Figure 5.1: System resolution as a function of distance to the detector surface for four Siemens low energy collimators. The intrinsic resolution is set to 3.8 mm.

	Acceptance Angle (°)	Sensitivity (cps/MBq)	Bore Length (mm)	Hole Diameter (mm)
LEHS	6.60	459	24.05	2.54
LEAP	3.72	149	24.05	1.45
LEHR	2.84	91	24.05	1.11
LEUHR	1.98	45	35.80	1.16

Table 5.1: Collimator specifications of four Siemens low energy collimators.

modeled by a 3D Gaussian kernel with a FWHM calculated using the distance from the point of origin to the interaction plane in the detector. Projections are generated by assigning counts according to detector and collimator specific sensitivity and geometry conditions to a 512×512 detector array with a bin size of 0.6×0.6 mm. For each detector pixel a Poisson realization is created using the projected pixel count value as the mean. Photon attenuation in the simulated object is accounted for using a constant linear attenuation coefficient of 0.15 cm^{-1} (140 keV in water with narrow beam geometry). A μ-map is generated for attenuation correction. Due to the lack of an accurate scatter model an acquisition with perfect scatter rejection of 140 keV (Tc-99m) photons is assumed.

To demonstrate the effect of varying system resolution on emission recovery, a standard quality control phantom (Deluxe Jaszczak Phantom^{TM}, Data Spectrum) with varying sized rods with diameters between 4.8 mm and 12.7 mm is simulated with the four different low energy collimators from Table 5.1. A data pixel size of 2.4 mm is used and the background activity is set to 10% of the rod activity. The total acquisition time is constant for all collimator types resulting in total count values of 15, 30, 45, and 150 million for LEUHR, LEHR, LEAP, and LEHS respectively. Figure 5.2 shows the truth model (top) and reconstructed images for each collimator. OSEM was used for image reconstruction including 3D (transversal and axial)

resolution recovery and attenuation correction. Both the 3D point spread function and the attenuation effect are modeled in the forward and backprojection steps of the reconstruction.
For the images in Figure 5.2 the reconstruction was stopped after the 3rd largest rods (9.5 mm) reached their true diameter. The rod size in the reconstructed image was estimated by using the 2nd order moment of the pixel value distribution. The eigenvalues of the covariance matrix were used to calculate the principle axis of the ellipse which represents the rod in the image.
Figure 5.2 also gives the number of updates needed to reach the true resolution for each of the collimators. Using LEHS the true object size was not reached after 300 updates.
In the following we evaluate the images in terms of emission recovery. After deriving

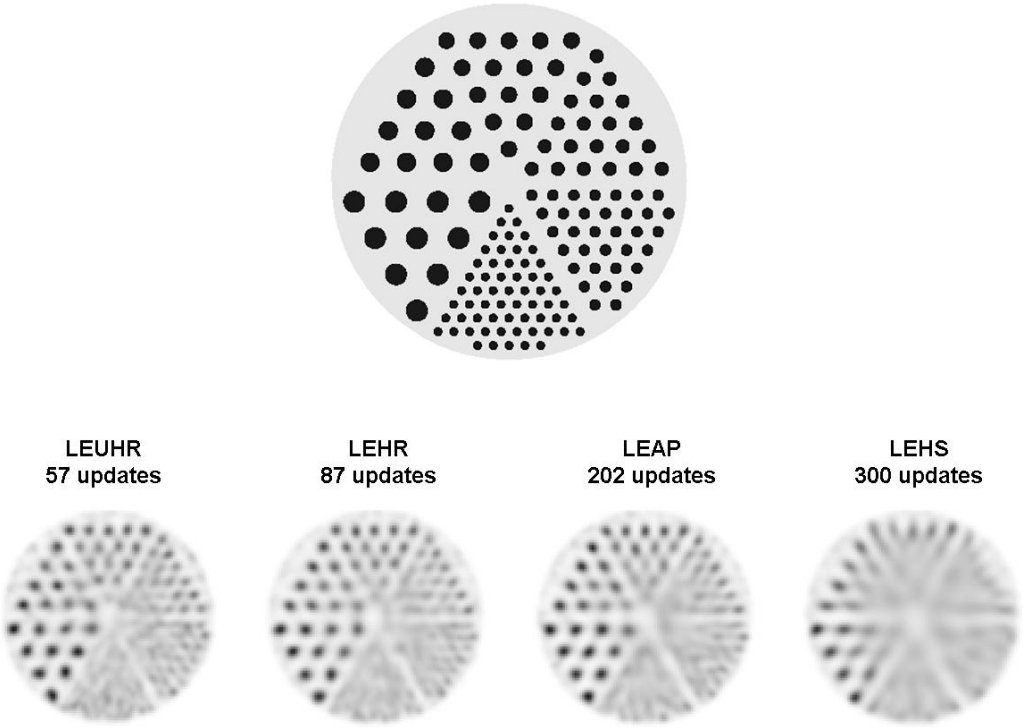

Figure 5.2: True image (top) and example reconstructed images after simulation of four different low energy collimators. Total counts are 15, 30, 45, and 150 million for LEUHR, LEHR, LEAP, and LEHS respectively. Reconstruction stopping criterion is the true object size of a 9.5 mm rod (3rd largest rods). For LEHS collimation the true object diameter was not reached after 300 updates.

the mean count density $\overline{d}$ in the reconstructed objects we define the emission recovery coefficient for a given object j and a given imaging parameter set i:

$$C_E(i,j) = \frac{\overline{d}(i,j)}{d_{True}(j)} , \tag{5.1}$$

where d_{True} is the true count density in the object. The boundaries of the target object to be measured are derived from the true high resolution.
In Figure 5.3 left we show the emission recovery for the 6 different rod sizes as a function of OSEM updates when using LEHR collimation. The comparison of the four different collimators is given in Figure 5.3 right. Mean values of 5 independent simulations with a pixel size of 2.4 mm and 10% background activity are shown. Total counts were 15, 30, 45, and 150 million for LEUHR, LEHR, LEAP, and LEHS respectively. For each rod size in Figure 5.3 right the reconstruction was stopped at the true object size values, respectively. The emission recovery values are normalized to the values of LEHR collimation.
The superiority in terms of emission recovery when using high resolution collimators at small structure sizes is obvious. High sensitivity collimation results in lower emission recovery values for all rod sizes tested.
In this initial assessment we observe in Figure 5.3 left that emission recovery is improved when using a higher number of updates. Yet, the noise level is expected to be higher. At these structure sizes and the system resolution of 9.6 mm (for LEHR collimation at 15 cm distance) the partial volume effect, which was not compensated in these cases, is a dominant factor. The superiority of small angle projection operators (i.e. with LEUHR collimation) for smaller structures at 30 million counts is not surprising. However, for further assessment we focus on LEHR collimation, since it is the most commonly used low energy collimator in clinical practice. Furthermore, we will investigate larger spherical structures (diameter > 9 mm) and different pixel sizes, count levels, and object positions.
We simulate hot spheres with diameters between 9.8 mm and 168 mm in a warm

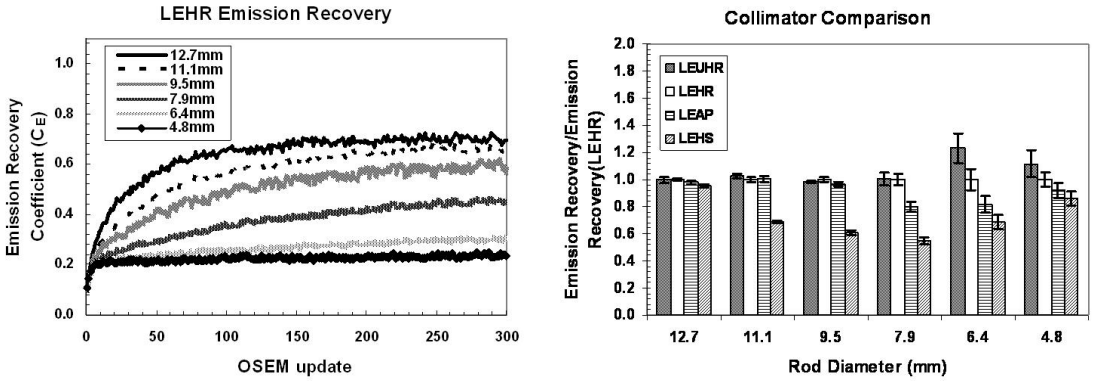

Figure 5.3: Comparison of four low energy collimators in terms of emission recovery when OSEM reconstruction was stopped at the true object size values respectively. 3D simulation of the Hot Rod Phantom with 10% background activity, 2.4mm pixel and 30×10^6 counts. Emission Recovery values are normalized to the LEHR results. Error bars shown are standard deviations (5 independent simulations for each data point).

cylindrical background with a diameter of 216 mm and height of 228 mm (sphere to background ratio 10:1). The dimensions of the small spheres are based on a standard quality control phantom (sphere inserts for Deluxe Jaszczak Phantom^{TM}, Data

Spectrum). We vary total counts between 0.125 and 32 million and reconstruction pixel size between 2.4 mm and 9.6 mm by rebinning the high resolution projection data. Figure 5.4 shows example images of simulated and reconstructed spheres.
Emission recovery is estimated according to Equation (5.1). As in the previous objects, the true boundaries are derived from the true high resolution images (Figure 5.4 top row). Partial volume effects, specifically spill-over at the object boundaries due to finite pixel size, are compensated by measuring the loss of emission in the simulation using different pixel sizes.

In Figure 5.5, A the loss of emission recovery due to spill over at the object bound-

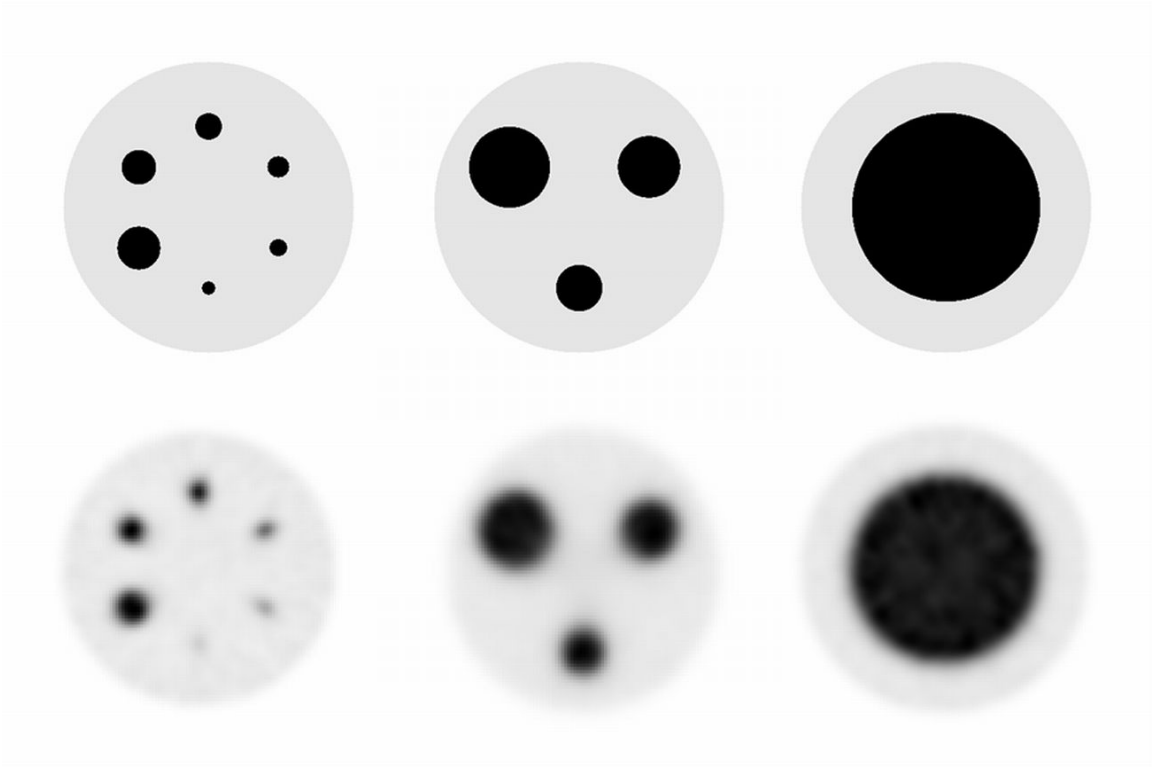

Figure 5.4: True (top row) and example reconstructed images (bottom row; LEHR collimation, 2.4 mm voxel, 32 OSEM updates) of the simulated spheres of different diameters in a 10% background.

aries is shown for the different object and voxel sizes used. The values are derived from simulations when a target to background ratio of 10:1 is assumed. Figure 5.5, B illustrates the effect when various sphere-to-background ratios are used. In this case we exemplarily show results for a 16 ml sphere (diameter: 31.3 mm). In subsequent simulations these results are used in a post-processing step after reconstruction to compensate for the spill-over effect by adding the respective values to the emission recovery coefficients measured in the simulations.

Figure 5.6, A and B show the emission recovery coefficients for different object sizes, number of OSEM updates, and voxel sizes used. Results are shown for LEHR collimation and 2 million total counts. No post-smoothing was applied after reconstruction. Each data point is the average value of 5 independently performed simulations. In general, the emission recovery coefficient is highly dependent on the number of OSEM

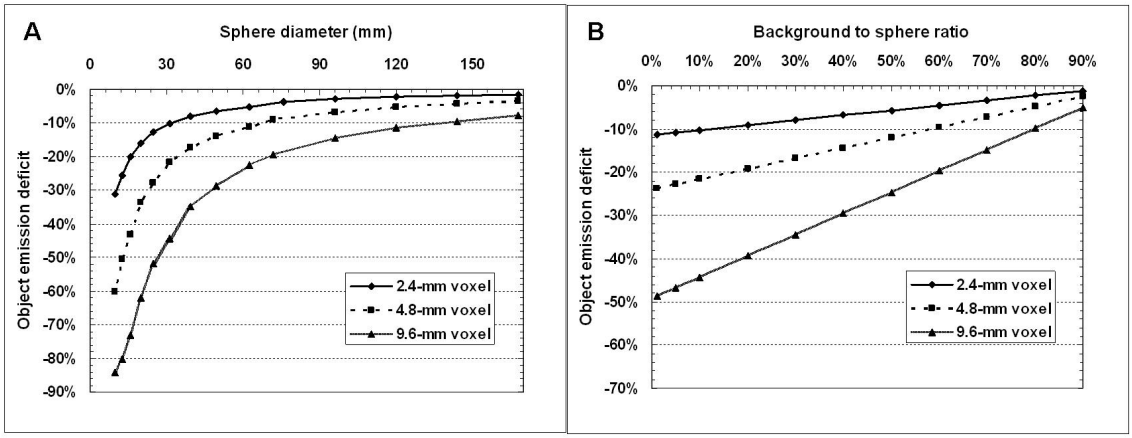

Figure 5.5: The effect of spill over at object boundaries on emission recovery due to finite voxel size for A: different object and voxel sizes with a target to background ratio of 10:1 and B: different target to background ratios using a 16 ml sphere.

updates especially for object sizes below 3 times the system resolution. In addition, it can be seen that the convergence rate in terms of emission recovery is slower for a smaller voxel size. The curves are steeper for 4.8 mm voxels than for 2.4 mm voxels, especially for low iteration numbers.
Figure 5.6, C describes the effect of the object position in the cylinder with 10% background on the emission recovery of a 16 ml sphere (object diameter: 31.3mm). The recovery coefficients e.g. for 32 updates vary between 0.80±0.01 for the center position and 0.89±0.01 for 92 mm off-center.
The dependency of total counts on the emission recovery is shown in Figure 5.6, D. Here we show results for 32 OSEM updates and a voxel size of 4.8 mm, since these are parameters which we use in the patient studies later on. Beyond 3 times the system resolution, the standard deviation of the recovery coefficient is below 0.0052 for all count levels tested. Below this point standard deviations are between 0.0065 for 16 ml spheres and 0.0462 for 0.5ml spheres. This result indicates that our recovery coefficients are unaffected by the count level.
To give a visual impression of the image behavior for different object sizes and reconstruction parameters, we show cross sections through reconstructed images of a hot sphere phantom in Figure 5.7. Sphere sizes are between 9.8 mm and 31.2 mm. The true image (top left) and reconstructed images with 10, 30, and 60 OSEM updates are shown. These images visually confirm the findings of Figure 5.6 A.
In summary, we observe significant variations of emission recovery with the number of OSEM updates and object size and position. We obtained emission recovery coefficients for imaging scenarios including parameters typical for the clinical operation range. We use these coefficients for the quantitative calibration method described in subsequent sections.

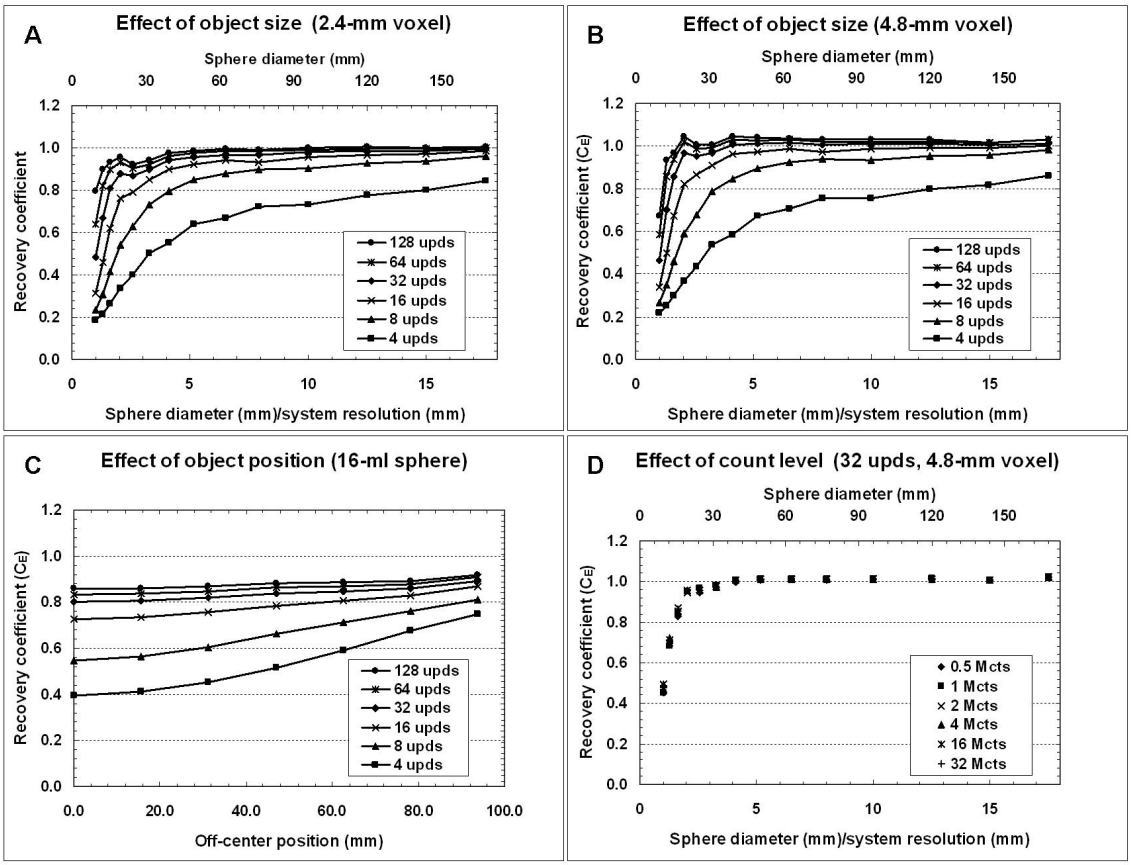

Figure 5.6: Emission recovery coefficients as a function of object size and number of OSEM updates for different voxel sizes using LEHR collimation and 2 million total counts (A and B), for different object positions of a 16 ml sphere (C), and for different total counts (D).

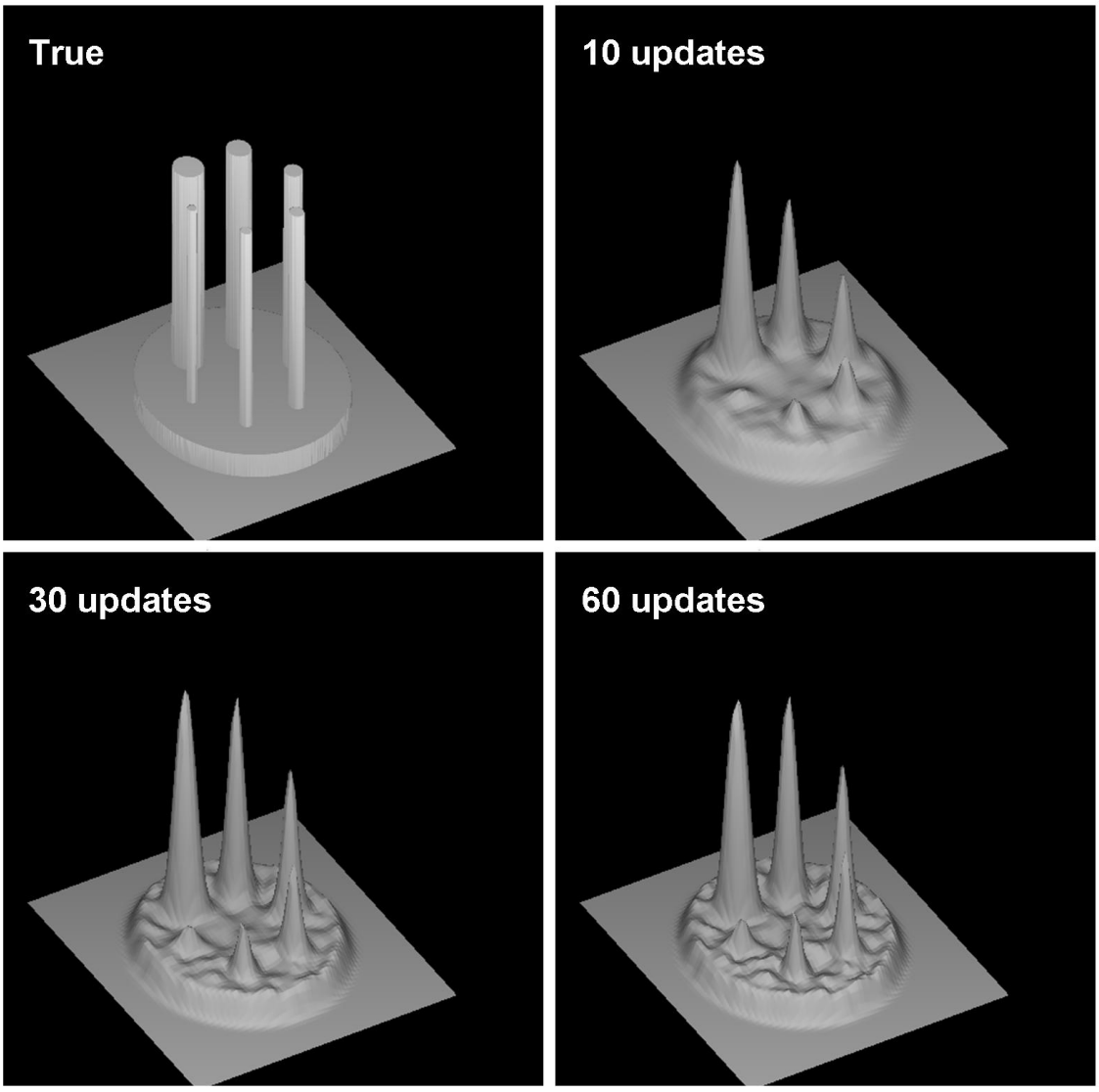

Figure 5.7: Cross sections through a reconstructed image of a hot sphere phantom.

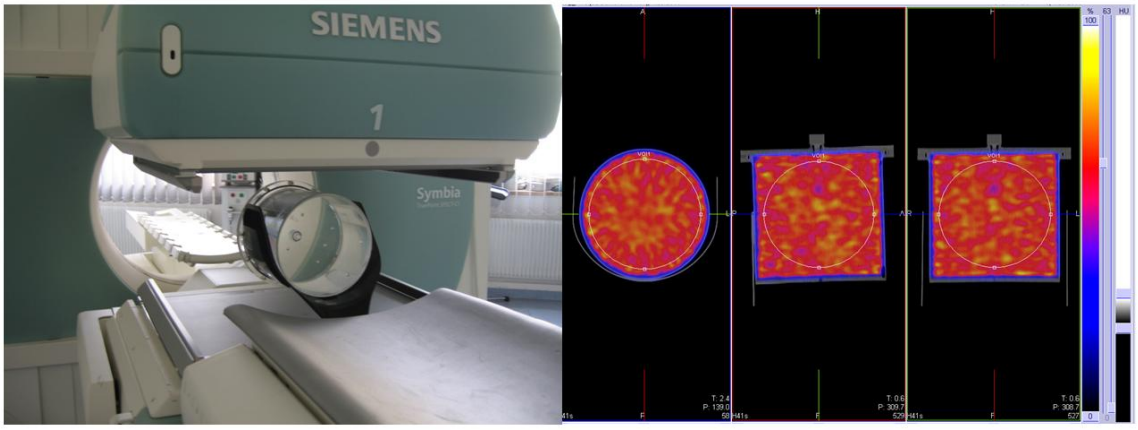

Figure 5.8: Left: Imaging setup for the cross-calibration using a large cylinder phantom. Right: Example reconstructed images with large volume of interest.

5.1.2 Step 2: Cross Calibration of the Imaging System

The cross calibration of the imaging systems serves as conversion from image counts to activity values. We cross-calibrate the clinical SPECT/CT system using a large cylindrical phantom (diameter: 216 mm, height: 186 mm) filled uniformly with a known activity concentration of Tc-99m measured in a well counter. The well counter is calibrated with a standard reference source (Cs-137). The measurement error for Tc-99m specified by the manufacturer is 5%. Approximately 50 million total counts are collected in a 360° acquisition range, 120 projections, and a 150 mm detector radius of rotation. Figure 5.8 left shows the imaging setup in a dual-headed SPECT/CT system. Two separate energy windows for the acquisition of the photo peak and the lower scatter are used. The window widths are both set to 15% as recommended by the manufacturer resulting in 108.5-129.5 keV for the lower scatter window and 129.5-150.5 keV for the photopeak window. An attenuation map is generated from a CT scan of the phantom using 130 kV, 30 mAs, and a smooth reconstruction kernel (B08s, Siemens Healthcare) with a value of the modulation transfer function (MTF) at 50% (ρ_{50}) of one line pair per centimeter (lp/cm). The reconstructed slice thickness is set to 5 mm. SPECT data is reconstructed using OSEM-3D with CT based attenuation correction and energy window based scatter correction. We use a modified triple-energy-window (TEW) method [52, 55] for scatter estimation with a 15% window for both photo peak and lower scatter, respectively. The scattered photons S_{pp} in the photopeak window are estimated as follows:

$$S_{pp} = \frac{w_{pp}}{2w_{ls}} P_{ls} \ , \tag{5.2}$$

where P_{ls} is the pixel intensity in the lower scatter window and w_{pp} and w_{ls} are the widths of the photopeak and lower scatter window, respectively (compare Equation (2.40)). In our case $w_{pp} = w_{ls} = 15\%$, thus a scaling factor of 0.5 is used. The scatter estimate is then included in the statistical model of the reconstruction by adding it to the projection estimate in the forward projection step (Equation (2.41), [64, 58]). The μ-values used for attenuation correction are determined by using piecewise linear

scaling from CT Hounsfield units (HU) to linear attenuation coefficients and converted from the effective CT energy to the energy of the radioisotope (Section 2.2.3, [29]). The attenuation correction is applied in the forward and backprojection within the reconstruction. Both scatter and attenuation correction methods are implemented in the commercial reconstruction software package (syngo MI applications 2009A, Siemens Healthcare).
To calculate the system volume sensitivity a large volume of interest (VOI) ($>$ 3000 ml, compare Figure 5.8 right) is drawn in the reconstructed image. We define the count rate within this VOI as:

$$R = (\sum_{j \in VOI} \hat{f}_j)/T_{dwell} \stackrel{def}{=} \hat{F}_{VOI}/T_{dwell} \ , \tag{5.3}$$

where $\hat{f}_j$ are the reconstructed counts in the jth voxel and T_{dwell} is the dwell time of the detector.
We correct for radioactive decay from the time of calibration T_{cal} to the start time of the acquisition T_0 using the decay factor $D(t)$:

$$D(t) = e^{-\lambda t} = e^{-\lambda(T_0 - T_{cal})} \ , \tag{5.4}$$

with the decay constant λ:

$$\lambda = \frac{\ln 2}{T_{1/2}} \ , \tag{5.5}$$

where $T_{1/2}$ is the half life of the isotope.
Since the time duration of the acquisition is not short in comparison to the half life of the isotope ($T_{1/2}$(Tc-99m)=361.2 minutes), we also correct for the radiocative decay that occurs during the acquisition. The number of recorded counts during the acquisition is proportional to the area a_d under the exponential decay curve from time T_0 to time $T_0 + \Delta t$, where Δt is the time duration of the acquisition (detector dwell time plus detector moving time). The effective decay factor $D_{eff}(t, \Delta t)$ is then the ratio of the area a_d and the area a_0, where a_0 corresponds to the counts that would be recorded in the absence of decay (constant count rate):

$$\begin{aligned} D_{eff}(t, \Delta t) \ = \ a_d/a_0 \ &= \ \left(\int_{T_0}^{T_0+\Delta t} e^{-\lambda t}\, dt \right) / \left(\int_{T_0}^{T_0+\Delta t} dt \right) \\ &= \left(\frac{1}{\lambda} e^{-\lambda T_0} - \frac{1}{\lambda} e^{-\lambda(T_0+\Delta t)} \right) / \Delta t \\ &= \left(\frac{1}{\lambda} e^{-\lambda T_0} - \frac{1}{\lambda} e^{-\lambda T_0} e^{-\lambda \Delta t} \right) / \Delta t \\ &= e^{-\lambda T_0} \left(1 - e^{-\lambda \Delta t}\right) / \lambda \Delta t \ . \end{aligned} \tag{5.6}$$

The decay corrected count rate $\hat{R}$ in the VOI is then [77]:

$$\hat{R} = R/D_{eff}(t, \Delta t) = R \ \cdot \ e^{\lambda T_0} \ \cdot \ \lambda \Delta t (1 - e^{-\lambda \Delta t})^{-1} \ . \tag{5.7}$$

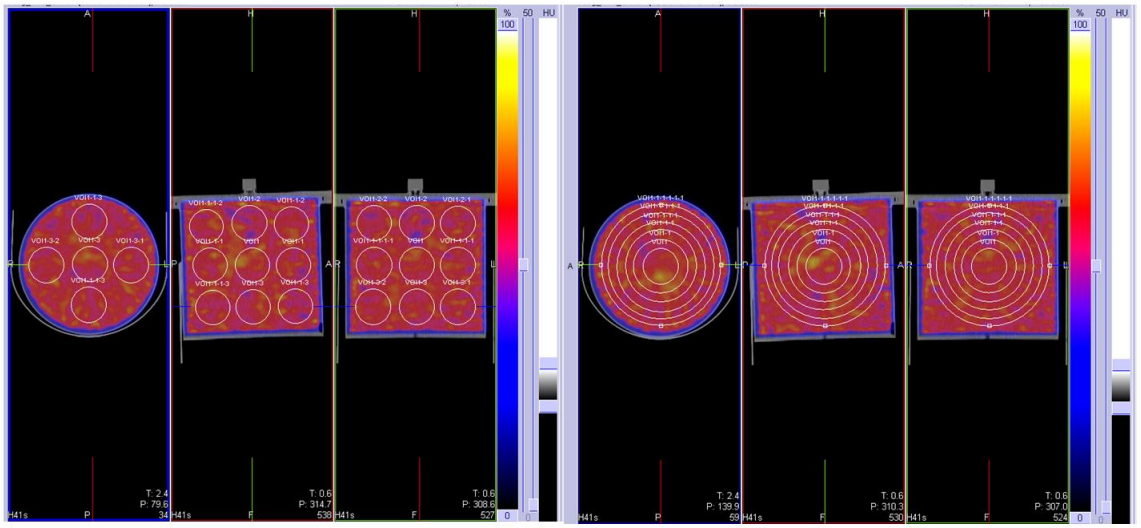

Figure 5.9: Different positions (left) and sizes (right) of volumes of interest used to assess variations of calculated system volume sensitivity values.

The second factor in Equation (5.7) corrects for the radioactive decay from the time of calibration to the start time of the acquisition (with $T_{cal} = 0$ assumed to be the starting point of time measurement, compare Equation (5.4)). The third factor corrects for the time duration of the acquisition.
Using the decay corrected count rate we define the system volume sensitivity as:

$$S_{Vol} = \frac{\hat{R}/V_{VOI}}{c_A} \ , \tag{5.8}$$

where V_{VOI} is the volume of the drawn VOI and c_A is the actual activity concentration in the phantom measured by the well counter. The unit of the system volume sensitivity is counts per minute per kilo Becquerel (cpm/kBq). The calculated value of S_{Vol} using the described imaging procedure and a large VOI is 10.29 cpm/kBq.
The variability of S_{Vol} is tested by drawing 15 small spherical VOIs (60 ml each), evenly distributed in the cylindrical volume, and calculating S_{Vol} for each small VOI. Similarly, different sized VOIs between 60 ml and 3000 ml are drawn. Figure 5.9 illustrates the positions and sizes of the VOIs. The calculated mean S_{Vol} for all VOIs is 10.28±0.24 cpm/kBq.

We briefly mentioned above that there is an error in the well counter measurement procedure which is specified to 5% by the manufacturer. At this point we will expand on this and calculate the impact of the errors caused by measurement instrumentation on the precision of our results.
When variables of a function are values of experimental measurements they have uncertainties due to measurement limitations (e.g. instrument precision) which propagate to the combination of variables in the function. Uncertainties can be defined as absolute errors Δx or relative errors $\Delta x/x$ in percent. The propagated uncer-

tainty Δf for a given function $f(x_1, x_2, \ldots, x_n)$ with the experimental measurements x_i (with $i = 1, 2, \ldots, n$) and absolute errors Δx_i can be estimated as [156, 157]:

$$\Delta f = \sqrt{\left(\frac{\partial f}{\partial x_1}\Delta x_1\right)^2 + \cdots + \left(\frac{\partial f}{\partial x_n}\Delta x_n\right)^2} \tag{5.9}$$

by using the following approximation which is derived from the Taylor series expansion around the point $f(x_1, x_2, \ldots, x_n)$:

$$\begin{aligned} &f(x_1 + \Delta x_1, x_2 + \Delta x_2, \ldots, x_n + \Delta x_n) \approx \\ &\approx f(x_1, x_2, \ldots, x_n) + \frac{\partial f}{\partial x_1}\Delta x_1 + \frac{\partial f}{\partial x_2}\Delta x_2 + \cdots + \frac{\partial f}{\partial x_n}\Delta x_n \end{aligned} \tag{5.10}$$

The precision of the system volume sensitivity is impacted by activity and volume measurement errors and statistical variations of measured counts. Here we treat the image counts $\hat{F}_{VOI}$ as Poisson distributed for the sake of convenience. Note that the data technically loose their Poisson characteristic due to processing during reconstruction.
According to Equation (5.9) the error for S_{Vol} is:

$$\begin{aligned} \Delta S_{Vol}^2 &= \left(\frac{\partial S_{Vol}}{\partial \hat{F}_{VOI}}\right)^2 \Delta \hat{F}_{VOI}^2 + \left(\frac{\partial S_{Vol}}{\partial c_A}\right)^2 \Delta c_A^2 \\ &= \left(\frac{1}{T_{dwell}\, V_{VOI}\, c_A}\right)^2 \Delta \hat{F}_{VOI}^2 + \left(-\frac{\hat{F}_{VOI}}{T_{dwell}\, V_{VOI}\, c_A^2}\right)^2 \Delta c_A^2 \ , \end{aligned} \tag{5.11}$$

with the error for the true activity concentration:

$$\begin{aligned} \Delta c_A^2 &= \left(\frac{\partial c_A}{\partial V}\right)^2 \Delta V^2 + \left(\frac{\partial c_A}{\partial A}\right)^2 \Delta A^2 \\ &= \left(-\frac{A}{V^2}\right)^2 \Delta V^2 + \left(\frac{1}{V}\right)^2 \Delta A^2 \ , \end{aligned} \tag{5.12}$$

where V is the volume measured with a measurement cylinder with an imprecision $\Delta V/V$ of 0.4% and A is the activity measured in the well counter with $\Delta A/A = 5\%$. Using Equation (5.11) and taking into account the variations for multiple VOIs, the propagated relative standard error (RSE) of the system volume sensitivity ΔS_{Vol} is 6.5%.

5.1.3 Step 3: Application of Corrections to Reconstructed Image Data

The calibration method was verified by using a standard quality control sphere phantom (Flangeless Deluxe Jaszczak Phantom™, Hollow Sphere Set (6)™, Data Spectrum). The measured activity concentration according to the calibrated well counter

was 729 kBq/ml in the spheres and 64 kBq/ml in the background, resulting in an activity concentration ratio of 11.5:1. The activity dilution for the spheres was prepared using a calibrated pipette (Eppendorf Research®) with 0.6% imprecision as specified by the manufacturer. The total activity in the phantom at the time of acquisition was 427.7 MBq. Data with the phantom in the center of the field of view was acquired by using a 150 mm detector radius of rotation over a 360° scan range and 120 projections with a dwell time of 15 seconds each. LEHR collimation with a 4.8 mm pixel size was used and approximately 24 million total counts were acquired. For attenuation correction a CT acquisition of the phantom was performed using 130kV, 30 mAs, and a smooth (B08s, Siemens Healthcare) and medium reconstruction kernel (B40s, Siemens Healthcare) with $\delta_{50} = 4.5$ lp/cm. The reconstructed slice thickness was set to 3 mm.

The SPECT data was reconstructed with OSEM-3D with scatter and CT based attenuation correction, as described earlier. Spherical VOIs were manually drawn by following the CT boundaries of the fused SPECT/CT image (see Figure 5.10). The VOIs were shifted by 2.4 mm (0.5 times voxel size) in negative and positive x, y, and z direction and the average of the total counts in the VOIs were calculated. This procedure was done to minimize biases introduced by the initial positioning of the VOI by hand as well as by residual mis-registration of SPECT and CT images.

We calculate the absolute activity concentration for a given object size j using the following formula:

$$\hat{c}_A(j) = \frac{\hat{R}(j)/V_{VOI}}{S_{Vol}\, C_E(j, i')}\ , \tag{5.13}$$

with i' being the specific imaging parameter set used (4.8 mm pixel, 32 OSEM updates, LEHR collimation).

The absolute activity concentrations $\hat{c}_A$ for all 6 spheres are calculated by applying Equation (5.13) using recovery coefficients between 0.291 and 0.801 for the smallest and the largest sphere, respectively. Starting with measurement errors of 5% for the well counter and 0.6% for the pipette, we propagate the errors and estimate measurement errors for each of the variables in Equation (5.13) and ultimately for $\hat{c}_A$. The propagated error for the estimated activity concentration is:

$$\begin{aligned}
\Delta\hat{c}_A^2 &= \left(\frac{\partial\hat{c}_A}{\partial\hat{F}_{VOI}}\right)^2 \Delta\hat{F}_{VOI}^2 + \left(\frac{\partial\hat{c}_A}{\partial V_{VOI}}\right)^2 \Delta V_{VOI}^2 + \\
&\quad + \left(\frac{\partial\hat{c}_A}{\partial S_{Vol}}\right)^2 \Delta S_{Vol}^2 + \left(\frac{\partial\hat{c}_A}{\partial C_E}\right)^2 \Delta C_E^2 \\
&= \left(\frac{1}{T_D\, V_{VOI}\, S_{Vol}\, C_E}\right)^2 \Delta\hat{F}_{VOI}^2 + \left(-\frac{\hat{F}_{VOI}}{T_D\, V_{VOI}^2\, S_{Vol}\, C_E}\right)^2 \Delta V_{VOI}^2 + \\
&\quad + \left(-\frac{\hat{F}_{VOI}}{T_D\, V_{VOI}\, S_{Vol}^2\, C_E}\right)^2 \Delta S_{Vol}^2 + \left(-\frac{\hat{F}_{VOI}}{T_D\, V_{VOI}\, S_{Vol}\, C_E^2}\right)^2 \Delta C_E^2
\end{aligned} \tag{5.14}$$

The results for the phantom experiment are summarized in Table 5.2 showing the true and the calculated activity concentrations, the applied volume sensitivity and

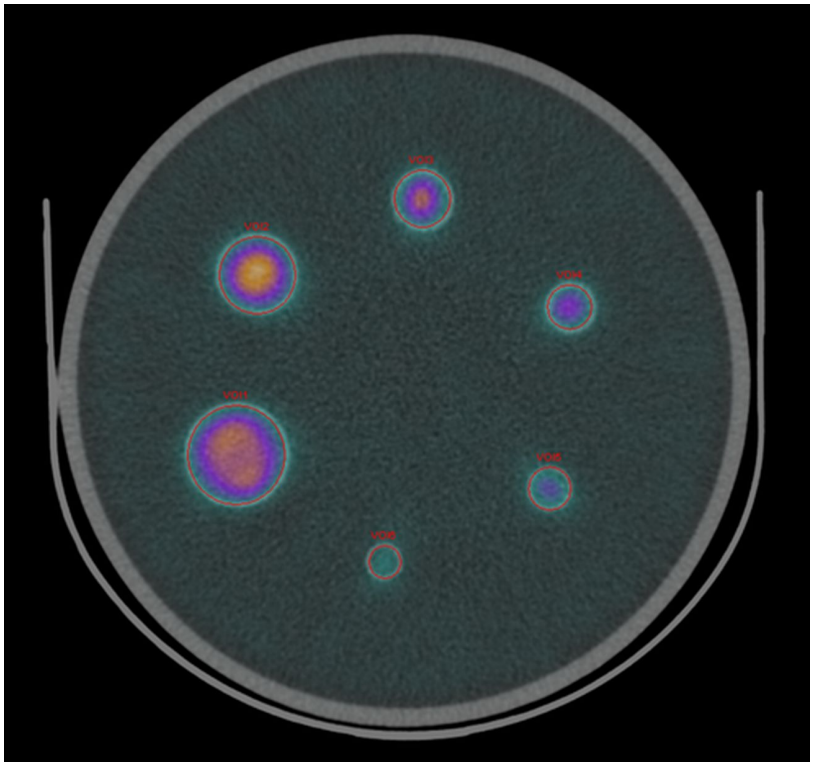

Figure 5.10: Reconstructed image of the sphere phantom fused with the CT image (LEHR collimation, 4.8 mm voxel, 32 OSEM updates). Circular volumes of interest were drawn manually using the CT boundaries as reference.

True Sphere Volume (ml)	V_{VOI} (ml)	C_E	$\hat{c}_A$ (kBq/ml)	$\delta_{c_A}(\%)$	$\Delta\delta_{c_A}/\delta_{c_A}(\%)$
16	15.97 (0.1%)	0.8 (0.1%)	708.3 (6.5%)	-2.8	8.0
8	8.02 (0.1%)	0.74 (0.1%)	749.4 (6.5%)	+2.8	8.5
4	3.94 (0.6%)	0.71 (0.2%)	684.0 (6.6%)	-6.2	7.7
2	2.08 (1.0%)	0.61 (0.6%)	685.3 (6.8%)	-6.0	7.9
1	0.98 (0.8%)	0.42 (0.8%)	679.7 (6.7%)	-6.8	7.8
0.5	0.52 (1.6%)	0.29 (1.4%)	708.8 (7.1%)	-2.8	8.4

Table 5.2: Quantitative results for the phantom experiment.

recovery coefficients, and the VOI volumes. Propagated relative standard errors (RSE) are given in brackets. The relative difference between true and calculated activity concentration δ_{c_A} is determined by:

$$\delta_{c_A} = \frac{\hat{c}_A - c_A}{c_A} \tag{5.15}$$

and the corresponding error is:

$$\Delta\delta^2_{c_A} = \left(\frac{1}{c_A}\right)^2 \Delta\hat{c}^2_A + \left(-\frac{\hat{c}_A}{c^2_A}\right)^2 \Delta c^2_A \tag{5.16}$$

The average difference between true and calculated activity concentration for the phantom experiment is -3.6% with an average RSE of 8.0%. Assuming a Gaussian behavior this would result in a 95% confidence interval for the quantitative accuracy between -19.4% and +12.2%.

5.2 Quantitative Accuracy of In-vivo 3D SPECT

5.2.1 Patient Studies

After the validation with phantom experiments, we test the developed calibration method in-vivo in patient studies.
Permission to perform studies in patients was granted by the Ethical Committee of the University of Erlangen-Nuremberg. Image data-sets from 16 patients were acquired undergoing Tc-99m-diphosponate (DPD) bone examinations of the pelvis for clinical reasons. A bone SPECT/CT imaging protocol according to Table 2.2 was used. Injected dose was between 7-10 MBq/kg body weight Tc-99m-DPD. SPECT/CT acquisitions were performed 3-4 hours after intravenous injection. The acquisition protocol employed LEHR collimation, a matrix size of 128×128, 4.8 mm pixels and a total of 120 projections, each with a dwell time of 15 seconds, over 360°. The total number of counts was between 2.9 and 8.5 million for the 16 patients examined. A low-dose CT with 130 kV, 30 mAs using adaptive dose modulation (CARE Dose 4D, Siemens Healthcare) was performed subsequently to the SPECT acquisition. The CT reconstruction used a smooth and a medium kernel (B08s, B40s, Siemens Healthcare) with 5 mm and 1 mm reconstruction increments, respectively.
After creation of the CT derived attenuation map the SPECT data of the 16 patients was reconstructed using OSEM-3D with scatter and CT based attenuation correction using 4 subsets and 8 iterations. No post-smoothing was applied to the reconstructed images.
The patients' urine was collected after the examination and measured in a well counter (see Figure 5.11 bottom). For this, three test-tubes were filled independently with a pipette (1 ml each) and the average, decay corrected activity concentration values served as gold standard c_A.
Volumes of interest were drawn in the reconstructed image by manually adjusting the threshold of an isocontour such that the VOI boundaries coincided with the bladder boundaries of the fused CT image. The values for the threshold resulted in between 20% and 25% of the maximum voxel value of the respective VOI. Similar values were reported by Shcherbinin et al. [88] to most accurately represent the true volume of a given object. The VOI volumes varied between 40.7 ml and 482.0 ml. Figure 5.11 top shows fused images of two representative patients and the respective VOIs. Absolute activity concentrations $\hat{c}_A$ were calculated according to Equation 5.13 using the emission recovery coefficient C_E at the particular operation point (volume and imaging parameters).
Since one cannot assume a constant activity concentration in the bladder during the acquisition and until the time of urine collection, the concentration change rate was estimated by measuring the mean count density in the bladder in the first and last 2D frame of the projection data set. The difference in the angular position of the two frames was 3°. Isocontours with a 50% threshold were drawn in both frames and the decay corrected count density was calculated in the regions of interest. Using the difference in the count density of the two frames, a linear curve was extrapolated beyond the end point of the acquisition till the time of urine collection.
The mean activity concentration change rate of the urine during the acquisition was 0.5% per minute. The average time from the end of the acquisition till the urine

collection was 8.8 minutes resulting in a correction factor for the reconstructed counts of 4.3%.
Table 5.3 summarizes the results from the patient experiments. The mean deviation of the calculated activity concentrations from the gold standard values is +1.1% with an average RSE of 8.4%. The lower and upper boundaries of a 95% confidence interval are -15.4% and +17.5%. The target volumes and activity concentrations are between 40.7 ml and 482.0 ml and 13.6 kBq/ml and 284.1 kBq/ml. Mean quantification accuracy within 10% could be achieved in 13 out of 16 patients.

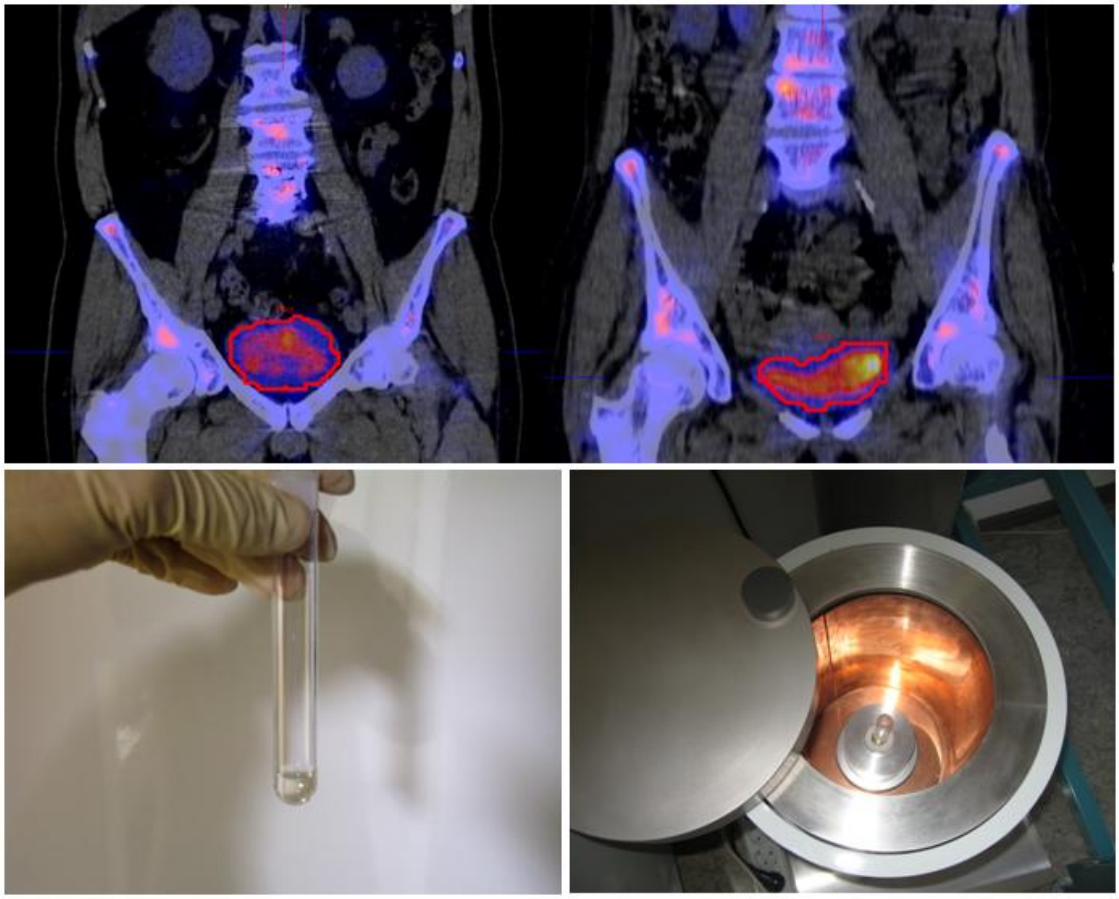

Figure 5.11: Reconstructed images of two representative patients fused with the CT images (LEHR collimation, 4.8 mm voxel, 32 OSEM updates). Volumes of interest are drawn by setting the threshold of an isocontour to coincide as close as possible with the CT boundaries.

Patient	V_{VOI} (ml)	Urine activity concentration c_A (kBq/ml)	$\hat{c}_A$ (kBq/ml)	δ_{c_A} (%)	$\Delta\delta_{c_A}/\delta_{c_A}$
1	380.4	24.5	24.6	0.4%	8.3%
2	479.4	30.6	32.0	4.7%	8.4%
3	244.6	45.0	45.8	1.8%	8.2%
4	40.7	144.3	168.7	16.9%	12.4%
5	166.4	46.5	43.1	-7.4%	7.3%
6	309.1	13.6	13.8	1.4%	8.0%
7	114.4	27.3	25.4	-6.8%	7.3%
8	128.0	41.7	48.6	16.6%	8.8%
9	204.3	73.5	68.0	-7.5%	8.0%
10	273.0	17.5	20.0	14.3%	10.3%
11	157.2	16.7	16.9	1.0%	8.5%
12	53.0	284.1	272.9	-3.9%	9.0%
13	482.0	34.6	32.9	-4.9%	7.3%
14	420.1	94.2	86.8	-7.8%	7.1%
15	282.8	75.1	77.5	3.1%	8.1%
16	246.8	138.4	131.3	-5.2%	7.4%
Min	**40.7**	**13.6**	**13.8**	**-7.8%**	**7.1%**
Max	**482.0**	**284.1**	**272.9**	**16.9%**	**12.4%**
Average	**248.9**	**69.2**	**69.3**	**1.1%**	**8.4%**

Table 5.3: Quantitative accuracy and accumulated errors for the patient experiments

5.2.2 Summary - 3D Quantitative SPECT

Using the developed calibration method, the average quantitative accuracy is within 3.6% in phantoms with different sized spheres when using Tc-99m. These results reproduce the accuracy reported by Vandervoort et al. [84], Willowson et al. [86], and Shcherbinin et al. [88] (compare Section 2.4). We show, in addition, that this accuracy can be achieved independently of target volume when the appropriate correction factors are used. It turns out that these correction factors not only depend on object size but also on position and, more importantly, on the number of OSEM updates. Little comment was made on this non-stationary behavior in previous work, although we believe that this represents a major challenge for quantification using OSEM.
We estimated the precision of our experiments by taking errors into account which are unavoidable and caused by processes like activity and volume measurement, drawing of VOIs, and also by image statistics. Considering the various sources of error we obtain an average accumulated error of 8.0% in our phantom experiment resulting in a 95% confidence interval between -19.4% and +12.2%. This confidence interval outlines realistic uncertainty boundaries when operating in a clinical setup.
In-vivo results show an average accuracy within 1.1% with an average precision of 8.4%, similar to the phantom experiment. The accuracy in patient studies ranges from -7.8% to +16.9% resulting in a standard deviation of 8.5% compared to 3.6% in the phantom experiment. We relate the larger variation in the patient study to procedures and assumptions during our calibration method:

1. We assumed a linear extrapolation with a slope derived from projection data to account for metabolic function. This linear extrapolation of activity concentration change rates is an assumption and might not represent the truth in all the cases. In general, one should assume that the activity change rate of the urine is highly varying from patient to patient and justifies a validation in its own right. We chose the simplest approach of linear extrapolation. Due to the rather short time between acquisition and urine collection the correction factor that was applied to the reconstructed counts was on average 4.3%. One could argue that this is a minor change and still in the range of our uncertainties of 8%. Not applying this correction would result in a different bias and shift the confidence interval by 4.3%.

2. The VOIs in the SPECT images were determined by drawing an isocontour which best represented the object boundaries in the fused CT image. This is not a trivial task especially if other high uptake regions are close to the target.

3. The method used to simulate the imaging system only takes the primary photons of 140 keV into account, neglecting septal penetration and assuming perfect scatter rejection. Object and collimator scatter is present in the acquired data and corrected using TEW-based scatter estimates included in the iterative reconstruction. The TEW method for scatter correction is easy to implement and proved to give accurate scatter estimates in phantoms [55, 54]. Narita et al. [54] showed that this method introduces an overall bias of 4% for absolute quantification. We should point out that we indirectly accounted for biases caused by the scatter

correction technique, since scatter correction is applied both in the cross calibration step as well as the actual measurements. Note, however, that the imaging setup was slightly different and the scatter response is different in patients than in phantoms.

Despite various inconsistencies, the developed calibration procedure shows encouraging results for the accuracy of absolute quantification in SPECT when using Tc-99m in combination with OSEM-3D reconstruction in phantoms and also in patients. Our results for the propagated measurement errors show that the real challenge for quantitative SPECT in a clinical setup is to improve the precision, that is, to reduce the error bars. The lower bound of the precision is given by the measurement tools available at the clinical site and may rarely be below 5%.

5.3 Quantitative Accuracy of dynamic SPECT

We presented a calibration technique for quantitative SPECT which delivered good accuracy in 3D static SPECT imaging. We proceed with applying the method to dynamic SPECT imaging. We investigate the accuracy of time-activity measurements when slow-rotating dual-headed gamma camera systems in combination with co-registered CT images and OSEM-3D with scatter and attenuation correction are used. The goal is to demonstrate the potential and the limitations of a clinical dual-headed SPECT/CT system for quantitative tomographic imaging of dynamic processes using multiple time-contiguous 3D acquisitions with 3D iterative reconstruction.
We first use simulations of a SPECT/CT system to estimate absolute quantification errors in time-activity measurements. We systematically assess dependencies of these errors on signal to noise ratio and sampling frequencies using a MAG-3 renal time-activity profile.
In addition, a physical phantom is developed to measure dynamic processes on a clinical SPECT/CT system. We set a baseline for dual-headed SPECT systems by evaluating different activity change rates in the phantom and varying sampling frequencies of the imaging system.

5.3.1 Dynamic SPECT simulations

Simulations are used to estimate the emission recovery coefficients for various imaging parameter settings of time-contiguous SPECT acquisitions. We use the quasi-analytical method which we described earlier (Section 5.1.1) and employ LEHR collimation. As before, a μ-map is used for attenuation correction and perfect scatter rejection of 140keV (Tc-99m) photons is assumed.
Projections of a phantom with six spheres of varying diameters between 9.9 and 31.2 mm (Jaszczak Deluxe, Data Spectrum, Hillsborough, NC, USA) are generated. The activity concentration in the spheres changes over time according to a three-phase renal time-activity function with peak activity after four minutes. Figure 5.12 shows the image model of the sphere phantom (left) and the time-activity profile with the three renal phases (right). The phases model the perfusion phase (I), secretion phase (II), and excretion phase (III) [98]. The simulated SPECT acquisition uses 60 views in a 180° rotation of two detectors (total angular range: 360°, total number of views: 120). Signal to noise ratio and SPECT rotation times are varied between 8×10^3 and 128×10^3 total peak counts and 7.5 seconds to 120 seconds per 180° rotation, respectively. Five independent realizations are generated for each parameter setting. OSEM-3D with attenuation correction is used for reconstruction of the images.
Figure 5.13 shows examples of reconstructed images from simulations using the time-activity profile in Figure 5.12. In this example a maximum activity concentration of 3 kBq/ml at the peak of the time activity curve is used. We use a background activity concentration of 10% of the peak value in the target object.
Figure 5.14 left shows the mean emission recovery coefficients for the different object sizes in the simulated phantom and different sampling frequencies. 16 iterations and 2 subsets were used for reconstruction without post-smoothing. Values are averaged over all time-contiguous acquisitions in a particular time-activity measurement. Fig-

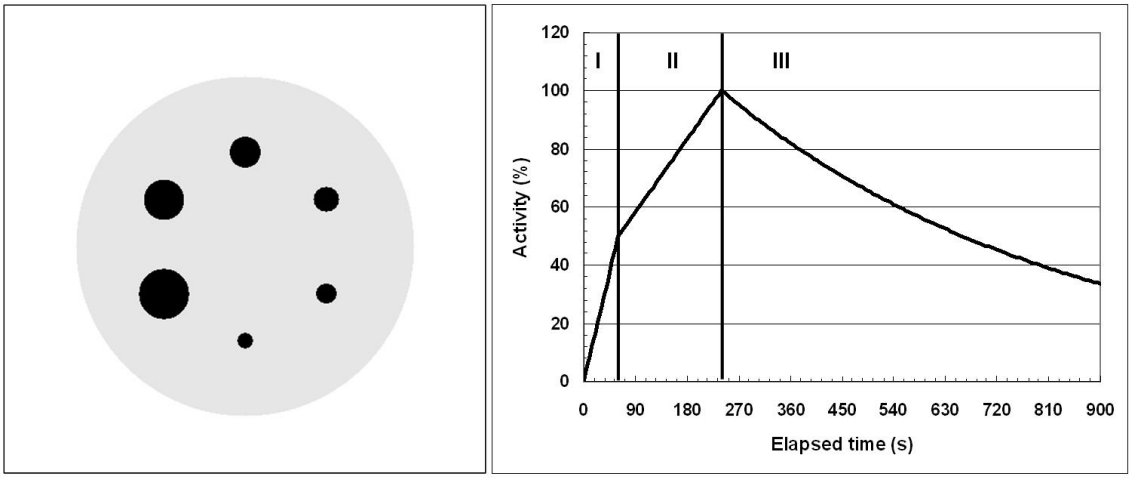

Figure 5.12: Image model (left) and time-activity profile (right) used for simulation of renal clearance. Three phases are modeled: Perfusion phase (I), secretion phase (II), and excretion phase (III).

ure 5.14 right gives the corresponding standard errors.
Results from simulations indicate robust behavior of the emission recovery for the six tested object sizes against changes in sampling frequencies and noise levels. The standard error of the recovery coefficients decreases with larger object size and is below 5% for objects whose volume exceeds 4 ml. Note that for image evaluation the object boundaries need to be known precisely to draw correct regions of interest. We notice from the images in Figure 5.13 that it is a challenging task to draw correct object boundaries based on nuclear images only, especially for small objects and low count levels. In practice, this postulates co-registered SPECT/CT images.

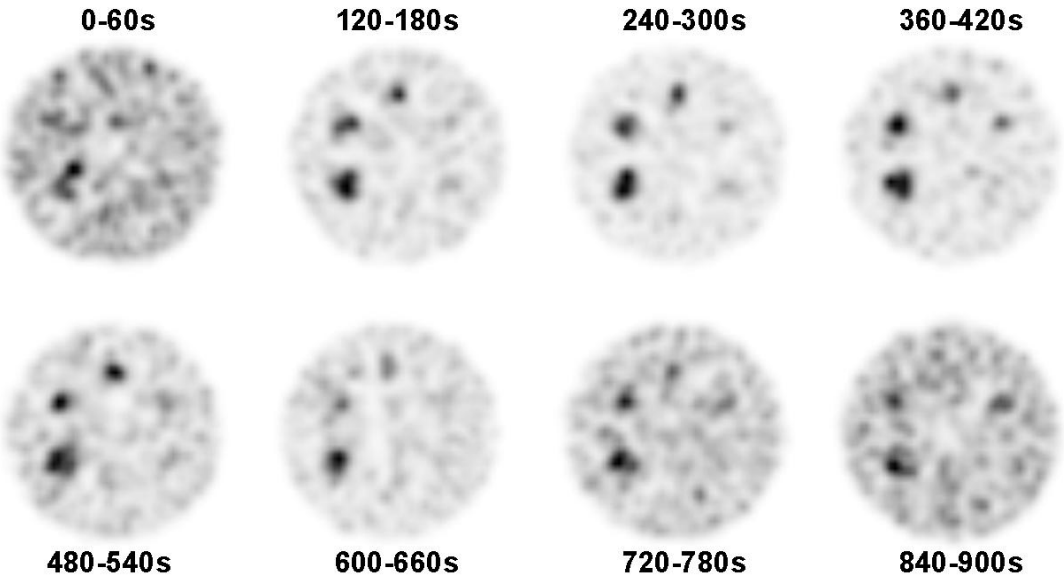

Figure 5.13: Example reconstructed images of the simulated sphere phantom. Every second time frame is shown. Peak total counts per time frame are 64×10^3.

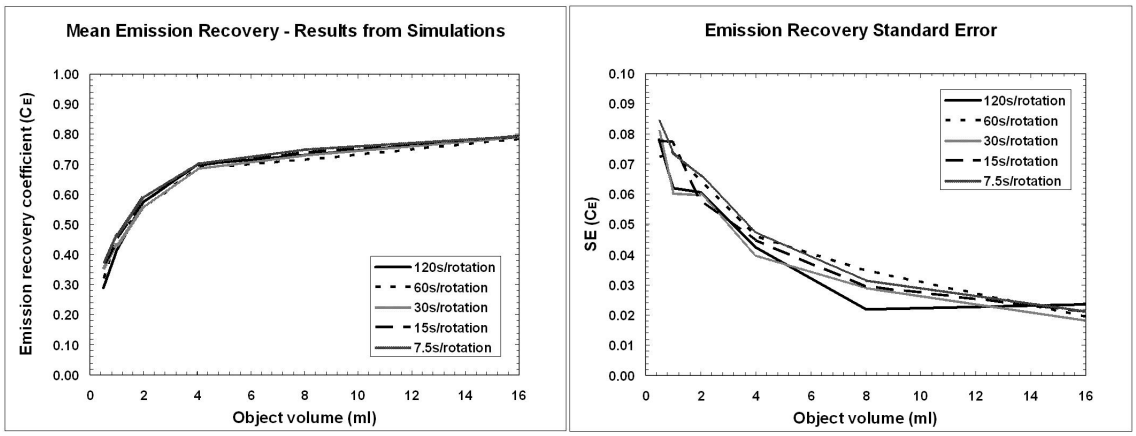

Figure 5.14: Left: Simulation results for the mean emission recovery coefficients for different object sizes and sampling frequencies. Right: Corresponding standard errors of the mean emission recovery coefficients. 32 OSEM updates were used for reconstruction.

5.3.2 Dynamic Phantom Experiments

In addition to simulations, a physical phantom is developed which allows the assessment of dynamic processes with a clinical SPECT/CT system. The phantom consists of a cylindrical chamber (45.5 ml) with input and output tubing, connected to a programmable peristaltic pump (Cavro Scientific Instruments, Sunnyvale, CA, USA). The diameter of the tubing is 1.6 mm and the maximum rotational speed of the pump is 7.25 revolutions per second (RPS) resulting in a maximum flow rate of $1.5ml/s$. The chamber is placed in a large water cylinder for imaging. Two reservoirs containing an activity dilution of Tc-99m for wash-in and fresh water for wash-out, respectively, are prepared. Figure 5.15 shows the setup of the pump and the cylindrical chamber with input and output tubing (left) and the imaging setup in the SPECT/CT system (right).

We acquire dynamic image sequences by performing time-contiguous SPECT acqui-

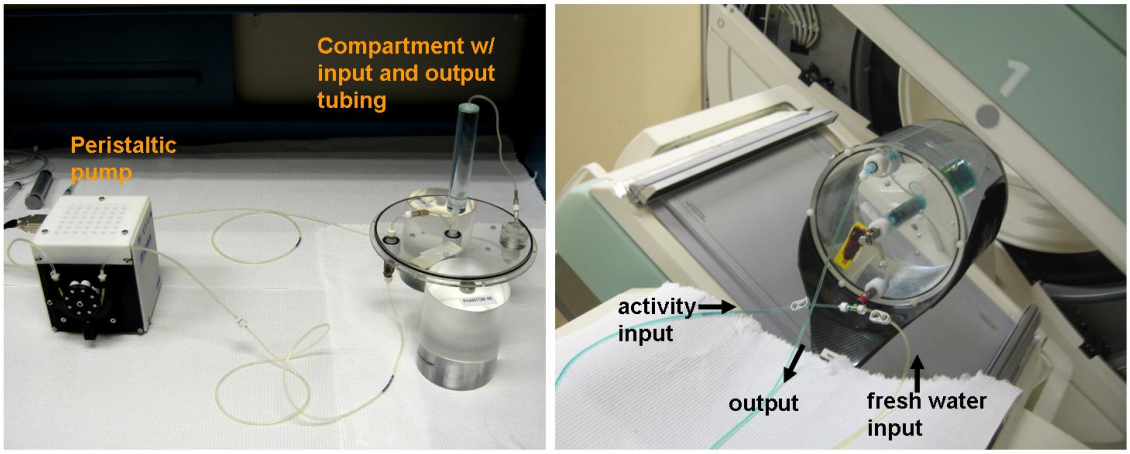

Figure 5.15: Left: Physical phantom for modeling dynamic processes. A cylindrical compartment is connected to a programmable peristaltic pump. Right: Setup of the dynamic phantom in the dual headed SPECT/CT imaging system.

sitions using a dual-headed SPECT/CT system (Symbia-T2, Siemens Healthcare). A full SPECT 360° data set is obtained by rotating the dual-headed system by 180°. Due to a finite gantry rotation range, the rotational direction of the gantry is alternated after each 180° acquisition. The maximum imaging speed of the system in continuous mode is $18°/s$ which results in a minimum total imaging time of 10 seconds for a full SPECT projection data set (180° rotation). Additional time in between the contiguous acquisitions is spent for acceleration and deceleration. The amount of this imaging dead time varies between 1 second and 5.7 seconds depending on the final imaging speed.

For the dynamic phantom experiments, we vary the imaging time between 10 seconds and 60 seconds for a single SPECT image. The flow rate of the pump is varied between 0.2 ml/s and 1.5 ml/s. The time activity curve peaks once the entire chamber volume is replaced by the input activity dilution. For a flow rate of 0.2 ml/s, this peak activity is obtained after 240 seconds, which is typical for a renal time activity function [98]. In addition to a renal TAC, we test dynamic processes with peak times

T_P of 120, 60, and 30 seconds.
The surrounding water cylinder of the phantom is filled with Tc-99m such that the peak activity to background ratio is 10:1.
For attenuation correction, a CT acquisition of the phantom is performed using 130kV, 30 mAs x-rays, and a smooth reconstruction kernel (B08s, Siemens Healthcare, Germany) with a 3 mm reconstruction increment. Images are reconstructed with OSEM-3D with corrections for scatter (TEW) and attenuation. We use 16 iterations and 2 subsets without post-smoothing. Figure 5.16 shows a reconstructed image of the phantom at peak time fused with the co-registered CT image.
Quantitative evaluation is done by first drawing a VOI in the reconstructed image using the boundaries of the registered CT image. The absolute activity concentration $\hat{c}_A$ is then calculated by using Equation (5.13).

Figures 5.17 to 5.20 show the results of the phantom experiments for the four different TACs with peak times T_P of 240 seconds (Figure 5.17), 120 seconds (Figure 5.18), 60 seconds (Figure 5.19), and 30 seconds (Figure 5.20). For each TAC the true and calculated activity concentration for rotation times of 10, 15, 30, and 60 seconds are shown. Error bars indicate the accumulated uncertainties due to measurement instrumentation such as well counter and pipette. Errors are propagated through all calibration steps (Equation (5.11) and (5.14)). The gaps between the columns indicate acceleration and deceleration times of the imaging system in which no image data is taken. These times increase with detector rotation speed.

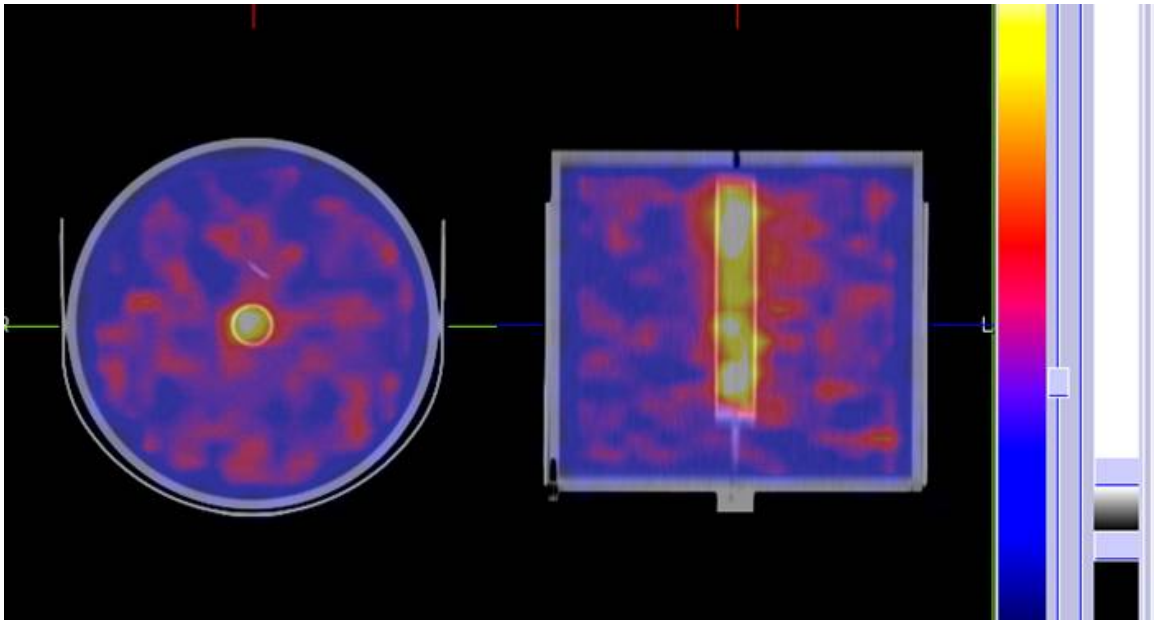

Figure 5.16: Reconstructed image of the phantom fused with the co-registered CT image.

We observe that the individual SPECT images (the columns in Figures 5.17 to 5.20) represent the true activity concentration accurately at the discrete point in time where they were taken. This is true for all time-activity profiles and sampling frequencies. Table 5.4 provides the detailed results including the mean accuracy δ_{c_A} for each imaging setup (averaged over all time-contiguous volumes in a TAC measure-

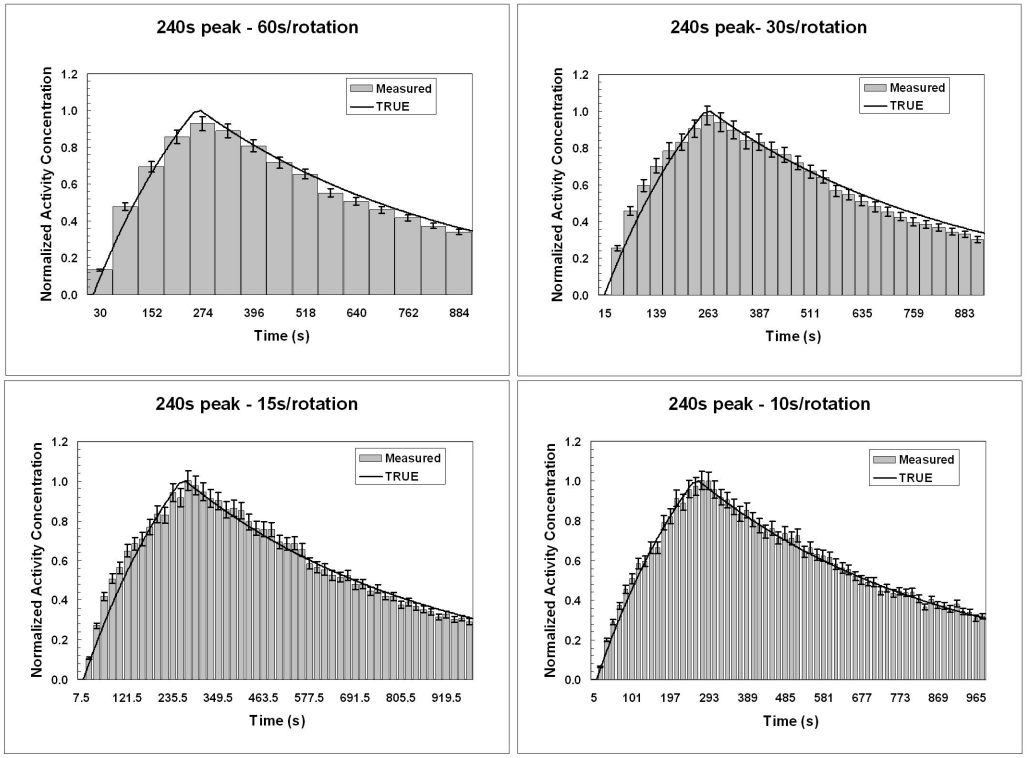

Figure 5.17: True and calculated activity concentration for a TAC with a $T_P = 240s$ imaged with sampling frequencies of 60, 30, 15, and 10 seconds per rotation.

ment) and the mean RSE $\Delta\delta_{c_A}/\delta_{c_A}$ due to measurement instrumentation. The mean accuracy is within 0.4% ($T_P = 240s$) and 8.8% ($T_P = 30s$). The average accumulated uncertainties due to measurement instrumentation are between 6.1% and 8.2%.
Table 5.4 also shows the estimation errors of the area under the time activity curve (AUC) and the accuracy to which the peak time and the time of 50% washout ($T_{1/2}$) are estimated. These parameters are typically used for diagnostic interpretation of TACs e.g. for renal function [98].
The area under the time-activity curve is estimated within an accuracy of 8.2% for processes with peak times of 240, 120, and 60 seconds and within 13.1% for the fastest process tested ($T_P = 30s$).
For slow processes (T_P: 240s, 120s), the peak time and $T_{1/2}$ are estimated within an accuracy of 10% for all different sampling frequencies with improved accuracy when denser time sampling is used (10 and 15 seconds per image). For faster processes, these parameters cannot be estimated accurately when using imaging times of 30 and 60 seconds per volume. This is confirmed by Figures 5.19 and 5.20. For $T_P = 30s$ and an imaging time of 60 seconds, the shape of the TAC cannot be reproduced. Figure 5.20 also visualizes the increased impact of the detector dead time due to acceleration and deceleration on fast time-activity processes.

TAC Peak Time (s)	Rotation Time (s)	Mean δ_{c_A} (%)	Mean $\Delta\delta_{c_A}/\delta_{c_A}$ (%)	AUC Estimation Error (%)	Peak Time Estimation Error (%)	$T_{1/2}$ Estimation Error (%)
240s	10s	6.0%	7.2%	7.7%	3.0%	1.7%
	15s	2.7%	7.3%	8.2%	1.7%	2.1%
	30s	0.8%	7.2%	4.3%	2.2%	4.8%
	60s	0.4%	6.6%	5.6%	1.9%	3.6%
120s	10s	6.2%	6.6%	6.1%	2.9%	3.1%
	15s	2.8%	7.2%	3.4%	2.6%	3.0%
	30s	3.1%	7.1%	3.7%	4.5%	3.6%
	60s	1.1%	6.4%	4.4%	9.9%	5.9%
60s	10s	5.9%	6.9%	6.7%	1.4%	6.0%
	15s	8.9%	7.7%	7.7%	7.9%	13.0%
	30s	1.8%	6.1%	2.7%	10.0%	11.9%
	60s	2.8%	7.0%	3.4%	30.0%	25.8%
30s	10s	8.8%	7.8%	5.2%	5.7%	3.7%
	15s	8.4%	7.6%	6.3%	24.3%	10.4%
	30s	6.4%	8.2%	13.1%	31.4%	76.2%
	60s	6.6%	6.6%	11.7%	14.3%	80.9%

Table 5.4: Quantitative accuracy and estimation errors of time activity parameters for dynamic phantom experiments.

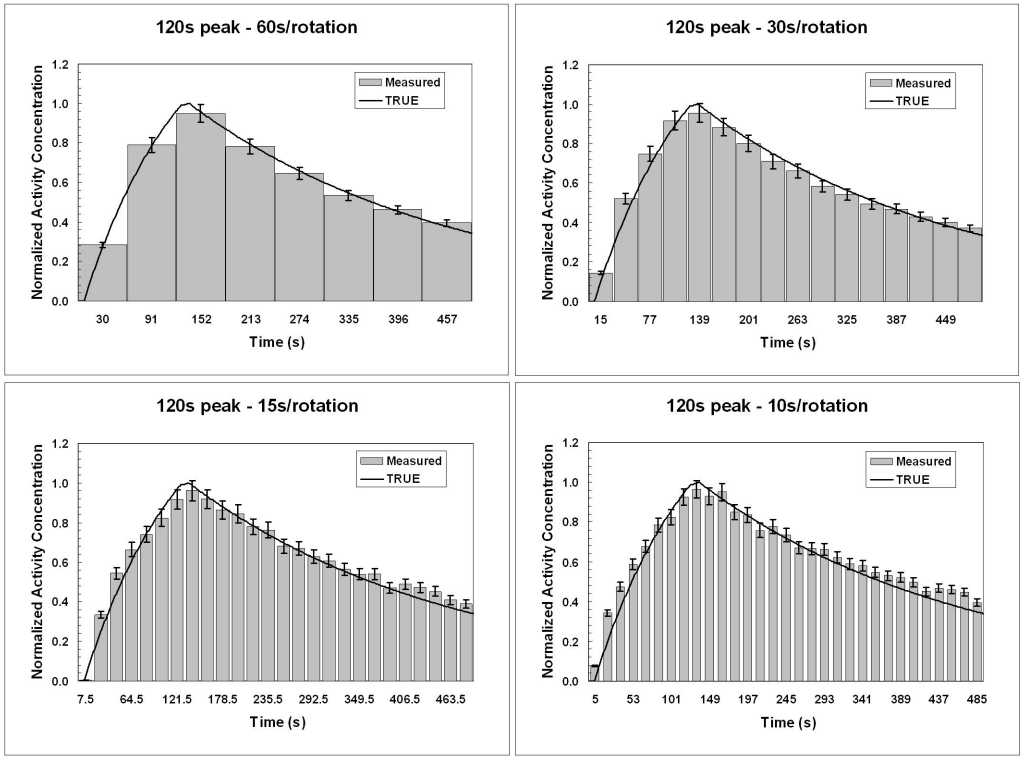

Figure 5.18: True and calculated activity concentration for a TAC with $T_P = 120s$ imaged with sampling frequencies of 60, 30, 15, and 10 seconds per rotation.

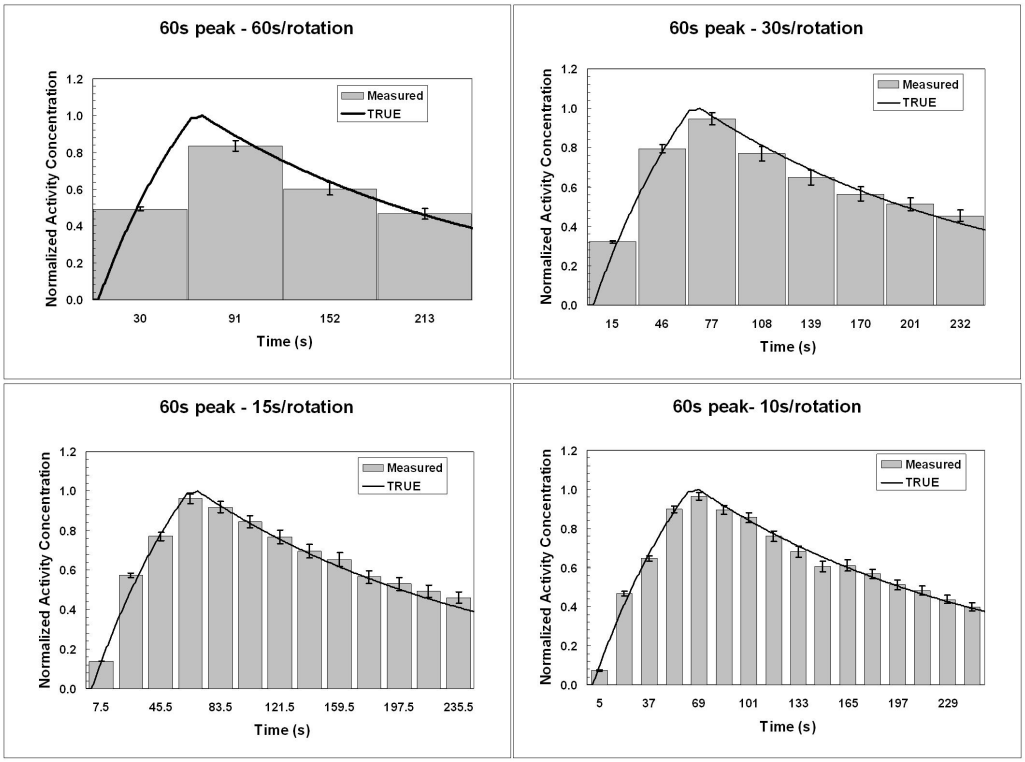

Figure 5.19: True and calculated activity concentration for a TAC with a $T_P = 60s$ imaged with sampling frequencies of 60, 30, 15, and 10 seconds per rotation.

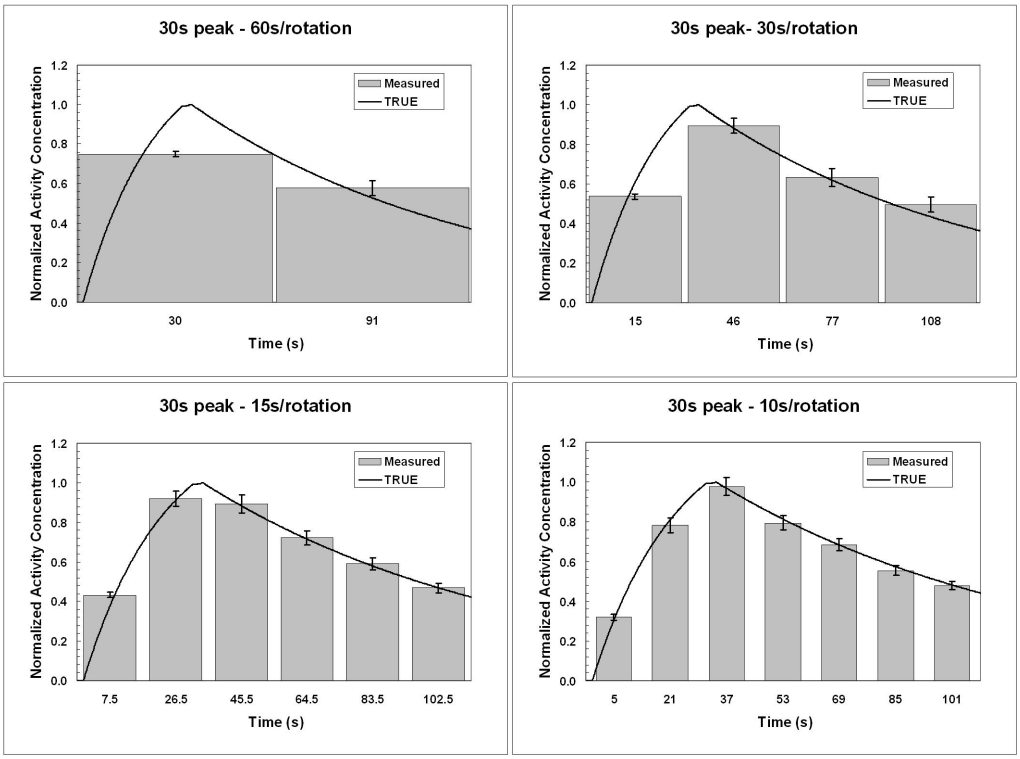

Figure 5.20: True and calculated activity concentration for a TAC with a $T_P = 30s$ imaged with sampling frequencies of 60, 30, 15, and 10 seconds per rotation.

5.3.3 Summary - Dynamic SPECT

We used time-contiguous SPECT acquisitions with a dual-headed gamma camera system to measure absolute activity concentrations of dynamic processes. We employed the calibration technique for quantitative SPECT which we originally developed for static 3D images. We showed in dynamic SPECT simulations that the recovery coefficients, which are used for calibration, are robust against signal to noise levels and sampling frequencies of the imaging system and therefor can be applied directly without further calibration.
We developed a physical phantom which provides flow rates for TACs with peak times down to 30 seconds. Various time-activity profiles and imaging speeds were tested and images were reconstructed using OSEM-3D. We could show that the quantitative accuracy of time-contiguous SPECT images of this phantom is within the same range as the accuracy for static SPECT images. This is true for TACs with peak times between 30 and 240 seconds. Time activity parameters such as peak time and the time of 50% wash-out can be estimated within 6% for a renal time-activity function using imaging speeds between 10 and 60 seconds per rotation and for profiles with T_P of 120, 60, and 30 seconds when the fastest possible gantry speed is used. From the present results we can conclude that the limiting factor for a reliable estimation of time-activity parameters is not the signal to noise ratio or the calibration method but rather the time sampling capabilities of the imaging device. It appears that accurate results are possible with sampling frequencies $f_{Sampling} > 2f_{TAC}$. With a minimum time of 10 seconds for a full SPECT data set and 5.7 seconds imaging dead time per volume, this would imply that processes with $T_P > 26s$ can be accurately measured with current dual-headed SPECT systems.

Chapter 6

Summary and Outlook

The goal of this thesis has been to optimize clinical Single Photon Emission Computed Tomography imaging for selected multi-modal static and dynamic applications. In the introductory Chapter 2 we in-depth discussed the characteristics of the SPECT image formation including the principles of imaging instrumentation, projection data generation and image reconstruction. In addition, we provided an overview of current clinical nuclear medicine applications and procedures. We discussed recent developments in the field of quantitative and dynamic SPECT and identified failures of these prior work that impede their use in routine clinical practice. In particular, the non-stationary behavior of the routinely used OSEM reconstruction in terms of emission recovery has not been studied extensively prior to this work. In addition, realistic measuring conditions in clinical environments have not been taken into account for quantitative procedures.

The first part of this thesis was focused on the optimization of clinical routine imaging protocols specific for the cardiac application. In Chapter 3 we developed tools for efficient data manipulation and objective image quality assessment of static and gated cardiac images. Image analysis tools were based on the known geometries of well established cardiac phantoms which are typically used for image quality testing in nuclear cardiology. In the case of the static phantom, we used the known geometry to generate an emission function of the myocardial wall by proper sampling of the cardiac chamber via profiles similar to previous work done for clinical diagnostic tools. The emission function served as basis for the generation of property maps and global quantitative metrics which were considered important for a SPECT system's image quality assessment. Validation of the developed tools using measured data demonstrated their practicability for the assessment of the image formation chain including quality control problems, attenuation effects, imaging instrumentation, and acquisition and reconstruction protocols. This allows the use in a wide range of purposes not only for SPECT but also for Positron Emission Tomography (PET).

In Chapter 4 we developed a time optimized cardiac acquisition protocol, using OSEM-3D, where the acquisition time could be reduced to 53% of conventional FBP-driven acquisition protocols. We assessed image quality and lesion detection ability by employing the developed phantom analysis tools and performing human observer studies. We found that the detection ability is not impacted when using 6° angular steps and OSEM-3D reconstruction. We tested the rapid acquisition protocol with a

database of static phantoms as well as with the dynamic phantom using a variety of gated phantom and imaging setups. An exemplary retrospective and a prospective study conducted at the Iowa Heart Institute delivered good correlations between the conventional and the new protocol.

In the second part of this thesis, we focused on the optimization of the image interpretation. Current routine clinical diagnosis is based on image intensities which do not represent the true absolute activity concentration of the target region due to processes inherent to current SPECT image formation.
We developed a calibration method for quantitative SPECT which can be used with current clinical imaging systems. One essential component of this calibration method is the consideration of the non-stationarity of clinically used iterative reconstruction. We derived emission recovery coefficients which depend on object size and position and more importantly on the number of OSEM updates. This non-stationary behavior was little mentioned in previous work but, in our opinion, presents a major challenge for quantitative SPECT when using current imaging systems in combination with OSEM. By using proper corrections for non-stationary behavior we obtained accurate quantitative results both in phantoms as well as in-vivo in patients. During our experiments we stressed the topic of imprecision of the obtained results. We estimated the accumulated errors which originate from measurement instrumentation and procedures throughout the course of calibration. We obtained an accumulated imprecision which is in the range of our accuracy yielding a 95% confidence interval with an expansion of 31%. In our study the dominant factor in the accumulated uncertainties due to measurement instrumentation is the well counter (5%). Using high precision measurement tools the overall uncertainties could be minimized. Still, in a clinical setup, using standard measurement tools, the presented uncertainty values are realistic.
In the final part of this thesis, we employ the developed calibration method for quantitative SPECT to dynamic imaging using time-contiguous acquisitions and 3D iterative reconstruction. We verified with simulations that the recovery coefficients, used for the calibration, are robust against signal to noise ratio and sampling frequency of the imaging system. We developed a physical dynamic phantom and established a baseline for the quantitative accuracy of dual-headed slow rotating SPECT/CT systems. The overall findings were that the limiting factor for accurate estimation of dynamic parameters is the sampling frequency of the imaging system. For a state-of-the-art dual-headed SPECT systems accurate results could be obtained for dynamic processes with peak times of 30 seconds. The imprecision of the obtained results is in the same range as for static images.

The long term goal in quantitative SPECT is to minimize the error bars and to increase the confidence in the obtained accuracy. New acquisition and processing techniques, e.g. simultaneous multi-modal acquisition and reconstruction, can help in the future to increase the image information relevant for quantification and to improve the precision.
Accurate quantification of other clinically important isotopes, e.g. for image based dosimetry in radiotherapy, like In-111 or I-131, may need additional correction fac-

tors in the reconstruction and calibration methods [91, 79]. Our method employs recovery coefficients derived from hot spherical objects which do not move. In order to use the method for other specific applications such as e.g. cardiac imaging, recovery coefficients specific for the shapes and positions of the target organ and more sophisticated partial volume corrections (see e.g. Da Silva et al., [82]) ought to be used. For moving objects e.g. the heart or lung tumors, motion correction methods need to be used to obtain the accuracy presented in this work.

Appendix A

Emission Recovery Look-up Tables

Object Volume (ml)	4 updates		8 updates		16 updates		32 updates		64 updates		128 updates	
	a	b	a	b	a	b	a	b	a	b	a	b
2482.7	0.842	0.820	0.961	0.938	0.983	0.959	0.994	0.970	1.001	0.976	1.004	0.980
1563.5	0.802	0.778	0.937	0.911	0.969	0.942	0.985	0.958	0.993	0.966	0.998	0.971
904.8	0.776	0.740	0.927	0.888	0.967	0.927	0.987	0.947	0.997	0.957	1.003	0.962
463.2	0.731	0.692	0.903	0.860	0.954	0.910	0.979	0.934	0.992	0.946	0.999	0.953
229.8	0.721	0.676	0.896	0.845	0.934	0.881	0.966	0.913	0.983	0.929	0.991	0.937
128.0	0.669	0.617	0.876	0.814	0.942	0.896	0.968	0.921	0.984	0.936	0.993	0.945
64.0	0.641	0.602	0.851	0.800	0.924	0.868	0.958	0.900	0.976	0.917	0.988	0.928
32.0	0.551	0.510	0.795	0.736	0.896	0.829	0.939	0.869	0.963	0.890	0.977	0.904
16.0	0.500	0.454	0.734	0.666	0.848	0.769	0.898	0.815	0.924	0.838	0.940	0.853
8.0	0.402	0.356	0.627	0.556	0.790	0.700	0.867	0.769	0.901	0.799	0.923	0.818
4.0	0.334	0.288	0.543	0.468	0.759	0.654	0.880	0.758	0.931	0.802	0.958	0.825
2.0	0.263	0.219	0.415	0.346	0.617	0.514	0.810	0.674	0.897	0.746	0.931	0.775
1.0	0.217	0.172	0.310	0.247	0.457	0.364	0.666	0.530	0.819	0.652	0.896	0.713
0.5	0.186	0.142	0.236	0.180	0.314	0.240	0.485	0.369	0.637	0.486	0.797	0.608

Table A.1: Recovery coefficients for LEHR collimation, 2.4 mm voxel size, 10% background, 2 million counts; a: values with spill-over corrections, b: values without spill-over correction.

Object Volume (ml)	4 updates a	4 updates b	8 updates a	8 updates b	16 updates a	16 updates b	32 updates a	32 updates b	64 updates a	64 updates b	128 updates a	128 updates b
2482.7	0.862	0.823	0.980	0.937	1.003	0.959	1.014	0.970	1.029	0.985	1.032	0.988
1563.5	0.820	0.775	0.958	0.908	0.990	0.938	1.006	0.953	1.014	0.961	1.018	0.965
904.8	0.797	0.738	0.953	0.885	0.994	0.924	1.014	0.943	1.023	0.952	1.028	0.957
463.2	0.754	0.688	0.933	0.856	0.985	0.905	1.010	0.928	1.023	0.940	1.029	0.946
229.8	0.756	0.676	0.940	0.845	0.972	0.874	1.005	0.905	1.022	0.920	1.031	0.928
128.0	0.705	0.617	0.924	0.814	0.988	0.889	1.014	0.913	1.029	0.926	1.036	0.933
64.0	0.673	0.591	0.896	0.787	0.974	0.856	1.009	0.887	1.028	0.903	1.038	0.912
32.0	0.588	0.501	0.849	0.724	0.961	0.819	1.007	0.858	1.031	0.879	1.045	0.891
16.0	0.537	0.442	0.786	0.646	0.911	0.749	0.965	0.794	0.991	0.815	1.007	0.827
8.0	0.437	0.343	0.679	0.532	0.865	0.678	0.953	0.746	0.986	0.773	1.006	0.788
4.0	0.367	0.275	0.589	0.441	0.824	0.617	0.967	0.724	1.021	0.764	1.043	0.780
2.0	0.301	0.211	0.459	0.321	0.671	0.469	0.856	0.599	0.938	0.656	0.966	0.675
1.0	0.251	0.167	0.349	0.232	0.501	0.333	0.704	0.468	0.854	0.568	0.935	0.621
0.5	0.219	0.137	0.264	0.165	0.340	0.213	0.467	0.291	0.587	0.367	0.673	0.420

Table A.2: Recovery coefficients for LEHR collimation, 4.8 mm voxel size, 10% background, 2 million counts; a: values with spill-over corrections, b: values without spill-over correction.

Object Volume (ml)	4 updates a	4 updates b	8 updates a	8 updates b	16 updates a	16 updates b	32 updates a	32 updates b	64 updates a	64 updates b	128 updates a	128 updates b
2482.7	0.888	0.815	1.008	0.926	1.029	0.946	1.038	0.954	1.042	0.958	1.043	0.959
1563.5	0.852	0.767	0.992	0.895	1.023	0.923	1.036	0.936	1.042	0.940	1.043	0.942
904.8	0.831	0.728	0.991	0.872	1.032	0.908	1.050	0.924	1.057	0.930	1.059	0.932
463.2	0.792	0.675	0.978	0.837	1.030	0.883	1.052	0.903	1.061	0.910	1.064	0.913
229.8	0.798	0.652	0.982	0.807	1.024	0.842	1.053	0.866	1.064	0.875	1.068	0.878
128.0	0.745	0.592	0.976	0.781	1.043	0.852	1.065	0.870	1.075	0.878	1.079	0.881
64.0	0.721	0.560	0.957	0.744	1.036	0.806	1.067	0.830	1.080	0.840	1.085	0.844
32.0	0.635	0.471	0.908	0.673	1.028	0.763	1.069	0.793	1.083	0.804	1.088	0.807
16.0	0.577	0.400	0.830	0.576	0.965	0.669	1.020	0.707	1.039	0.720	1.047	0.726
8.0	0.469	0.309	0.700	0.461	0.887	0.585	0.979	0.645	1.006	0.663	1.016	0.669
4.0	0.382	0.236	0.570	0.352	0.767	0.473	0.897	0.554	0.945	0.584	0.963	0.595
2.0	0.302	0.174	0.415	0.240	0.554	0.320	0.693	0.401	0.765	0.442	0.793	0.458
1.0	0.249	0.138	0.306	0.170	0.369	0.205	0.447	0.248	0.496	0.276	0.513	0.285
0.5	0.221	0.120	0.241	0.131	0.268	0.146	0.311	0.169	0.344	0.187	0.362	0.197

Table A.3: Recovery coefficients for LEHR collimation, 9.6 mm voxel size, 10% background, 2 million counts; a: values with spill-over corrections, b: values without spill-over correction.

List of Symbols and Acronyms

Symbols

x	Observed data	13
y	Image space coordinate	7
y	Hidden data	13
$\mathbf{A}$	System matrix	10
$\mathbf{A}_{d,c}$	System matrix including detector response and attenuation	11
$C_E(i,j)$	Emission recovery coefficient	81
$D(\theta,\xi)$	Myocardial wall distortion	44
$D(t)$	Decay factor	87
$D_{eff}(t,\Delta t)$	Effective decay factor	87
E_0	Initial photon energy	9
E_{SC}	Scattered photon energy	9
$E[\ldots]$	Expectation value operator	14
$E(r,\theta,\xi)$	Myocardial wall response function	41
$\mathbf{G}$	Poisson distributed random vector	11
I_0	Initial beam intensity	8
$I_{BP}(\theta,\xi)$	Bloodpool intensity	44
$I(x)$	Beam intensity	8
K	Collimator hole shape constant	8
$L()$	Objective function	54
N	Number of image voxels	11
P	Number of detector bins	11
$P(\theta,\xi)$	Integral perfusion	42
$Q()$	Q-function	14
$S(\theta,\xi)$	Myocardial wall nonsymmetry	44
S_{Vol}	System volume sensitivity	88
$T(\theta,\xi)$	Myocardial wall thickness	42

Acronyms

2D	Two-dimensional	5
$3D$	Three-dimensional	5
APD	Analytic photon distribution	21
AUC	Area under the curve	62
CLS	Constraint least-squares	34
CT	Computer tomography	1
COR	Center of Rotation	29
DPD	Diphosponate	93
DRF	Detector response function	18
$EANM$	European Association of Nuclear Medicine	27
ECG	Echocardiogram	2
ECT	Emission computed tomography	13
EDV	End-diastolic volume	52
EF	Ejection fraction	52
EM	Expectation maximization	13
ESV	End-systolic volume	52
FBP	Filtered backprojection	12

FOV	Field of view	6
$FWHM$	Full width at half maximum	6
HE	High energy	31
HLA	Horizontal ong axis	67
HU	Hounsfield unit	87
$LEAP$	Low energy all purpose	28
$LEHR$	Low energy high resolution	28
$LEHS$	Low energy high sensitivity	78
$LEUHR$	Low energy ultra high resolution	28
$MCAT$	Mathematical Cardiac Torso	34
MHR	Multi-head Registration	29
ML	Maximum likelihood	13
$MLEM$	Maximum likelihood expectation maximization	13
MTF	Modulation transfer function	86
$NEMA$	National Electrical Manufacturers Association	28
$OSEM$	Ordered subset expectation maximization	12
PET	Positron Emission Tomography	109
PMT	Photomultiplier tube	5
PSF	Point spread function	8
$RBSC$	Reconstruction-based scatter compensation	21
ROI	Region of interest	32
ROC	Receiver operating characteristics	61
RPS	Revolutions per second	101
SA	Short axis	52
SD	Standard deviation	46
SE	Standard error	62
SNM	Society of Nuclear Medicine	27
SRS	Summed rest score	70
SSS	Summed stress score	70
$SPECT$	Single photon emission computed tomography	1
SRF	Scatter response function	9
$TDCS$	Transmission-dependent convolution subtraction	21
TEW	Triple energy window	21
UHE	Ultra high energy	31
VLA	Vertical long axis	67
VOI	Volume of interest	87

List of Figures

List of Tables

Bibliography

[1] H. O. Anger, "Scintillation camera with multichannel collimators," *Journal of Nuclear Medicine*, vol. 5, no. 7, pp. 515–531, 1964.

[2] J. Radon, "Über die bestimmung von funktionen durch ihre integralwerte längs gewisser mannigfaltigkeiten," *Berichte Sächsische Akademie der Wissenschaften, Leipzig, Mathematisch-Physikalische Klasse*, vol. 69, pp. 262 – 277, 1917.

[3] S. R. Cherry, J. A. Sorenson, and M. E. Phelps, *Physics in nuclear medicine*, 3rd ed. Elsevier Science, 2003.

[4] C. C. Harris, K. L. Greer, R. J. Jaszczak, C. E. Floyd Jr, E. C. Fearnow, and R. E. Coleman, "Tc-99m attenuation coefficients in water-filled phantoms determined with gamma cameras," *Medical Physics*, vol. 11, pp. 681–685, 1984.

[5] E. C. Frey and B. M. W. Tsui, "Parameterization of the scatter response function in spect imagingusing monte carlo simulation," *IEEE Transactions on Nuclear Science*, vol. 37, no. 3 Part 1, pp. 1308–1315, 1990.

[6] C. E. Floyd, R. J. Jaszczak, C. C. Harris, and R. E. Coleman, "Energy and spatial distribution of multiple order compton scatter in spect: a monte carlo investigation," *Physics in Medicine and Biology*, vol. 29, pp. 1217–1230, 1984.

[7] M. S. Rosenthal and L. J. Henry, "Scattering in uniform media," *Physics in Medicine and Biology*, vol. 35, pp. 265–274, 1990.

[8] A. J. Rockmore and A. Macovski, "A maximum likelihood approach to emission image reconstruction from projections," *IEEE Transactions on Nuclear Science*, vol. 23, pp. 1428–1432, 1976.

[9] F. J. Beekman, H. de Jong, and S. van Geloven, "Efficient fully 3-d iterative spect reconstruction with monte carlo-based scatter compensation," *IEEE Transactions on Medical Imaging*, vol. 21, no. 8, pp. 867–877, 2002.

[10] L. A. Shepp and B. F. Logan, "Reconstructing interior head tissue from x-ray transmissions," *IEEE Transactions on Nuclear Science*, vol. 21, pp. 228–236, 1974.

[11] R. B. Blackman and J. W. Tukey, *The measurement of power spectra: from the point of view of communications engineering.* Dover Publications New York, 1959.

[12] S. Butterworth, "On the theory of filter amplifiers," *Circuit theory: foundations and classical contributions*, pp. 221–226, 1974.

[13] F. J. Klocke, M. G. Baird, B. H. Lorell, T. M. Bateman, J. V. Messer, D. S. Berman, P. T. O'Gara, B. A. Carabello, R. O. Russell, and M. D. Cerqueira, "Acc/aha/asnc guidelines for the clinical use of cardiac radionuclide imaging-executive summary-a report of the american college of cardiology/american heart association task force on practice," *Journal of the American College of Cardiology*, vol. 42, no. 7, pp. 1318–1333, 2003.

[14] J. A. Parker, M. E. Daube-Witherspoon, L. S. Graham, H. D. Royal, A. Todd-Pokropek, and M. V. Yester, "Society of nuclear medicine procedure guideline for general imaging," 2004.

[15] B. Hesse, K. Taegil, A. Cuocolo, C. Anagnostopoulos, M. Bardies, J. Bax, F. Bengel, E. B. Sokole, G. Davies, M. Dondi, L. Edenbrandt, P. Franken, A. Kjaer, J. Knuuti, M. Lassmann, M. Ljungberg, C. Marcassa, P. Marie, F. McKiddie, M. O'Connor, E. Prvulovich, R. Underwood, and B. Van Eck-Smit, "Eanm/esc procedural guidelines for myocardial perfusion imaging in nuclear cardiology," *European Journal of Nuclear Medicine and Molecular Imaging*, vol. 32, pp. 855–897, 2005.

[16] D. R. Gilland, R. J. Jaszczak, Z. Liang, K. L. Greer, and R. E. Coleman, "Quantitative spect brain imaging: effects of attenuation and detector response," *IEEE Transactions on Nuclear Science*, vol. 40, no. 3, pp. 295–299, 1993.

[17] B. M. W. Tsui, E. C. Frey, X. Zhao, D. S. Lalush, R. E. Johnston, and W. H. McCartney, "The importance and implementation of accurate 3d compensation methods for quantitative spect," *Physics in Medicine and Biology*, vol. 39, pp. 509–530, 1994.

[18] B. M. W. Tsui, X. Zhao, E. C. Frey, and W. H. McCartney, "Quantitative single-photon emission computed tomography: basics and clinical considerations," *Seminars in Nuclear Medicine*, vol. 24, no. 1, pp. 38–65, 1994.

[19] M. S. Rosenthal, "Quantitative spect imaging: a review and recommendations by the focus committee of the society of nuclear medicine computer and instrumentation council," *Journal of Nuclear Medicine*, vol. 36, no. 8, pp. 1489–1513, 1995.

[20] H. M. Hudson and R. S. Larkin, "Accelerated image reconstruction using ordered subsets of projection data," *IEEE Transactions on Medical Imaging*, vol. 13, no. 4, pp. 601–609, 1994.

[21] L. A. Shepp and Y. Vardi, "Maximum likelihood reconstruction for emission tomography," *IEEE Transactions on Medical Imaging*, vol. 1, no. 2, pp. 113–122, 1982.

[22] A. P. Dempster, N. M. Laird, and D. B. Rubin, "Maximum likelihood from incomplete data via the em algorithm," *Journal of the Royal Statistical Society*, vol. 39, no. 1, pp. 1–38, 1977.

[23] K. Lange and R. Carson, "Em reconstruction algorithms for emission and transmission tomography," *Journal of Computer Assisted Tomography*, vol. 8, no. 2, pp. 306–316, 1984.

[24] M. Wernick and J. Aarsvold, *Emission tomography: the fundamentals of PET and SPECT*. Elsevier Academic Press, 2004.

[25] S. J. Glick, M. A. King, T. S. Pan, and E. J. Soares, "An analytical approach for compensation of non-uniform attenuation in cardiac spect imaging," *Physics in Medicine and Biology*, vol. 40, pp. 1677–1677, 1995.

[26] H. Shinohara, T. Yamamoto, Y. Kuniyasu, T. Hashimoto, and T. Yokoi, "Implementation and quantitative evaluation of analytical methods for attenuation correction in spect: a phantom study," *Physics in Medicine and Biology*, vol. 44, pp. 2643–2655, 1999.

[27] H. Zaidi and B. Hasegawa, "Determination of the attenuation map in emission tomography," *Journal of Nuclear Medicine*, vol. 44, pp. 291–315, 2003.

[28] Y. Seo, K. H. Wong, M. Sun, B. L. Franc, R. A. Hawkins, and B. H. Hasegawa, "Correction of photon attenuation and collimator response for a body-contouring spect/ct imaging system," *Journal of Nuclear Medicine*, vol. 46, no. 5, pp. 868–877, 2005.

[29] J. S. Fleming, "A technique for using ct images in attenuation correction and quantification in spect," *Nuclear Medicine Communications*, vol. 10, no. 2, pp. 83–97, 1989.

[30] S. C. Blankespoor, X. Xu, K. Kaiki, J. K. Brown, H. R. Tang, C. E. Cann, and B. H. Hasegawa, "Attenuation correction of spect using x-ray ct on an emission-transmission ct system: myocardial perfusion assessment," *IEEE Transactions on Nuclear Science*, vol. 43, no. 4, pp. 2263–2274, 1996.

[31] Z. Liang, J. Ye, and D. P. Harrington, "An analytical approach to quantitative reconstruction of non-uniform attenuated brain spect," *Physics in Medicine and Biology*, vol. 39, no. 11, pp. 2023–2042, 1994.

[32] F. Natterer, "Inversion of the attenuated radon transform," *Inverse Problems*, vol. 17, no. 1, pp. 113–119, 2001.

[33] L. T. Chang, "A method for attenuation correction in radionuclide computed tomography," *IEEE Transactions on Nuclear Science*, vol. 25, pp. 638–643, 1978.

[34] K. Van Laere, M. Koole, J. Versijpt, and R. Dierckx, "Non-uniform versus uniform attenuation correction in brain perfusion spet of healthy volunteers," *European Journal of Nuclear Medicine and Molecular Imaging*, vol. 28, no. 1, pp. 90–98, 2001.

[35] E. S. Chornoboy, C. J. Chen, M. I. Miller, T. R. Miller, and D. L. Snyder, "An evaluation of maximum likelihood reconstruction for spect," *IEEE Transactions on Medical Imaging*, vol. 9, no. 1, pp. 99–110, 1990.

[36] G. T. Gullberg, R. H. Huesman, J. A. Malko, N. J. Pelc, and T. F. Budinger, "An attenuated projector-backprojector for iterative spect reconstruction," *Physics in Medicine and Biology*, vol. 30, pp. 799–816, 1985.

[37] G. L. Zeng and G. T. Gullberg, "Unmatched projector/backprojector pairs in an iterative reconstruction algorithm," *IEEE Transactions on Medical Imaging*, vol. 19, no. 5, pp. 548–555, 2000.

[38] H. Zaidi, *Quantitative Analysis in Nuclear Medicine Imaging*. New York: Springer, 2006.

[39] G. L. Zeng and G. T. Gullberg, "Frequency domain implementation of the three-dimensional geometricpoint response correction in spect imaging," *IEEE Transactions on Nuclear Science*, vol. 39, no. 5 Part 1, pp. 1444–1453, 1992.

[40] E. V. R. Di Bella, A. B. Barclay, R. L. Eisner, and R. W. Schafer, "A comparison of rotation-based methods for iterative reconstructionalgorithms," *IEEE Transactions on Nuclear Science*, vol. 43, no. 6, pp. 3370–3376, 1996.

[41] G. L. Zeng, G. T. Gullberg, B. M. W. Tsui, and J. A. Terry, "Three-dimensional iterative reconstruction algorithms withattenuation and geometric point response correction," *IEEE Transactions on Nuclear Science*, vol. 38, no. 2, pp. 693–702, 1991.

[42] A. W. McCarthy and M. I. Miller, "Maximum likelihood spect in clinical computation times using mesh-connected parallel computers," *IEEE Transactions on Medical Imaging*, vol. 10, no. 3, pp. 426–436, 1991.

[43] F. J. Beekman, E. G. J. Eijkman, M. A. Viergever, G. F. Borm, and E. T. P. Slijpen, "Object shape dependent psf model for spect imaging," *IEEE Transactions on Nuclear Science*, vol. 40, no. 1, pp. 31–39, 1993.

[44] E. C. Frey, Z. W. Ju, and B. M. W. Tsui, "A fast projector-backprojector pair modeling the asymmetric, spatially varying scatter response function for scatter compensation inspect imaging," *IEEE Transactions on Nuclear Science*, vol. 40, no. 4 Part 1, pp. 1192–1197, 1993.

[45] M. A. King, T. S. Pan, and D. S. Luo, "An investigation of aliasing with gaussian-diffusion modeling ofspect system spatial resolution," *IEEE Transactions on Nuclear Science*, vol. 44, no. 3 Part 2, pp. 1375–1380, 1997.

[46] V. Kohli, M. A. King, S. J. Glick, and T. S. Pan, "Comparison of frequency-distance relationship and gaussian-diffusion-based methods of compensation for distance-dependent spatial resolution in spect imaging," *Physics in Medicine and Biology*, vol. 43, pp. 1025–1038, 1998.

[47] K. F. Koral, N. H. Clinthorne, and W. Leslie Rogers, "Improving emission-computed-tomography quantification by compton-scatter rejection through offset windows," *Nuclear Instruments and Methods in Physics Research A*, vol. 242, pp. 610–614, 1986.

[48] K. F. Koral, Y. Dewaraja, and S. Lin, "I-131 tumor quantification: a new background-adaptive method," in *IEEE Nuclear Science Symposium Conference Record*, Albuquerque, NM, USA, 1997, pp. 1155–1159.

[49] I. Buvat, H. Beneli, A. Todd-Pokropek, and R. Di Paola, "Scatter correction in scinitigraphy: the state of the art," *European Journal of Nuclear Medicine and Molecular Imaging*, vol. 21, pp. 675–694, 1994.

[50] I. Buvat, M. Rodriguez-Villafuerte, A. Todd-Pokropek, H. Benali, and R. Di Paola, "Comparative assessment of nine scatter correction methods based on spectral analysis using monte carlo simulations," *Journal of Nuclear Medicine*, vol. 36, pp. 1476–1488, 1995.

[51] R. J. Jaszczak, K. L. Greer, C. E. Floyd Jr, C. C. Harris, and R. E. Coleman, "Improved spect quantification using compensation for scattered photons," *Journal of Nuclear Medicine*, vol. 25, pp. 893–900, 1984.

[52] K. Ogawa, Y. Harata, T. Ichihara, A. Kubo, and S. Hashimoto, "A practical method for position-dependent compton-scatter correction in single photon emission ct," *IEEE Transactions on Medical Imaging*, vol. 10, no. 3, pp. 408–412, 1991.

[53] M. A. King, G. J. Hademenos, and S. J. Glick, "A dual-photopeak window method for scatter correction," *Journal of Nuclear Medicine*, vol. 33, pp. 605–612, 1992.

[54] Y. Narita, S. Eberl, H. Iida, B. F. Hutton, M. Braun, T. Nakamura, and G. Bautovich, "Monte carlo and experimental evaluation of accuracy and noise properties of two scatter correction methods for spect," *Physics in Medicine and Biology*, vol. 41, pp. 2481–2496, 1996.

[55] T. Ichihara, K. Ogawa, N. Motomura, A. Kubo, and S. Hashimoto, "Compton scatter compensation using the triple-energy window method for single-and dual-isotope spect," *Journal of Nuclear Medicine*, vol. 34, no. 12, pp. 2216–2221, 1993.

[56] S. R. Meikle, B. F. Hutton, and D. L. Bailey, "A transmission-dependent method for scatter correction in spect," *Journal of Nuclear Medicine*, vol. 35, pp. 360–367, 1994.

[57] B. Axelsson, P. Msaki, and A. Israelsson, "Subtraction of compton-scattered photons in single-photon emission computerized tomography," *Journal of Nuclear Medicine*, vol. 25, no. 4, pp. 490–494, 1984.

[58] B. F. Hutton and V. Baccarne, "Efficient scatter modelling for incorporation in maximum likelihood reconstruction," *European Journal of Nuclear Medicine and Molecular Imaging*, vol. 25, pp. 1658–1665, 1998.

[59] R. G. Wells, A. Celler, and R. Harrop, "Analytical calculation of photon distributions in spect projections," *IEEE Transactions on Nuclear Science*, vol. 45, no. 6 Part 3, pp. 3202–3214, 1998.

[60] E. Vandervoort, A. Celler, G. Wells, S. Blinder, K. Dixon, and Y. Pang, "Implementation of an analytically based scatter correction in spect reconstructions," *IEEE Transactions on Nuclear Science*, vol. 52, pp. 645–653, 2005.

[61] J. E. Bowsher and C. E. Floyd Jr, "Treatment of compton scattering in maximum likelihood, expectation-maximization reconstructions of spect images," *Journal of Nuclear Medicine*, vol. 32, pp. 1285–1291, 1991.

[62] E. C. Frey and B. M. W. Tsui, "Modeling the scatter response function in inhomogeneous scattering media for spect," *IEEE Transactions on Nuclear Science*, vol. 41, no. 4 Part 1, pp. 1585–1593, 1994.

[63] M. V. Narayanan, P. H. Pretorius, S. T. Dahlberg, J. A. Leppo, N. Botkin, J. Krasnow, W. Berndt, E. C. Frey, and M. A. King, "Evaluation of scatter compensation strategies and their impact on human detection performance tc-99m myocardial perfusion imaging," *IEEE Transactions on Nuclear Science*, vol. 50, no. 5 Part 2, pp. 1522–1527, 2003.

[64] H. Zaidi and K. F. Koral, "Scatter modelling and compensation in emission tomography," *European Journal of Nuclear Medicine and Molecular Imaging*, vol. 31, pp. 761–782, 2004.

[65] C. Kamphuis, F. J. Beekman, P. P. Van Rijk, and M. A. Viergever, "Dual matrix ordered subsets reconstruction for accelerated 3d scatter compensation in single-photon emission tomography," *European Journal of Nuclear Medicine and Molecular Imaging*, vol. 25, pp. 8–18, 1997.

[66] T. Kuwert, F. Grünwald, U. Haberkorn, and T. Krause, *Nuklearmedizin.* Thieme Georg Verlag, 2008.

[67] E. A. o. N. Medicine, "Statistics survey: Status of nuclear medicine in europe," European Association of Nuclear Medicine, Tech. Rep., 2007, http://www.eanm.org.

[68] F. A. Mettler Jr, M. Bhargavan, K. Faulkner, D. B. Gilley, J. E. Gray, G. S. Ibbott, J. A. Lipoti, M. Mahesh, J. L. McCrohan, and M. G. Stabin, "Radiologic and nuclear medicine studies in the united states and worldwide: Frequency, radiation dose, and comparison with other radiation sources–1950-2007," *Radiology*, vol. 253, no. 2, pp. 520–531, 2009.

[69] A. Bockisch, L. S. Freudenberg, D. Schmidt, and T. Kuwert, "Hybrid imaging by spect/ct and pet/ct: Proven outcomes in cancer imaging," *Seminars in Nuclear Medicine*, vol. 39, pp. 276–289, 2009.

[70] E. Even-Sapir, Z. Keidar, and R. Bar-Shalom, "Hybrid imaging (spect/ct and pet/ct)Ůimproving the diagnostic accuracy of functional/metabolic and anatomic imaging," *Seminars in Nuclear Medicine*, vol. 39, pp. 264–275, 2009.

[71] A. Noemayr, W. Roemer, D. Strobel, W. Bautz, and T. Kuwert, "Anatomical accuracy of hybrid spect/spiral ct in the lower spine," *Nuclear Medicine Communications*, vol. 27, no. 6, pp. 521–528, 2006.

[72] A. Nuis, "Council directive 97/43/euratom of 30 june 1997 on health protection of individuals against the dangers of ionizing radiation in relation to medical exposure, and repealing directive 84/466/euratom," *Official Journal of the European Communities*, vol. L 180, pp. 22–27, 1997.

[73] K. J. Donohoe, M. L. Brown, and B. D. Collier, "Society of nuclear medicine procedure guideline for bone scintigraphy," pp. 205–209, 2003.

[74] H. R. Balon, S. J. Goldsmith, B. A. Siegel, E. B. Silberstein, E. P. Krenning, O. Lang, and K. J. Donohoe, "Procedure guideline for somatostatin receptor scintigraphy with 111in-pentetreotide," *Journal of Nuclear Medicine*, vol. 42, no. 7, pp. 1134–1138, 2001.

[75] L. Kapucu, F. Nobili, A. Varrone, J. Booij, T. Vander Borght, K. Någren, J. Darcourt, K. Tatsch, and K. J. Van Laere, "Eanm procedure guideline for brain perfusion spect using 99m tc-labelled radiopharmaceuticals, version 2," *European Journal of Nuclear Medicine and Molecular Imaging*, vol. 36, pp. 2093–2102, 2009.

[76] E. Busemann Sokole, A. P achcínska, A. Britten, M. Lyra Georgosopoulou, W. Tindale, and R. Klett, "Routine quality control recommendations for nuclear medicine instrumentation," *European Journal of Nuclear Medicine and Molecular Imaging*, vol. 37, pp. 662–671, 2010.

[77] J. T. Chapman, J. Hugg, J. Vesel, C. Bai, and I. Blevis, "Nema standards publication nu 1-2007," 2007.

[78] H. Hines, R. Kayayan, J. Colsher, D. Hashimoto, R. Schubert, J. Fernando, V. Simcic, P. Vernon, and R. L. Sinclair, "National electrical manufacturers association recommendations for implementing spect instrumentation quality control," *Journal of Nuclear Medicine*, vol. 41, no. 2, pp. 382–389, 2000.

[79] Y. K. Dewaraja, S. J. Wilderman, K. F. Koral, M. S. Kaminski, and A. M. Avram, "Use of integrated spect/ct imaging for tumor dosimetry in i-131 radioimmunotherapy: A pilot patient study," *Cancer Biotherapy and Radiopharmaceuticals*, vol. 24, no. 4, pp. 417–426, 2009.

[80] B. He, Y. Du, W. P. Segars, R. L. Wahl, G. Sgouros, H. Jacene, and E. C. Frey, "Evaluation of quantitative imaging methods for organ activity and residence time estimation using a population of phantoms having realistic variations in anatomy and uptake," *Medical Physics*, vol. 36, pp. 612–619, 2009.

[81] M. Ljungberg, K. Sjogreen, X. Liu, E. Frey, Y. Dewaraja, and S. E. Strand, "A 3-dimensional absorbed dose calculation method based on quantitative spect for radionuclide therapy: evaluation for 131i using monte carlo simulation," *Journal of Nuclear Medicine*, vol. 43, no. 8, pp. 1101–1109, 2002.

[82] A. J. Da Silva, H. R. Tang, M. C. Wu, and B. H. Hasegawa, "Absolute quantitation of myocardial activity in phantoms," *IEEE Transactions on Nuclear Science*, vol. 46, no. 3 Part 2, pp. 659–666, 1999.

[83] A. J. Da Silva, H. R. Tang, K. H. Wong, M. C. Wu, M. W. Dae, and B. H. Hasegawa, "Absolute quantification of regional myocardial uptake of 99mtc-sestamibi with spect: experimental validation in a porcine model," *Journal of Nuclear Medicine*, vol. 42, no. 5, pp. 772–779, 2001.

[84] E. Vandervoort, A. Celler, and R. Harrop, "Implementation of an iterative scatter correction, the influence of attenuation map quality and their effect on absolute quantitation in spect," *Physics in Medicine and Biology*, vol. 52, pp. 1527–1545, 2007.

[85] S. Liu and T. Farncombe, "Collimator-detector response compensation in quantitative SPECT reconstruction," in *IEEE Nuclear Science Symposium Conference Record*, vol. 5, Honolulu, HI, USA, 2007, pp. 3955–3960.

[86] K. Willowson, D. L. Bailey, and C. Baldock, "Quantitative spect reconstruction using ct-derived corrections," *Physics in Medicine and Biology*, vol. 53, pp. 3099–3112, 2008.

[87] Y. Du, B. M. Tsui, and E. C. Frey, "Model-based compensation for quantitative 123 i brain spect imaging," *Physics in Medicine and Biology*, vol. 51, no. 5, pp. 1269–1282, 2006.

[88] S. Shcherbinin, A. Celler, T. Belhocine, R. Vanderwerf, and A. Driedger, "Accuracy of quantitative reconstructions in spect/ct imaging," *Physics in Medicine and Biology*, vol. 53, no. 17, pp. 4595–4604, 2008.

[89] S. Shcherbinin and A. Celler, "Quantitative accuracy of SPECT reconstructions with a voxelized CT-based partial volume effect correction," in *IEEE Nuclear Science Symposium Conference Record*, Dresden, Germany, 2008, pp. 4311–4318.

[90] B. He, Y. Du, X. Song, W. P. Segars, and E. C. Frey, "A monte carlo and physical phantom evaluation of quantitative in-111 spect," *Physics in Medicine and Biology*, vol. 50, no. 17, pp. 4169–4186, 2005.

[91] K. F. Koral, A. Yendiki, and Y. K. Dewaraja, "Recovery of total i-131 activity within focal volumes using spect and 3d osem," *Physics in Medicine and Biology*, vol. 52, no. 3, pp. 777–790, 2007.

[92] K. F. Koral, A. Yendiki, V. Lin, and Y. K. Dewaraja, "Comparison of 3d osem vs 1d sage for focal total-activity quantification in i-131 spect with he collimation," *IEEE Transactions on Nuclear Science*, vol. 52, pp. 154–158, 2005.

[93] K. F. Koral, A. Yendiki, Q. Lin, Y. K. Dewaraja, and J. A. Fessler, "Determining total i-131 activity within a voi using spect, a uhe collimator, osem, and a constant conversion factor," *IEEE Transactions on Nuclear Science*, vol. 51, no. 3 Part 2, pp. 611–618, 2004.

[94] T. R. Miller, "Clinically important characteristics of maximum-likelihood reconstruction," *Journal of Nuclear Medicine*, vol. 33, pp. 1678–1684, 1992.

[95] J. W. Stayman and J. A. Fessler, "Compensation for nonuniform resolution using penalized-likelihood reconstruction in space-variant imaging systems," *IEEE Transactions on Medical Imaging*, vol. 23, no. 3, pp. 269–284, 2004.

[96] J. S. Liow and S. C. Strother, "The convergence of object dependent resolution in maximum likelihood based tomographic image reconstruction," *Physics in Medicine and Biology*, vol. 38, pp. 55–70, 1993.

[97] G. N. Sfakianakis, E. Sfakianaki, M. Georgiou, A. Serafini, S. Ezuddin, and R. Kuker, "A renal protocol for all ages and all indications: Mercapto-acetyltriglycine (mag3) with simultaneous injection of furosemide (mag3-f0): A 17-year experience," *Seminars in Nuclear Medicine*, vol. 39, pp. 156–173, 2009.

[98] T. Zajic and E. Moser, "Procedure guidelines for dynamic renal scintigraphy," *NuklearMedizin*, vol. 43, pp. 177–80, 2004.

[99] K. J. Donohoe, A. H. Maurer, H. A. Ziessman, J. L. C. Urbain, and H. D. Royal, "Procedure guideline for gastric emptying and motility," *Journal of Nuclear Medicine*, vol. 40, pp. 1236–1239, 1999.

[100] A. Celler, T. Farncombe, R. Harrop, D. Noll, J. Maeght, and D. Lyster, "Three approaches to dynamic spect imaging," in *IEEE Nuclear Science Symposium Conference Record*, vol. 2, Albuquerque, NM , USA, 1997, pp. 1451–1455.

[101] K. Nakajima, J. Taki, H. Bunko, M. Matsudaira, A. Muramori, I. Matsunari, K. Hisada, and T. Ichihara, "Dynamic acquisition with a three-headed spect system: application to technetium 99m-sq30217 myocardial imaging," *Journal of Nuclear Medicine*, vol. 32, no. 6, pp. 1273–1277, 1991.

[102] M. V. Narayanan, R. Licho, T. H. Farncombe, M. A. King, and H. Pretorius, "Evaluation of the impact of 4d reconstruction algorithms in quantitative dynamic spect," in *IEEE Nuclear Science Symposium Conference Record*, vol. 2, Norfolk, VA, USA, 2002, pp. 1023–1026.

[103] N. Luyt and R. G. Wells, "Imaging of hepatic hemangiomas using multirotation dynamic spect," in *IEEE Nuclear Science Symposium Conference Record*, vol. 4, Portland, OR, USA, 2003, pp. 2932–2936.

[104] H. H. Bauschke, D. Noll, A. Celler, and J. M. Borwein, "An em-algorithm for dynamic spect tomography," *IEEE Transactions on Medical Imaging*, vol. 18, no. 3, pp. 252–261, 1999.

[105] T. Farncombe, S. Blinder, A. Celler, D. Noll, J. Maeght, and R. Harrop, "A dynamic expectation maximization algorithm for single camera rotation dynamic spect (dspect)," in *IEEE Nuclear Science Symposium Conference Record*, Lyon , France, 2000, pp. 31–35.

[106] T. Farncombe, M. King, A. Celler, and S. Blinder, "A fully 4d expectation maximization algorithm using gaussian diffusion based detector response for slow camera rotation dynamic spect," *Proceedings of the 2001 International Meeting on Fully 3D Image Reconstruction in Radiology and Nuclear Medicine*, pp. 129–132, 2001.

[107] M. A. Limber, M. N. Limber, A. Celler, J. S. Barney, and J. M. Borwein, "Direct reconstruction of functional parameters for dynamic spect," *IEEE Transactions on Nuclear Science*, vol. 42, no. 4, pp. 1249–1256, 1995.

[108] T. Farncombe, A. Celler, D. Noll, J. Maeght, and R. Harrop, "An evaluation of dynamic spect imaging methods," in *IEEE Nuclear Science Symposium Conference Record*, vol. 3, 1998, pp. 1959–1963.

[109] B. W. Reutter, G. T. Gullberg, and R. H. Huesman, "Kinetic parameter estimation from attenuated spect projection measurements," *IEEE Transactions on Nuclear Science*, vol. 45, no. 6, pp. 3007–3013, 1998.

[110] T. Farncombe, A. Celler, D. Noll, J. Maeght, and R. Harrop, "Dynamic spect imaging using a single camera rotation (dspect)," *IEEE Transactions on Nuclear Science*, vol. 46, no. 4, pp. 1055–1061, 1999.

[111] A. Celler, T. Farncombe, C. Bever, D. Noll, J. Maeght, R. Harrop, and D. Lyster, "Performance of the dynamic single photon emission computed tomography (dspect) method for decreasing or increasing activity changes," *Physics in Medicine and Biology*, vol. 45, no. 12, pp. 3525–3544, 2000.

[112] B. W. Reutter, G. T. Gullberg, and R. H. Huesman, "Direct least-squares estimation of spatiotemporal distributions from dynamic spect projections using a spatial segmentation and temporal b-splines," *IEEE Transactions on Medical Imaging*, vol. 19, no. 5, pp. 434–450, 2000.

[113] A. Sitek, E. V. R. Di Bella, and G. T. Gullberg, "Reconstruction from slow rotation dynamic spect using a factor model," *Lecture Notes in Computer Science*, pp. 436–441, 1999.

[114] A. Sitek, G. T. Gullberg, E. V. R. Di Bella, and A. Celler, "Reconstruction of dynamic renal tomographic data acquired by slow rotation," *Journal of Nuclear Medicine*, vol. 42, no. 11, pp. 1704–1712, 2001.

[115] B. W. Reutter, G. T. Gullberg, and R. H. Huesman, "Effects of temporal modelling on uncertainty of dynamic spect," *Physics in Medicine and Biology*, vol. 47, pp. 2673–2683, 2002.

[116] ——, "Accuracy and precision of compartmental model parameters obtained from directly estimated dynamic spect time-activity curves," *IEEE Transactions on Nuclear Science*, vol. 51, no. 1, pp. 170–176, 2004.

[117] B. W. Reutter, S. Oh, G. T. Gullberg, and R. H. Huesman, "Improved quantitation of dynamic spect via fully 4-d joint estimation of compartmental models and blood input function directly from projections," in *IEEE Nuclear Science Symposium Conference Record*, Puerto Rico, 2005, pp. 2337–2341.

[118] B. W. Reutter, G. T. Gullberg, R. Boutchko, K. Balakrishnan, E. H. Botvinick, and R. H. Huesman, "Fully 4-d dynamic cardiac spect image reconstruction using spatiotemporal b-spline voxelization," in *IEEE Nuclear Science Symposium Conference Record*, vol. 6, Honolulu, HI, USA, 2007, pp. 4217–4221.

[119] C. D. Winant, Y. R. Zelnik, B. W. Reutter, A. Sitek, S. L. Bacharach, G. T. Gullberg, and C. M. Aparici, "Analysis of dynamic spect/ct measurements of the arterial input function in human subjects," in *IEEE Nuclear Science Symposium Conference Record*, Orlando, FL, USA, 2009, pp. 3404–3408.

[120] K. Yamakado, K. Matsumura, Y. Takashiba, A. Nakatsuka, T. Kitano, T. Ichihara, H. Maeda, K. Takase, and K. Takeda, "Binding rate constant of tc-99m dtpa galactosyl human serum albumin measured by quantitative dynamic spectŮclinical evaluation as a total and regional liver function testŮ," *Annals of Nuclear Medicine*, vol. 15, no. 3, pp. 191–198, 2001.

[121] N. Shuke, T. Aburano, A. Okizaki, C. Zhao, K. Nakajima, K. Yokoyama, S. Kinuya, N. Watanabe, T. Michigishi, and N. Tonami, "Estimation of fractional liver uptake and blood retention of 99mtc-dtpa-galactosyl human serum albumin: an application of a simple graphical method to dynamic spect," *Nuclear Medicine Communications*, vol. 24, no. 5, pp. 503–511, 2003.

[122] Y. Sugai, A. Komatani, T. Hosoya, and K. Takahashi, "Comparisons of the time-activity curves of the cardiac blood pool and liver uptake by 99m tc-gsa dynamic spect and measured 99m tc-gsa blood concentrations," *Annals of Nuclear Medicine*, vol. 20, no. 4, pp. 295–301, 2006.

[123] H. Iida, S. Eberl, K. M. Kim, Y. Tamura, Y. Ono, M. Nakazawa, A. Sohlberg, T. Zeniya, T. Hayashi, and H. Watabe, "Absolute quantitation of myocardial blood flow with 201 tl and dynamic spect in canine: optimisation and validation of kinetic modelling," *European Journal of Nuclear Medicine and Molecular Imaging*, vol. 35, no. 5, pp. 896–905, 2008.

[124] K. J. Nichols, S. L. Bacharach, S. R. Bergmann, J. Chen, S. J. Cullom, S. Dorbala, E. P. Ficaro, J. R. Galt, D. L. Green Conaway, and G. V. Heller, "Instrumentation quality assurance and performance," *Journal of Nuclear Cardiology*, vol. 14, no. 6, pp. 61–78, 2007.

[125] C. L. Hansen, R. A. Goldstein, O. O. Akinboboye, D. S. Berman, E. H. Botvinick, K. B. Churchwell, C. D. Cooke, J. R. Corbett, S. J. Cullom, S. T. Dahlberg, R. S. Druz, E. P. Ficaro, J. R. Galt, R. K. Garg, G. Germano, G. V. Heller, M. J. Henzlova, M. C. Hyun, L. L. Johnson, A. Mann, B. D. McCallister Jr, R. A. Quaife, T. D. Ruddy, S. N. Sundaram, R. Taillefer, R. P. Ward, and J. J. Mahmarian, "Asnc imaging guidelines for nuclear cardiology procedures," *Journal of Nuclear Cardiology*, vol. 14, no. 6, pp. e39–60, 2007.

[126] D. R. Gilland, B. M. Tsui, Q. Yujin, and G. T. Gullberg, "Comparison of channelized hotelling and human observers in determining optimum os-em reconstruction parameters for myocardial spect," *IEEE Transactions on Nuclear Science*, vol. 53, no. 3, pp. 1200–1204, 2006.

[127] E. C. Frey, D. R. Gilland, and B. M. W. Tsui, "Application of task-based measures of image quality to optimization and evaluation of three dimensional reconstruction-based compensation methods in myocardial perfusion spect," *IEEE Transactions on Medical Imaging*, vol. 21, no. 9, pp. 1040–1050, 2002.

[128] X. He, E. C. Frey, J. Links, D. R. Gilland, W. P. Segars, and B. M. W. Tsui, "Evaluation and optimization of compensation methods for myocardial spect using a set of realistic phantoms that include patient variability," in *IEEE Nuclear Science Symposium Conference Record*, vol. 2, Norfolk, VA, USA, 2002, pp. 764–768.

[129] M. V. Narayanan, M. A. King, J. A. Leppo, S. T. Dahlberg, P. H. Pretorius, and H. C. Gifford, "Optimization of regularization of attenuation and scatter-corrected 99mtc cardiac spect studies for defect detection using hybrid images," *IEEE Transactions on Nuclear Science*, vol. 48, no. 3, pp. 785–789, 2001.

[130] S. Sankaran, E. C. Frey, K. L. Gilland, and B. M. Tsui, "Optimum compensation method and filter cutoff frequency in myocardial spect: A human observer study," *Journal of Nuclear Medicine*, vol. 43, no. 3, pp. 432–438, 2002.

[131] A. H. Vija, E. G. Hawman, and J. C. Engdahl, "Analysis of a spect osem reconstruction method with 3d beam modeling and optional attenuation correction: phantom studies," in *IEEE Nuclear Science Symposium Conference Record*, vol. 4, Portland, OR, USA, 2003, pp. 2662–2666.

[132] A. H. Vija, J. Zeintl, J. T. Chapman, E. G. Hawman, and J. Hornegger, "Development of rapid spect acquisition protocol for myocardial perfusion imaging," in *IEEE Nuclear Science Symposium Conference Record*, vol. 3, San Diego, CA, USA, 2006, pp. 1811–1816.

[133] C. B. Williams, A. H. Vija, T. D. Rempel, E. G. Hawman, and J. C. Engdahl, "Analysis of the impact of ct based attenuation correction, scatter compensation and 3d- beam modeling on spect image quality," in *IEEE Nuclear Science Symposium Conference Record*, vol. 6, Rome, Italy, 2004, pp. 3519–3522.

[134] J. Zeintl, A. H. Vija, J. T. Chapman, E. G. A. H. E. G. Hawman, and J. A. H. J. Hornegger, "Quantifying the effects of acquisition parameters in cardiac spect imaging and comparison with visual observers," in *IEEE Nuclear Science Symposium Conference Record*, vol. 6, San Diego, CA, USA, 2006, pp. 3251–3257.

[135] C. Wiuf and M. P. H. Stumpf, "Binomial subsampling," *Proceedings of the Royal Society Association*, vol. 462, pp. 1181–1195, 2006.

[136] C. D. Cooke, E. V. Garcia, R. D. Folks, J. W. Peifer, and N. F. Ezquerra, "Visualization of cardiovascular nuclear medicine tomographic perfusion studies," in *Conference on Visualization in Biomedical Computing*, Atlanta, 1990, pp. 185–189.

[137] E. E. DePasquale, A. C. Nody, E. G. DePuey, E. V. Garcia, G. Pilcher, C. Bredlau, G. Roubin, A. Gober, A. Gruentzig, and P. D'Amato, "Quantitative rotational thallium-201 tomography for identifying and localizing coronary artery disease," *Circulation*, vol. 77, no. 2, pp. 316–327, 1988.

[138] E. V. Garcia, "Quantification of rotational thallium-201 myocardial tomography," *Journal of Nuclear Medicine*, vol. 26, no. 1, pp. 17–26, 1985.

[139] J. Maddahi, E. V. Garcia, D. S. Berman, A. Waxman, H. J. Swan, and J. Forrester, "Improved noninvasive assessment of coronary artery disease by quantitative analysis of regional stress myocardial distribution and washout of thallium-201," *Circulation*, vol. 64, no. 5, pp. 924–935, 1981.

[140] G. Germano, J. Erel, H. Lewin, P. B. Kavanagh, and D. S. Berman, "Automatic quantitation of regional myocardial wall motion and thickening from gated technetium-99m sestamibi myocardial perfusion single-photon emission computed tomography," *Journal of the American College of Cardiology*, vol. 30, pp. 1360–1367, 1997.

[141] G. Germano, P. B. Kavanagh, P. Waechter, J. S. Areeda, S. Van Kriekinge, T. Sharir, H. C. Lewin, and D. S. Berman, "A new algorithm for the quantitation of myocardial perfusion spect. i: technical principles and reproducibility," *Journal of Nuclear Medicine*, vol. 41, no. 4, pp. 712–719, 2000.

[142] K. F. Van Train, J. S. Areeda, E. V. Garcia, C. D. Cooke, J. Maddahi, H. Kiat, G. Germano, G. Silagan, R. Folks, and D. S. Berman, "Quantitative same-day rest-stress technetium-99m-sestamibi spect: Definition and validation of stress normal limits and criteria for abnormality," *Journal of Nuclear Medicine*, vol. 34, pp. 1494–1502, 1993.

[143] G. Germano, T. Chua, H. Kiat, J. S. Areeda, and D. S. Berman, "A quantitative phantom analysis of artifacts due to hepatic activity in technetium-99m myocardial perfusion spect studies," *Journal of Nuclear Medicine*, vol. 35, no. 2, pp. 356–359, 1994.

[144] M. D. Cerqueira, N. J. Weissman, V. Dilsizian, S. K. Jacobs, W. K. Laskey, D. J. Pennell, J. A. Rumberger, T. J. Ryan, and M. S. Verani, "Standardized myocardial segmentation and nomenclature for tomographic imaging of the heart." *Journal of Nuclear Cardiology*, vol. 9, no. 2, pp. 240–245, 2002.

[145] F. J. T. Wackers, D. S. Berman, J. Maddahi, D. D. Watson, G. A. Beller, H. W. Strauss, C. A. Boucher, M. Picard, B. L. Holman, R. Fridrich, E. Inglese, B. Delaloye, A. Bischof-Delaloye, L. Camin, and K. McKusick, "Technetium-99m hexakis 2-methoxyisobutyl isonitrile: Human biodistribution dosimetry, safety and preliminary comparison to thallium-201 for myocardial perfusion imaging," *Journal of Nuclear Medicine*, vol. 30, pp. 301–311, 1989.

[146] J. Nuyts, "A study of the liver-heart artifact in emission tomography," *Journal of Nuclear Medicine*, vol. 36, no. 1, pp. 133–139, 1995.

[147] P. Maragos, "Morphological filtering for image enhancement and feature detection," in *The Image and Video Processing Handbook*, 2nd ed., A. C. Bovik, Ed. Elsevier, 2005, pp. 135–156.

[148] C. Kamphuis, F. J. Beekman, and M. A. Viergerver, "Evaluation of os-em vs. ml-em for 1d, 2d and fully 3d spect reconstruction," *IEEE Transactions on Nuclear Science*, vol. 43, no. 3, pp. 2018–2024, 1996.

[149] J. A. Bieszk and E. G. Hawman, "Evaluation of spect angular sampling effects: Continuous versus step-and-shoot acquisition," *Journal of Nuclear Medicine*, vol. 28, pp. 1308–1314, 1987.

[150] M. K. O'Connor and C. B. Hruska, "Effect of tomographic orbit and type of rotation on apparent myocardial activity," *Nuclear Medicine Communications*, vol. 26, no. 1, pp. 25–30, 2005.

[151] Y. H. Lau, B. F. Hutton, and F. J. Beekman, "Choice of collimator for cardiac spet when resolution compensation is included in iterative reconstruction," *European Journal of Nuclear Medicine and Molecular Imaging*, vol. 28, no. 1, pp. 39–47, 2001.

[152] J. A. Hanley and B. J. McNeil, "The meaning and use of the area under a receiver operating characteristic (roc) curve," *Radiology*, vol. 143, pp. 29–36, 1982.

[153] W. H. Press, B. P. Flannery, S. A. Teukolsky, and W. T. Vetterling, *Numerical Recipes: The Art of Scientific Computing*, 3rd ed., ser. Cambridge U. Press, Cambridge, England. Cambridge University Press, 2007.

[154] N. J. Purser, H. A. Williams, C. M. Tonge, and R. S. Lawson, "Apical thinning: real or artefact?" *Nuclear Medicine Communications*, vol. 29, pp. 382–389, 2008.

[155] J. M. Bland and D. G. Altman, "Measuring agreement in method comparison studies," *Statistical Methods in Medical Research*, vol. 8, no. 2, pp. 135–160, 1999.

[156] I. Bronshtein, K. Semendyayev, G. Musiol, and H. Muehlig, *Handbook of Mathematics*. Springer, 2004.

[157] J. R. Taylor, *An Introduction to Error Analysis: The Study of Uncertainties in Physical Measurements*, 2nd ed. Sausalito, California: University Science Books, 1997.